INSTITUTO DE FÍSICA

Universidade Federal Fluminense

Electronic Properties of Standard and Fractal Nanoscopic Systems

Lucas Lopes Lage

Niterói
2022

Electronic Properties of Standard and Fractal Nanoscopic Systems

Supervisor:

Profa. Dra. : **ANDREA LATGÉ**

Dissertation presented to the Departamento de Física of Universidade Federal Fluminense in partial fulfillment of the requirements for the degree of Master of Science.

Niterói

2022

Ata dos trabalhos finais da Comissão Examinadora da dissertação apresentada por **Lucas Lopes Lage**. No vigésimo nono dia do mês de julho de dois mil e vinte e dois, às quatorze horas e trinta minutos, reuniram-se no Instituto de Física da Universidade Federal Fluminense os membros da Comissão Examinadora constituída pelos professores doutores Andréa Brito Latgé (IF/UFF), Marcos Gonçalves de Menezes (UFRJ), Yutao Xing (IF/UFF) e de forma remota Roberto Hiroki Miwa (UFU); sob a presidência do primeiro, para prova pública de apresentação da dissertação intitulada *"Electronic Properties of Standard and Fractal Nanoscopic Systems"*, tendo em vista as exigências do Regulamento Específico do curso de Física relacionadas com a conclusão do Mestrado em Física pela Universidade Federal Fluminense. A dissertação foi elaborada sob a orientação da professora Andréa Brito Latgé. Após a exposição do trabalho, o aluno respondeu às questões formuladas pelos integrantes da Comissão Examinadora, que apresentou parecer no sentido de aprová-lo. Para constar, foi lavrada a presente ata, que vai assinada pelos membros da Comissão Examinadora e pelo mestrando.
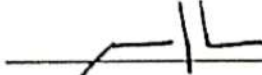
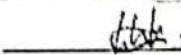Niterói, vinte e nove de julho de dois mil e vinte e dois.
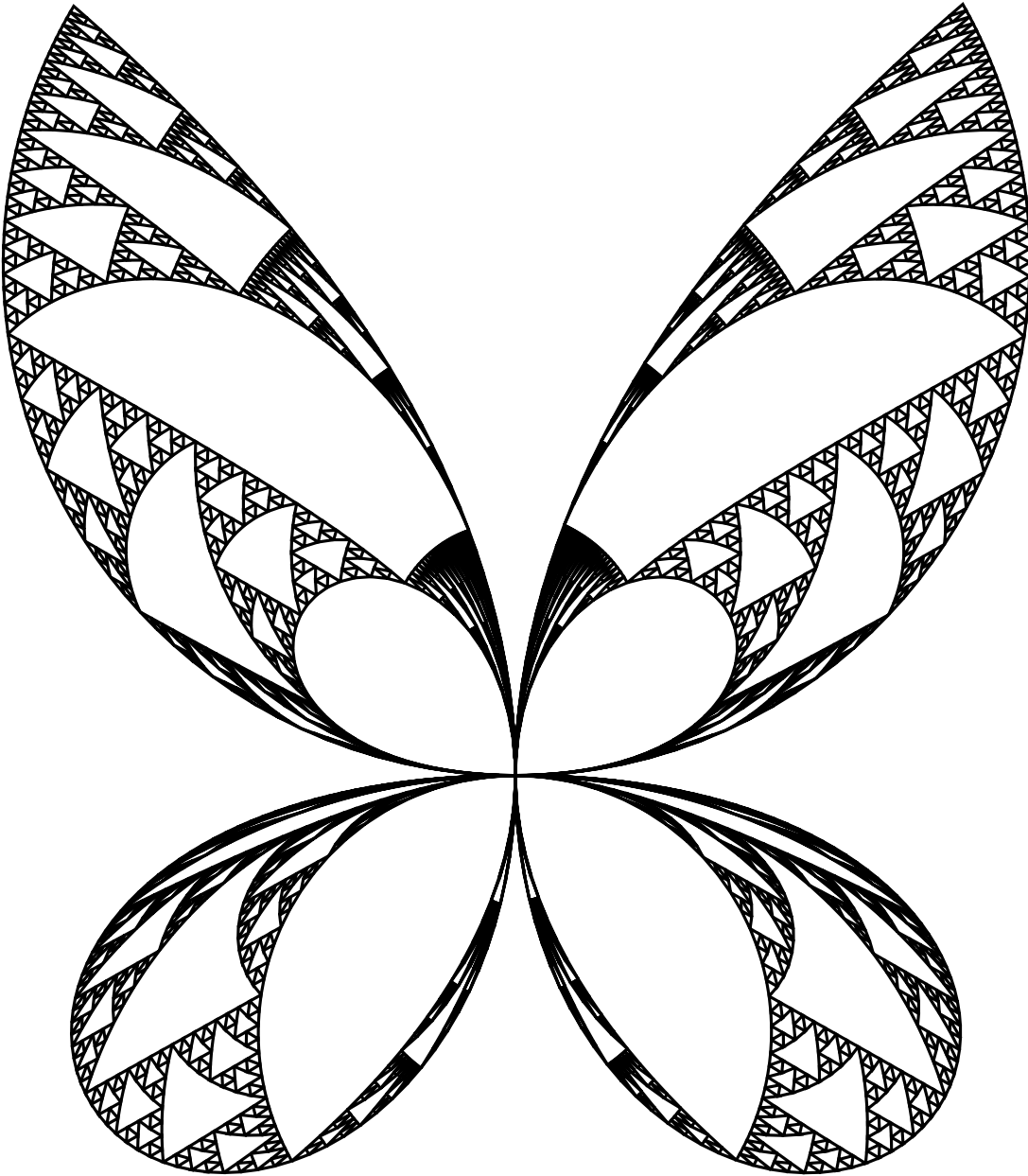
Dr. Andréa Brito Latgé

Dr. Marcos Gonçalves de Menezes

Dr. Roberto Hiroki Miwa (UFU)

Dr. Yutao Xing

Lucas Lopes Lage

Resumo

Neste trabalho estudamos propriedades eletrônicas de sistemas quasi-unidimensionais baseados em carbono. Por meio do método Tight-Binding e do formalismo de funções de Green aplicadas ao modelo de Landauer foi possível obter estruturas de bandas, densidade de estados e condutâncias eletrônica das redes propostas. O trabalho está subdividido entre o estudo de propriedades eletrônicas em geometrias do tipo favo de mel, em grafeno, α-graphyne e kagomé, definidas aqui como *stantard* e geometrias fractais obtidas pela inserção de triângulos de Sierpinski em cadeias carbônicas. O aparecimento de fenômenos fractais em geometrias stantard pode ser observada por meio da ação de um campo magnético externo no movimento dos elétrons da rede. Nesta situação, o espectro de energia em função do fluxo magnético nos fornece uma figura fractal denominada "Hofstadter Butterfly". Inicialmente apresentamos a teoria e modelos que possibilitam o estudo das propriedades eletrônicas de monocamadas, bicamadas e bicamadas rodadas das redes propostas. Resultados de estruturas eletrônica, densidade de estados eletrônicos e de transporte são explorados ao longo do trabalho. As redes fractais são apresentadas e em particular nos concentramos em sistemas compostos por triângulos de Sierpinski. Motivados por resultados experimentais encontrados recentemente na literatura, desenvolvemos modelos moleculares simplificados para descrever cadeias moleculares geradas a base de triângulos de Sierpinski. Esses modelos foram capazes de reproduzir de forma bastante satisfatória a partir de mapas de densidades locais de cargas com imagens do microscópio de tunelamento quântico. Nossos cálculos revelam o aparecimento da auto-similaridade destes sistemas nas respectivas propriedades eletrônicas. Nossos estudos se mostraram bastante promissores para futuras aplicações no desenvolvimento de dispositivos nanoscópicos. **Palavras-Chave:** grafeno-flat band-fractal-propriedades eletrônicas

Abstract

In this work we study the electronic properties of quasi-unidimensional carbon-based systems. Through the Tight-Binding method and the formalism of Green's functions applied to the Landauer model, it was possible to obtain band structures, density of states and electronic conductance of the proposed systems. The work is divided between the study of electronic properties of honeycomb, graphene, α-graphyne and kagomé geometries, defined here as *stantard* and fractal geometries obtained by inserting Sierpinski triangles into carbon chains. The emergence of fractal phenomena in standard geometries can be observed through the action of an external magnetic field on the movement of lattice electrons. In this situation, the spectrum of energy as a function of the magnetic flux gives us a fractal figure called "Hofstadter Butterfly". Initially we present the theory and models that allow the study of the electronic properties of monolayers, bilayers and bilayers rotated of the proposed networks. Results of electronic structures, density of electronic and transport states are explored throughout the work. Fractal networks are presented and in particular we focus on systems composed of Sierpinski triangles. Motivated by experimental results recently found in the literature, we developed simplified molecular models to describe carbon chains generated on the basis of Sierpinski triangles. These models were able to reproduce quite satisfactorily from maps of local charge densities with scanning tunneling microscope images. Our calculations reveal the appearance of the self-similarity of these systems in the respective electronic properties. The studies of the properties of the systems discussed here proved to be fundamental for future applications in the development of nanoscopic devices.

Keywords: graphene-standard lattices-flat band-fractal-electronic properties

Acknowledgments

I would like to thanks to everyone who stayed with me along through this hard times that we all being living.

First of all, I would like to thanks my mother for giving me the necessary support to move on, dispite all things that happened with us.

A very special thanks to my supervisor Andrea Latgé, with whom I could develop a great friendship. In addition, she is responsible for keeping alive my passion for physics and encourage all my academical desires during this period. I am very grateful for all her support.

A passionate thanks also to Jessica, my fiancee, my little peach fruit, my confidant, my eternal Miwa, my everything. You always had the greatest patience and affection with me. Whenever I needed, you were there during all these difficult times I went through. Thank you so much, you are the happiest surprise that life gave to me.

I could not fail to thank my dear friends from the <Bra|Ket> group, especially Dimas who gave me all the support when I needed it. Also, to my friends from DC group who I am sure that will stay with me during my life walk.

Last but not least, I would like to thank the research funding institutions such as CAPES, CNPq and FAPERJ that made possible my sub-existence during this period. As well as all the members and partners from my research group and all the UFF staff.

Contents

List of Figures

Introduction

The graphene is a bidimensional system believed for some time as being merely a toy model. Theoretical studies predict an unstable surface due to the fact that thermal fluctuations should be larger than the binding forces that bring atoms together. The formation of curved structures such as fullerenes and nanotubes are then expected to happen in graphene systems [1]. This belief comes down when the physicisst A. Geim e K.Novoselov obtained by exfoliation of graphite a single sheet, denominated later as graphene. Graphene is a semi-metal in the the the bulk, with Dirac cones [2] at the K points of the Brillouin Zone (BZ). The Dirac cones are energy regions with linear dispersion where the electron have a high group velocity, near to 10^6ms^{-1}, and null effective mass [3].
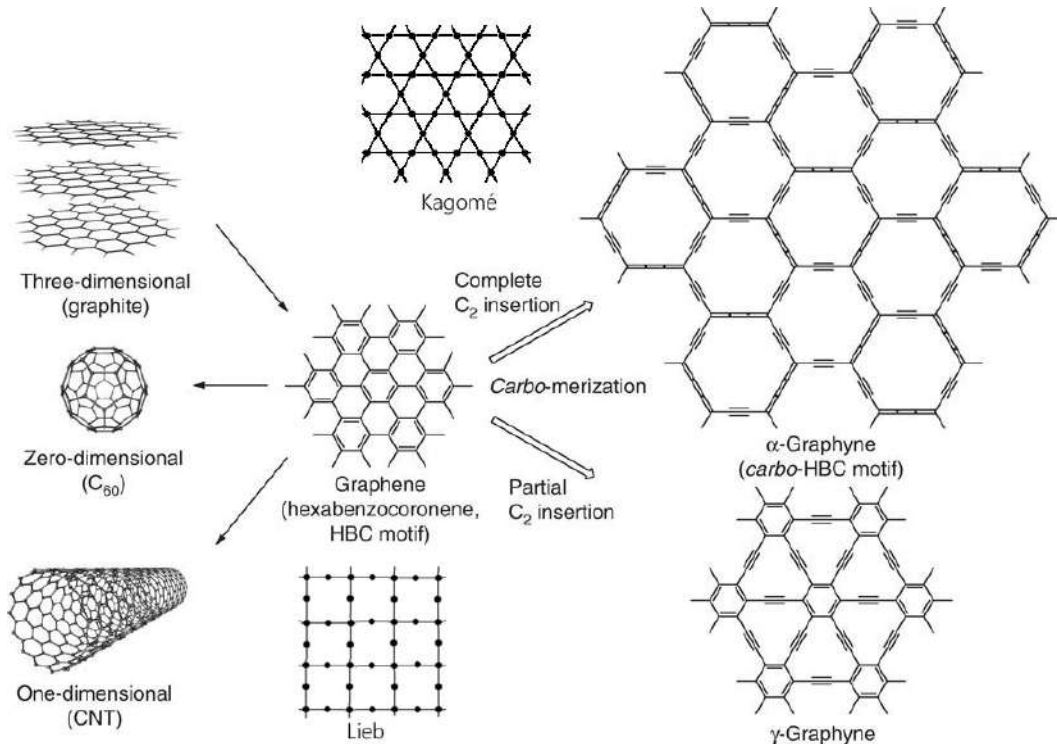
Figure 1: Carbon allotropes: From 0-D to infinite systems. Adapted from Ref.[4]

The subsequent confirmation that graphene exhibit a number of interesting physical responses, such as high mobility, ballistic electronic propagation, mechanical flexibility, among others, have

transformed graphene a protagonist in condensaded matter research [5]. Actually, after the graphene realization, a gold rush for experimental synthesis of graphene sheets begun. Also, several experimental techniques such as bottom-up assembly [6] and chemical vapour deposition (CVD) [7] were developed to reproduce the results obtained by different groups. Alternatively, new bidimensional hexagonal materials that were already theorized in the past, like graphyne lattices and Kagomé, predicted many years before the graphene discovery, started being investigated and also synthetized. As illustred in Fig. 1 the first traditional Kagomé lattice, theorized by I.Syozi in 1951 [8] gave rise to other decorated lattices such as Kagomé Honeycomb (originally proposed as a metal framework) [9], Lieb lattice, graphyne family, and others. In metallic materials like α-graphyne, or semi-metals in the graphene case, the electrons behave like a gas, and the corresponding electronic wave functions are delocalized throughout the lattice. Kagomé systems are in general semiconductors with a flat band near the Fermi Level. The flat band is a direct result from destructive interference between the electrons in the system [10].

Created from the insertion of acetylenic bonds (sp hybridization) between the graphene aromatic rings, the graphyne (Gy) proved to be a promising material. Since the theoretical proposal of R.H.Baughman *et al* [12] in 1987, several experimental attempts have been reported in the literature using chemical/mechanical routes for the synthesis of some of the several variations of the Gys [13, 14, 15, 16, 17], such as (α, β, γ and $6, 6, 12$)-graphyne shown in Fig.2. With even more acetylenic linkages, we have also the graphydine [18]. Several versions of graphyne have also emerged: multilayers, nanofoams, nanotubes, 0D-3D [19, 20] allotropes, among others. In addition, technological applications as proposed by Zhang *et al* [21], reported the use of graphyne as an anode in Lithium batteries, since energy storage and diffusion were better compared to graphite. Another possible application is as a desalination agent, reaching 100% of rejection of almost all ions present in seawater, including Na+, Cl-, Mg2+, K+ and Ca2+, two orders of magnitude higher than in commercial membranes [22]. In the second Chapter we discuss the electronic properties of bilayered graphyne, consisting of two graphyne layers stacked on top of one another and other interesting physical properties of such carbon based systems.

Almost every graphyne family and molecular kagomé structure had been already synthesized
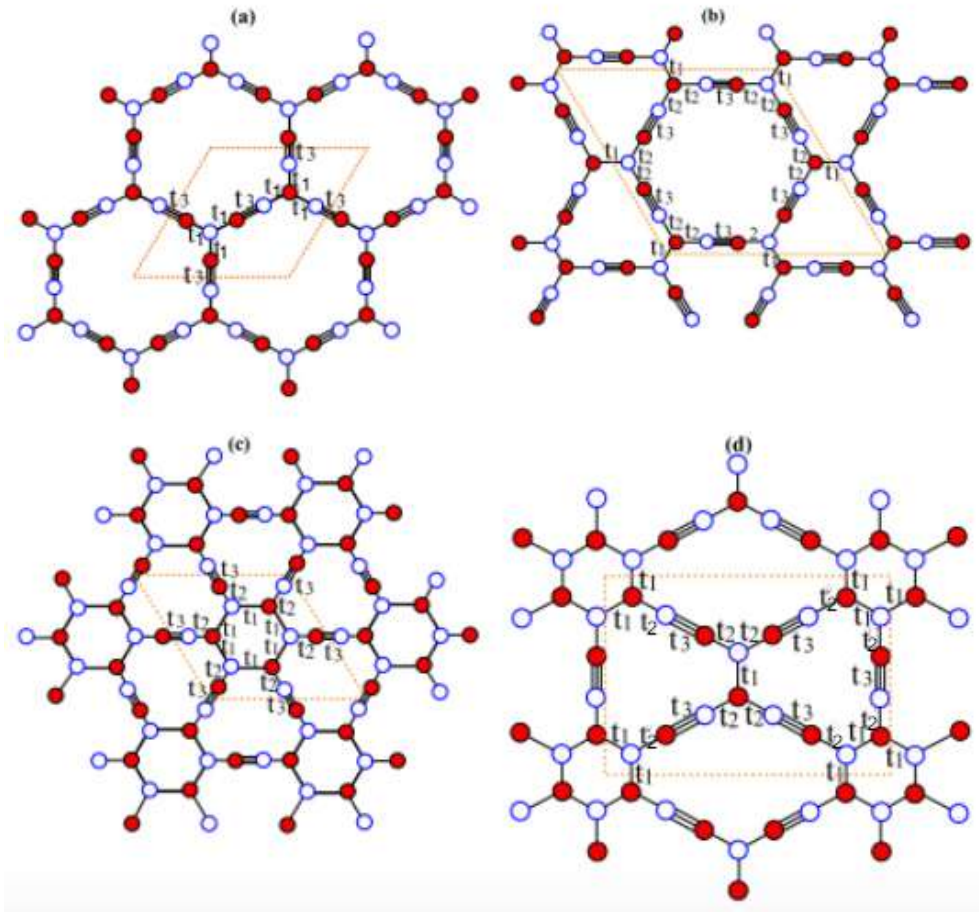
Figure 2: Molecular representation of 4 graphyne families:. (a) α-graphyne, (b) β-graphyne, (c) γ-graphyne, and (d) 6,6,12-graphyne. [11]

[9, 23], pushing the development of new models to describe them. It's important to mention that other system configurations are possible to be realized experimentally and theoretically described, like flakes, bilayers and twisted bilayers. Monolayered and bilayered graphene systems are already largely explored in the literature [2, 24, 25]. In the case of bilayer graphene, two configurations between the layers are possible [see Fig. 3(a)]; direct AA and bernal AB stackings, leading a metallic character for pristine graphene bilayer, which could be broke by an applied perpendicular electric field [26, 27]. Moreover, by rotating one layer relative to the other, Jarillo and his colleagues found the called magic-angle in twisted bilayer graphene (TBG) [28]. A superconducting transition evidenced in TBG started, at 1.7K, started a new rush around twisted materials, giving birth to new areas as the twistronics [29].
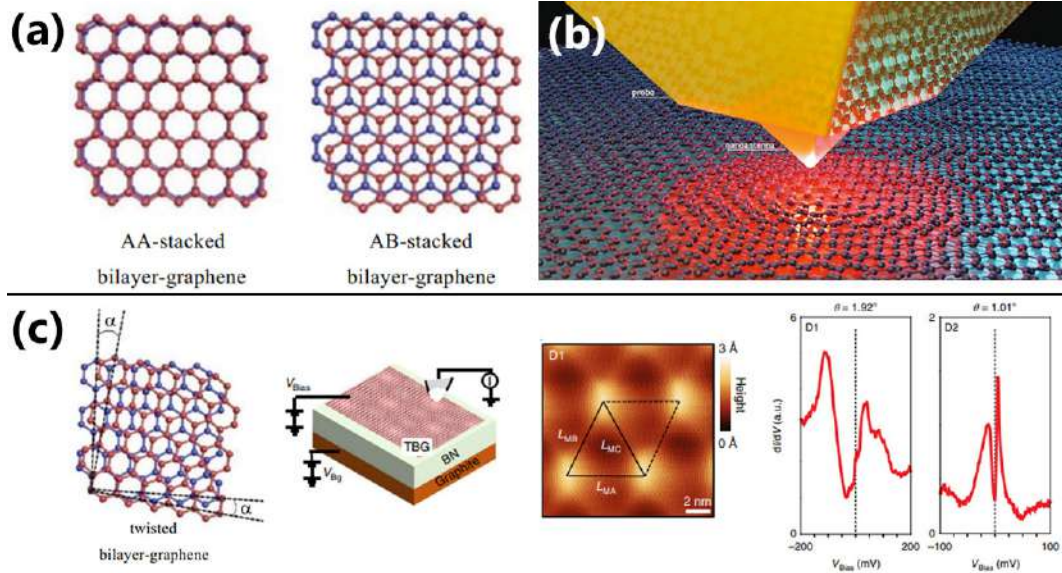
Figure 3: (a) AA and AB graphene stacking scheme. (b) Jorio group STM tip. (c) From left to right: TBG and STMs sample schemes, Charge density obtained via STM and increasing peak observed for low angles in the tunneling current. Adapted from.[27, 30, 31]

As it will be better pointed in the next sections regarding to the Moiré effect, the commensurable angles are responsible to the emergence of TBG supercells. This leads the possibility of obtaining Hofstadter-like butterflies, which are fractal figures [32]. Because of the large unit cells, the TBG showed up as a propper scenario to explore fractal properties in matter. Shortly, the Hofstadter butterflies are obtained when a confined electron in a thin periodic layer interacts with a perpendicular magnetic field promoting changes in the accessible electron energy. The corresponding electronic structure as a function of the magnetic field intensity shows fractal patterns, similar to butterfly wings. The effects of this interaction is explored in Sec. 3.2.

Concerned to experimental aspects, the thin layers of graphene can be manipulated as an origami using an experimental technique called Scanning Tunneling Microscopy (STM). Very recently, a Brazilian experimental group in UFMG led by Ado Jorio, have proposed and developed a new microscope tip with a pyramidal shape able to accurately measure nanometric systems (resolution of 1nm) and sharp spatial control [31, 33]. To rotate and create the TBGs they have manipulated the graphene layers with the new developed STM tip as illustrated in Fig. 3(b) [33]. The STM apparatus and experimental results are observed in Fig. 3(c). Also, for small angles, as depicted in mentioned figure, the results from the tunneling current reveals a sharply-angle dependent peak.

The STM creation gives for the first time the possibility of a direct real-space measurement, contrary to what was developed, for example, with the X-Ray diffraction experiments. Since then, the STM proved to be an important tool in the study of electronic properties of different materials. The great deal of having a microscope were the resolution is near from the unit in nanometric scale, is to explore a new world of properties of matter that was not available before. In fact, the main goal in any microscope measure is its amplifying power or resolution. Optical microscopes have limited resolution which qualitatively stipulates the limits that two sample points can be identified separately. More details of the STM theory are discussed in Chapter 1. Briefly, the measure is made using the quantum tunneling effect between the sample and the microscope tip. This is possible due to a gate voltage applied between them. With this experimental setup, we can obtain information about the system electronic topography by varying the perpendicular distance (d) among the tip and the lattice. Alternatively, we can obtain the charge density distribution around the lattice positions, for each energy value, considering d fixed.
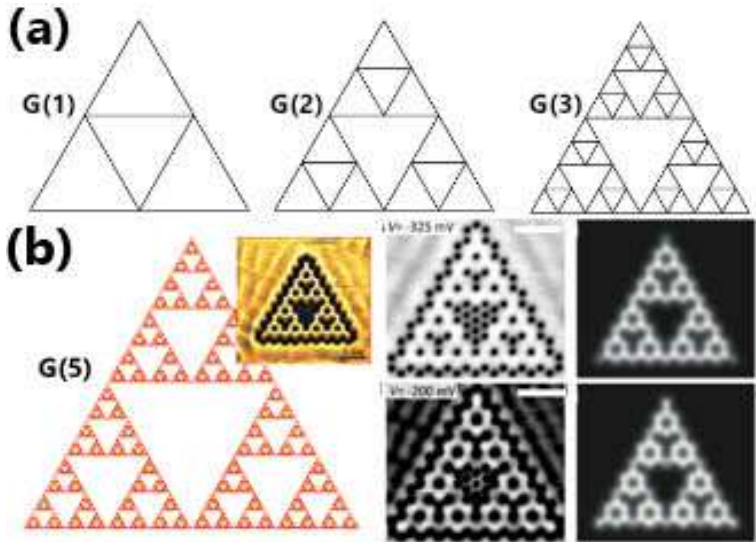
Figure 4: (a) Sierpienski Triangle generations (b) Experimental results of constructing ST flakes with a STM tip taken from Ref. [34].

After the brief introduction to carbon-based nanomaterials, their background and experimental measurements, we introduce in the following, the concept of fractals and discuss some results concerning the fractality in nanostructured systems. Fractal sets are characterized by their infinite self-similarity property, i.e., each part of the set has the same or approximately the same shape of the whole set. A particular example, is the Sierpinski Triangle (ST) [see Fig. 4]. Besides the fact that its constructed by 2D equilateral triangles, subdivided recursively into smaller equilateral triangles, the ST has a fractal dimension $D \approx 1.585$. Apart from a mathematical object, recently [34], the ST flakes becomes an experimental reality by manipulating CO molecules on Cu(111) surfaces with the STM tip. It was possible to build and measure the charge density in a real ST flake. Then, confronting experimental and theoretical models, the group concluded that the electrons behaves like a particle in a fractal dimension in such systems.

Mathematical fractal areas are hard to be measured. The "Koch Coastline" is a fractal figure based on Koch's snowflakes. For higher orders, as in Fig. 5(a), it is very similar to geographic coastlines seen from space photographs. Imagine that we want measure the total line-area occupied by a coastline following the Koch growth. We will certainly have a problem, since there are infinity generations, each one changing the topography of the coastline. Interested in this problem, Hausdorff developed the box-counting method [35, 36] to calculate the dimension of such figures.
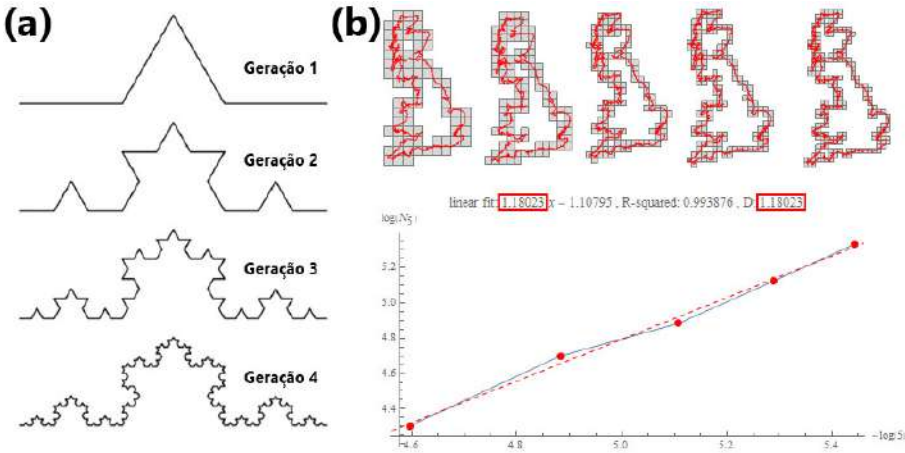
Figure 5: (a) Koch Coastline generations (b) Box-Counting on Grain Britain coast. Addapted from Ref. [37].

The box-counting method is based on the dimension calculation of the figure by filling it with

squares. The measure of the Great Britain coast dimension using the box-counting method [see top part of Fig. 5(b)] is made by filling it with different $N(r)$ squares with size r. After that, the dimension is obtained by the slope coefficient of the $log(N) - log(r^{-1})$ plot. In the bottom part of Fig. 5(b), we see the box method applied; for each dot in the graph we have a certain amount of boxes filling the coast.

Usually, a fractal is a figure with infinite self-similarity. Here in this work, we will call a finite fractal (pre-fractal in literature), simply as a fractal, in which the N-th iteration number will be given by the $G(N)$ orders. Motivated by the emergence of fractals in nanoscopic systems [38, 39, 40], in Fig. 6 we have illustrated several examples of STs based on different structures. Separated in the literature as conventional, hexagonal and graphene zigzag and armchair flakes. In the present work we also propose the Kagomé honeycomb ST flake, as well in the zigzag and armchair configurations.
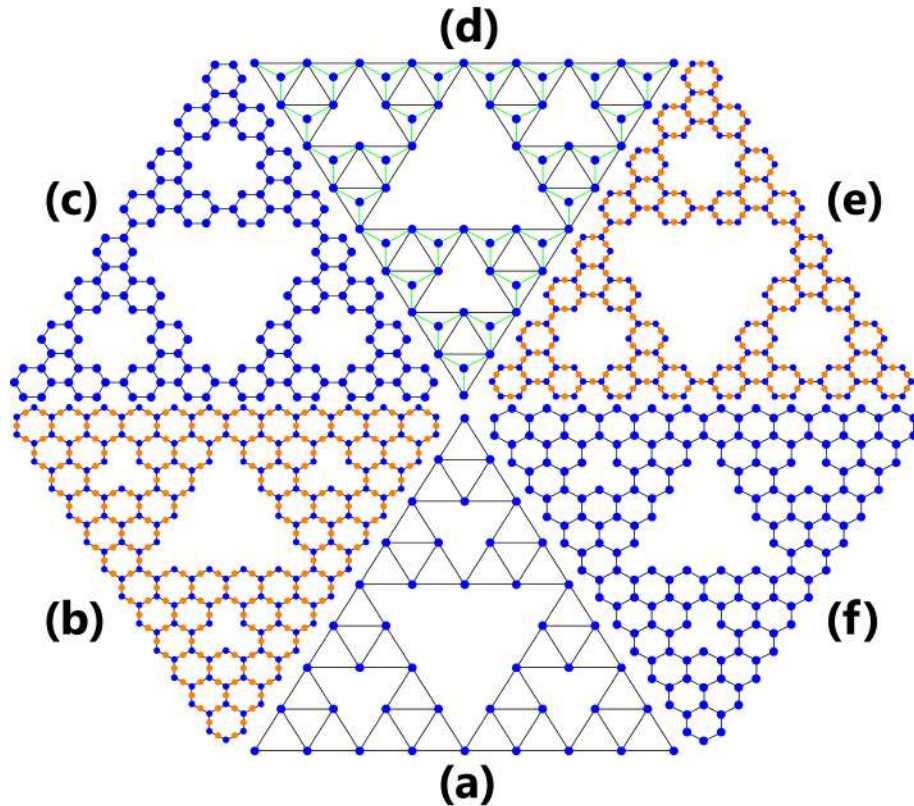
Figure 6: Variations of G(3) Sierpinski Triangle flakes: (a) Conventional ST, (b) Zigzag-Kagomé-Honeycomb ST (Z-KHST), (c) Armchair-Graphene ST (A-GST), (d) Hexagonal ST (HST), (e) Armchair-Kagomé-Honeycomb ST (A-KHST), and (f) Zigzag-Graphene ST (Z-GST).

More than a mathematical abstraction, fractals built with a finite number of iterations are physically applicable like in fractal circuits and antennas [41], fractals used in the synthesis of insulator thermal porous media [42], fractal wave guides as a possibility of a "spatial compression of light energy" [43, 44], and more recently the synthesis of Sierpinski composites [34, 45, 46] and models describing similar fractal [38, 47]. Lately, 1D molecular chains using STs as building blocks have been reported [45, 46] using low-temperature STM as depicted in Fig. 7. Experimental methods using self-assembly [48, 49, 50] and templating [51, 52, 53] are being used to synthesize ST flakes and nanoribbons with transition metals and metal-organic composites. The systems were grown on Au(111) and the success of the chain formation depends on the molecular coverage and matching between molecular size and surface lattices. Also, 2D crystals consisting of ST units are reported by exploiting benzene-like molecules and Fe atoms on Au(111) by combining molecular design and epitaxy control [54].
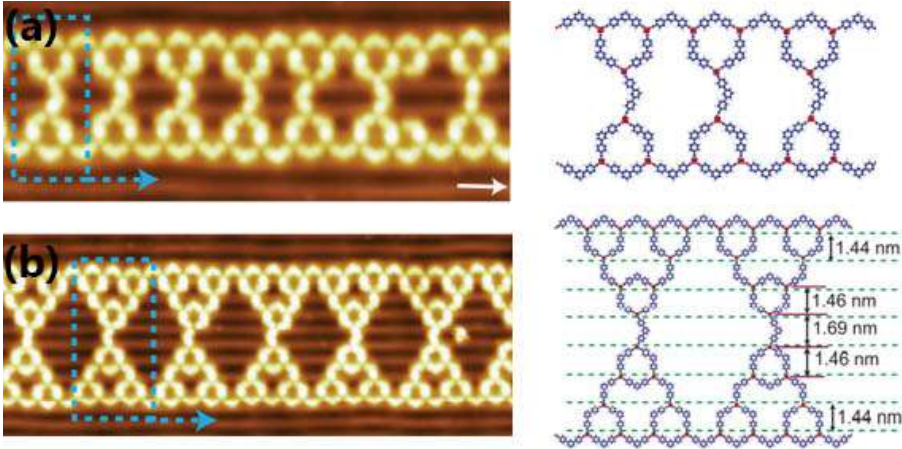
Figure 7: Experimental STM results and lattice model of BPyB molecules [51]. Mirrored ST chains: (a) G(1) and (b) G(2)

.

Nowadays the understanding of the electronic properties of these new materials is a very important technological aspect to the computational advances and device development evolution. The "nanofication" of the latest processors highlight even more the physical limit of the electronic components related with the Moore's law. The use of fractal lattice was reported as wave guide for photonic lattice [39], which could be employed in the construction of quasi-analog computing in

photonics [55].

In summary, we study in this work the electronic properties of nanostructures systems separated in two types. The first one, presenting well known regular geometries (honeycomb lattice), in which, in this work are denoted by standard geometries. And the fractal ones, mainly defined by the construction of fractal lattices or by the insertion of standard geometries into the ST flakes. It is important to mention that a connection between both physical systems can be made, for instance, by considering the case in which a magnetic field is applied perpendicularly to a 2D lattice, producing fractal patterns in the energy spectra, like the famous Hofstadter Butterfly signatures.

Chapter 1

Theory & Background

*To understand the rose, one
person may use geometry and
another the butterfly.*

Claudel, 1929

The quantum mechanical theories have been extensively verified experimentally and even nowadays its predictions continue motivating physics measurements. Flash drives and transistors use the transport theory developed for tunneling and drifted electrons in materials. Also, different under rated mathematical tools turned to be very useful for quantum field theories in condensed matter, as group theory and topology. Symmetry operations on Hamiltonian matrices are provided by operators that follow the Hilbert space formulation of quantum mechanics. All these theories are integrated forming a solid theoretical framework basis that moves the scientific advances though the centuries. In this chapter we discuss some of these condensed matter theories that are applied directly to help understanding the physics of the carbon systems proposed in this work.

1.1   Tight-Binding Method

The tight-binding (TB) approximation was suggested by Bloch in 1928 to calculate the state occupancy of periodic crystalline systems. The TB method is suitable for describing systems in

which electrons are strongly bound to atoms and interact weakly with neighboring potentials. In this context, the wave functions of these electrons will be quite similar to those of the corresponding free atom. Electronic wave functions are constructed from a linear combination of atomic orbitals (LCAO) belonging to different neighboring atoms. In the case of the materials studied here, due to the symmetry of the orbitals of the carbon atom, the transport is carried out through the π bonds of the p_z orbitals. The TB model allows us to calculate the band structures in the entire Brillouin zone, with the advantage of having a low computational cost.

Due to the translation symmetry of the crystalline systems given by the lattice vectors $\vec{a_i}$, any function that satisfies the Bloch theorem could be represented by itself multiplied by a phase [56], i.e.,

$$T_{\vec{a_i}}\Psi = e^{i\vec{k}.\vec{a_i}}\Psi, \quad (i = 1, 2, 3), \tag{1.1}$$

where T is the translation operator over the direction of the vector $\vec{a_i}$, and $\vec{k}$ is the Bloch wave vector. Any wave function $\Phi_{\vec{k}}(\vec{r})$ that satisfies the condition above[1], could be defined as a sum over the atomic wave function orbitals $\varphi(\vec{r} - \vec{R})$ for the j-th site, as

$$\Phi_{j\vec{k}}(\vec{r}) = \frac{1}{\sqrt{N}}\sum_{\vec{R}}^{N} e^{i\vec{k}.\vec{R}}\varphi(\vec{r} - \vec{R}), \quad (j = 1, 2, ..., N), \tag{1.2}$$

with $\vec{R}$ being the atom position, in terms of the lattice vectors, and N the number of unit cells, mapping the atoms for first, second, and others next-neighbors. If the wave function above is a good candidate for a Bloch orbital, then due to the translation invariant symmetry a displacement by the lattice parameter a could not change the orbital function

$$\begin{aligned}
\Phi_{j\vec{k}}(\vec{r} + \vec{a}) &= \frac{1}{\sqrt{N}}\sum_{\vec{R}}^{N} e^{i\vec{k}.\vec{R}}\varphi(\vec{r} + \vec{a} - \vec{R}) \\
&= e^{i\vec{k}.\vec{a}}\frac{1}{\sqrt{N}}\sum_{\vec{R}-\vec{a}}^{N} e^{i\vec{k}.(\vec{R}-\vec{a})}\varphi[\vec{r} - (\vec{R} - \vec{a})] \\
&= e^{i\vec{k}.\vec{a}}\Phi_{j\vec{k}}(\vec{r}).
\end{aligned} \tag{1.3}$$

Thus, $\Phi_{j\vec{k}}$ is a good candidate for a Bloch orbital function and the wave function $\Psi_{j\vec{k}}(\vec{r})$ is defined

---

[1]Which means that $\vec{k}$-index is now a good quantum number

as a linear combination of Bloch's functions, as

$$\Psi_{j\vec{k}}(\vec{r}) = \sum_{j'=1}^{N} C_{jj'}(\vec{k})\Phi_{j'\vec{k}}(\vec{r}) \ . \tag{1.4}$$

The coefficients $C_{jj'}$ are determined by the j-th eigenvalue expressed as

$$E_j(\vec{k}) = \frac{\langle \Psi_j | H | \Psi_j \rangle}{\langle \Psi_j | \Psi_j \rangle} \ , \tag{1.5}$$

with H being the Hamiltonian of the system. Now, changing the index and substituting Eq. 1.4 into Eq. 1.5, we have

$$E_i(\vec{k}) = \frac{\sum_{jj'=1}^{N} C_{ij}^* C_{ij'} \langle \Phi_{j,\vec{k}} | H | \Phi_{j',\vec{k}} \rangle}{\sum_{jj'=1}^{N} C_{ij}^* C_{ij'} \langle \Phi_{j,\vec{k}} | \Phi_{j',\vec{k}} \rangle} = \frac{\sum_{j,j'=1}^{N} H_{jj'}(\vec{k}) C_{ij}^* C_{ij'}}{\sum_{j,j'=1}^{N} S_{jj'}(\vec{k}) C_{ij}^* C_{ij'}} \ , \tag{1.6}$$

where $S_{jj'}(\vec{k}) = \langle \Phi_{j\vec{k}} | \Phi_{j'\vec{k}} \rangle$ are the orbital overlap matrix elements for first neighbor atoms, and the integral matrices $H_{jj'}(\vec{k}) = \langle \Phi_{j\vec{k}} | H | \Phi_{j'\vec{k}} \rangle = \epsilon \delta_{jj'} - t \delta_{jj' \pm 1}$, with ϵ being the on-site energy, and t the electronic hopping terms between the sites j and j'. The coefficients C_{ij}^* are chosen as to minimize the eigenvalues $E_i(\vec{k})$. Fixing $C_{ij'}$, we have

$$\frac{\partial E_i(\vec{k})}{\partial C_{ij}^*} = \frac{\sum_{j,j'=1}^{N} H_{jj'}(\vec{k}) C_{ij'}}{\sum_{j,j'=1}^{N} S_{jj'}(\vec{k}) C_{ij}^* C_{ij'}} - \frac{\sum_{j,j'=1}^{N} H_{jj'}(\vec{k}) C_{ij}^* C_{ij'}}{\left(\sum_{j,j'=1}^{N} S_{jj'}(\vec{k}) C_{ij}^* C_{ij'}\right)^2} \sum_{j,j'=1}^{N} S_{jj'}(\vec{k}) C_{ij'} = 0. \tag{1.7}$$

Multiplying then, both sides by $\sum_{j,j'=1}^{n} S_{jj'}(\vec{k}) C_{ij}^* C_{ij'}$ and substituting $E_i(\vec{k})$ from Eq.(1.6) in the second term of Eq.(1.7), we obtain obtemos

$$\sum_{j,j'=1}^{N} H_{jj'}(\vec{k}) C_{ij'} = E_i(\vec{k}) \sum_{j,j'=1}^{N} S_{jj'}(\vec{k}) C_{ij'} \ . \tag{1.8}$$

By defining a column vector,

$$C_i = \begin{bmatrix} C_{i1} \\ C_{i2} \\ \vdots \\ C_{iN} \end{bmatrix}, \tag{1.9}$$

we get

$$\mathcal{H}C_i = E_i(\vec{k})\mathcal{S}C_i. \tag{1.10}$$

Note that Eq. 1.1 is still a N-term expression. Transposing the left side to the right we get,

$$[\mathcal{H} - E_i(\vec{k})\mathcal{S}]C_i = 0.$$

The only non-trivial solution is for $[\mathcal{H} - E_i(\vec{k})\mathcal{S}]$ non-invertible, so the eigenfunction is determined by solving the following **secular** equation,

$$det[\mathcal{H} - E(\vec{k})\mathcal{S}] = 0. \tag{1.11}$$

From this equation we can obtain the dispersion relation of the energy inside the Brillouin zone, for a certain direction of the wave vector $\vec{k}$. In the orthogonal approximation, the overlap term is equal to one, and there are several ways to express the energy of the system in function of its own symmetries. In the next Section, we apply the Tight-Binding method to a Kagomé honeycomb nanoribbon to illustrate the use of theory.

1.1.1   Application: Kagomé Honeycomb Nanoribbon

Here we introduce some aspects of the Kagomé honeycomb nanoribbons (KHNRs) and perform the orthogonal[2] TB calculations to derive the electronic structure and the density of state in such systems. Usually, the Kagomé honeycomb (KH) lattices are composed by covalent organic frameworks, with complex unit cells and different band structure features, as depicted in Fig.1.1-(a).

---

[2]Approximation were the Bloch orbitals of each atom are orthogonal between then, making the overlap matrix (S) in the secular equation 1.1 equal to identity

Otherwise, in simplified models, the lattice is treated as a decorated graphene with on-site energy potentials $\pm\varepsilon$, for each sub-lattice as shown in Fig.1.1-(b), with white and black atoms [9].
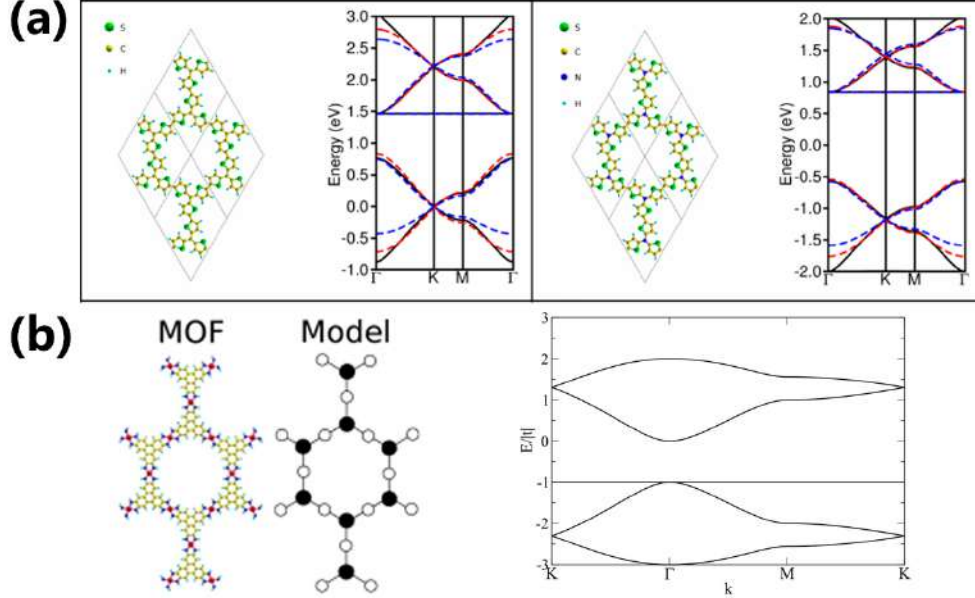
Figure 1.1: (a) Possible atomic configurations for Metal Organic Framework (MOF) KH and (b) MOF configuration and the simplified model with its band structure for $\varepsilon < 0$. Adapted from Ref. [9].

Despite the fact that a KH lattice, also exhibits hexagonal symmetry, like graphene, a band gap $E_g = 2\varepsilon$, within the adopted model, ensuring a semiconductor state in both bidimensional [Fig. 1.1(b)] and quasi-unidimensional (nanoribbons) [Fig.1.2]. This occurs due to the symmetry break in the unit cell, by the insertion of intermediary atoms between the graphene lattice, which gives asymmetrical sub-blocks in the Hamiltonian as will be discussed.

Fig. 1.2 shows an example of a zigzag kagomé honeycomb nanoribbon (Z-KHNR). In order to preserve and to explore the system symmetries, we define the sequence of unit cells that are used in the computation code, illustrated with colored dashed rectangles in green, yellow and blue, representing nanoribbons with sizes N=1, 2, and 3, respectively. An arbitrary site index is chosen in black for kagomé and white for graphene unit cells. We can see that for the 3-Z-KHNR the gap size is proportional to $E_g = 2\varepsilon$ like in the bulk case. Due to a single flat state at $E = -0.25t$ the electronic band structure is is not complete symmetric about the fermi level. The emergence of a flat state is an important feature of the Kagomé systems [10].
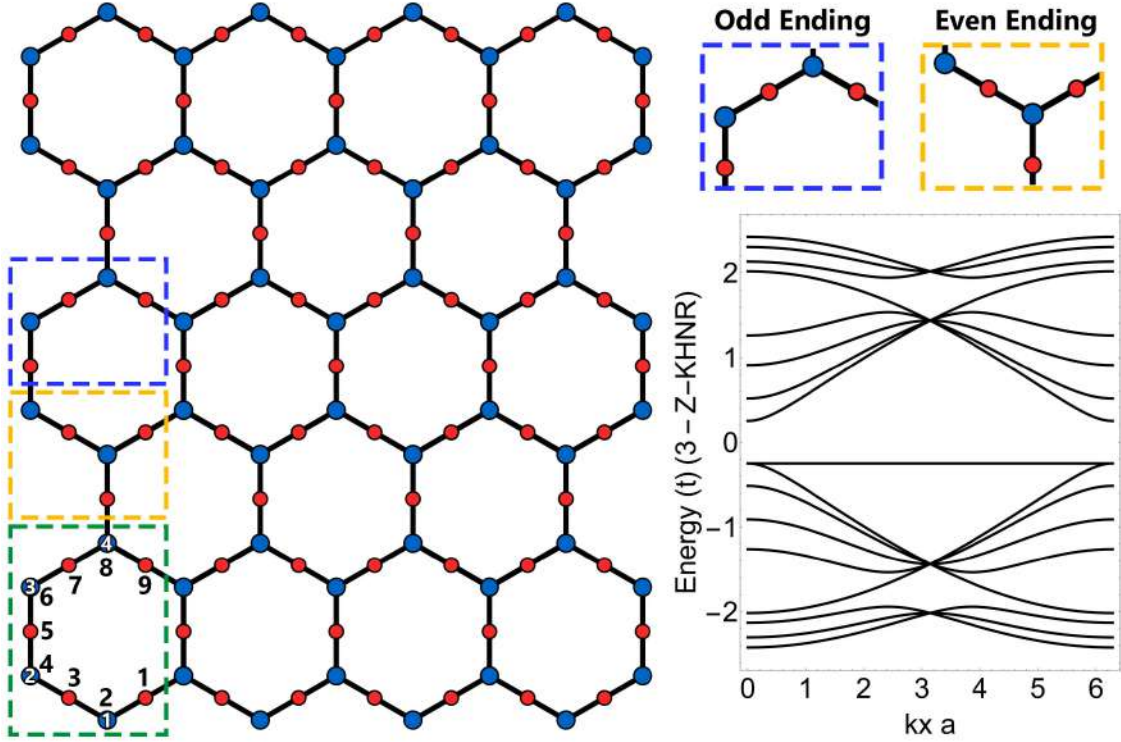
Figure 1.2: Growth illustration of the KHNRs, highlighting odd and even edges that alternate as the system increases. Red and blue sites, denotes on-site energies settled as $\varepsilon = \pm 0.25t$

The Hamiltonian used to calculate the electronic properties of this system is given as

$$H = \sum_i \varepsilon_i c_i^\dagger c_i \; - \; \sum_{<i,j>} t_{i,j} c_i^\dagger c_j \; + \; h.c. \tag{1.12}$$

with ε_i being the on-site energy for each atom located at site i, defined as $\pm 0.25t$ for blue and red sites, respectively, $c_i^\dagger$ (c_i) is the creation (annihilation) operator of an electron on site i, and $t_{i,j}$ is the hopping energies for nearest neighboring atoms. Is important to stress that the hopping values from Kagomé and Graphene systems described in Fig. 1.2 are different, however, for simplicity here we denote both hopping terms as t^3.

The Hamiltonian matrix (H_K) for N=1 (green unit cell in Fig. 1.2 with 9 atoms) is defined by a 9x9 matrix

---

[3]It is important to stress that the hopping value for the Graphene and Kagomé cases are different, but, to not load the notation, here we define both as t.

$$H_K = \left(\begin{array}{cccc|c|cccc} -\varepsilon & t & 0 & te^{iak} & 0 & 0 & 0 & 0 & 0 \\ t & \varepsilon & t & 0 & 0 & 0 & 0 & 0 & 0 \\ 0 & t & -\varepsilon & t & 0 & 0 & 0 & 0 & 0 \\ te^{-iak} & 0 & t & \varepsilon & t & 0 & 0 & 0 & 0 \\ \hline 0 & 0 & 0 & t & -\varepsilon & t & 0 & 0 & 0 \\ \hline 0 & 0 & 0 & 0 & t & \varepsilon & t & 0 & te^{-iak} \\ 0 & 0 & 0 & 0 & 0 & t & -\varepsilon & t & 0 \\ 0 & 0 & 0 & 0 & 0 & 0 & t & \varepsilon & t \\ 0 & 0 & 0 & 0 & 0 & te^{iak} & 0 & t & -\varepsilon \end{array} \right) \qquad (1.13)$$

As expected, the matrix dimension is given by the number of atoms in the unit cell. Following the counting in the figure, for first neighbors between different unit cells, a phase is added. Moreover, the hamiltonian of graphene H_G can be obtained by removing the red atoms from the green unit cell, leaving four blue atoms located in the hexagon vertices. The corresponding Hamiltonian matrix is

$$H_G = \left(\begin{array}{cccc} \varepsilon & t\left(1 + e^{iak}\right) & 0 & 0 \\ t\left(1 + e^{-iak}\right) & \varepsilon & t & 0 \\ 0 & t & \varepsilon & t\left(1 + e^{iak}\right) \\ 0 & 0 & t\left(1 + e^{-iak}\right) & \varepsilon \end{array} \right) \qquad (1.14)$$

Comparing the sub-blocks in H_K [Eq. 1.13] with the H_G [Eq. 1.14], we notice an alternating sign value for the on-site energies in the H_K matrix. This is in accordingly with is expected for the Kagomé features. For that reason, the diagonal terms of these sub-blocks can be written in terms of the generalized 4D Z-Pauli matrix σ_Z^{4D} as,

$$D1 = -\varepsilon \ \sigma_Z^{4D}$$

$$D2 = \varepsilon \ \sigma_Z^{4D} \qquad (1.15)$$

where D1 and D2 stand for the diagonal terms of the first and second highlighted 4x4 sub-blocks of H_K, respectively. The σ_Z^{4D} is obtained by the tensorial product $I_2 \otimes \sigma_Z$, with I_2 and σ_Z being the 2x2 identity and Pauli matrices. As discussed in the Appendix. A, when the diagonal terms of the Graphene Hamiltonian (H_G) are proportional to σ_Z, both time-reversal and spatial symmetries of the hexagonal system are broken, with that, the protected metallic state observed for zigzag graphene nanoribbons [see Fig. 1.3(a)], is changed to a semiconductor character [57, 58]. Hence, for zigzag kagomé, a band gap proportional to 2ε is reached [see Fig. 1.3(b)]. Further effects, such as external magnetic, electric fields and strain [59, 60, 61, 62] could also be employed to break these symmetries and change the electronic properties in that systems. The electronic energy bands and density of states of both systems are shown in Fig. 1.3
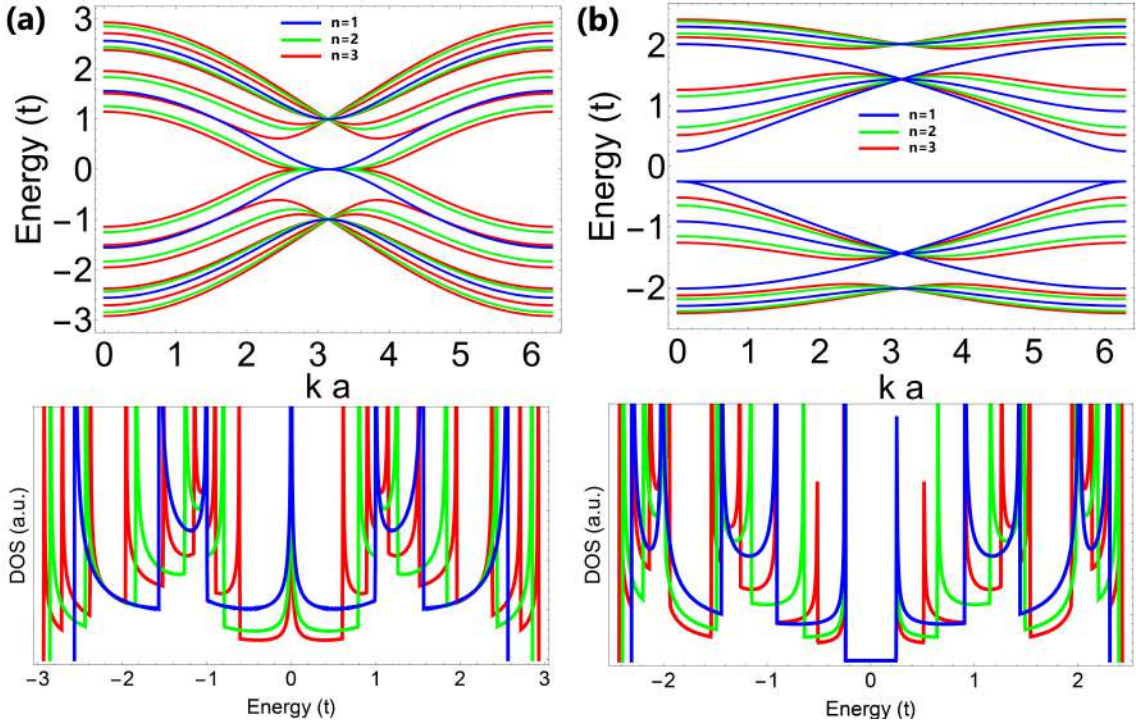
Figure 1.3: Band structure and DOS obtained by the smooth histogram from top to bottom (a) $\varepsilon = 0$ (1,2,3)-Z-GNR (b) $\varepsilon = \pm 0.25t$ (1,2,3)-Z-KHNR.

Usually, energy bands with no dispersion in momentum space, also called as flat bands, are related to isolated sites with no connections between the neighbors. Flat bands in general have many physical interpretations [10, 63]. From the electronic perspective, in such regions, the effective mass of the particle is almost infinite, giving origin to a fully localized state. Consequently, a dispersionless

state surges and the hopping term is effectively turned off. In a Kagomé lattice, the flat bands are characterized by a destructive interference between the electronic wave functions of the moving electrons in the lattice [63]. When this occurs, Bloch orbitals becomes localized at specific sites of the lattice.

With the help of the eigenvalues $E(k)$, obtained from the secular equation 1.1, we can count the number of states per energy and construct an energy smooth histogram, from which it is possible to obtain the electronic total density of states (DOS). Results for the density of states of both systems, kagomé honeycomb and graphene nanoribbons, for N=1, 2, and 3, are shown in the the bottom part of Fig. 1.3. The electronic localization difference between $E = -0.25t$ and $E = 0.25t$ can be evidenced in the respective peak heights of the DOS. As a general DOS feature of both nanoribbon systems is the set of Van Hove singularities, typical of quasi-1D systems. Further techniques for calculating the electronic DOS are discussed in the next section based on the Green function formalism.

1.2 Time-Independent Green's Function

We can use the idea that Schrodinger's equation is to non-relativistic quantum mechanics as Newton's second law is to classical mechanics [64]. However, instead of governing the motion of a particle, as is the case of the second law, the Schrodinger equation governs the dynamics of a wavefunction $\Psi(\vec{r}, t)$. In this context, we are interested in obtaining the Ψ functions of the electrons confined in the crystals, and for that, we can make use of the Green's functions. In general, the time-independent Green functions $G(\vec{r})$ can be seen as solutions of non-homogeneous linear differential equations, which describe systems subject to external perturbations [65]. Let's consider

$$\mathcal{L}\psi(x) = f(x), \tag{1.16}$$

where $\psi(x)$ and $f(x)$ are known and unknown functions, respectively, and $\mathcal{L}$ is a linear operator. The condition for Green's function to satisfy Eq. 1.16 is defined by,

$$\mathcal{L}G(x,x') = \delta(x-x') \Leftrightarrow \int dx' \mathcal{L}G(x,x')f(x') = \int dx'\delta(x-x')f(x')$$

where we use the linearity of $\mathcal{L}$ and Dirac delta's filtering property. Comparing this expression with Eq. 1.16, we determine $\psi(x)$ through

$$\psi(x) = \int dx' G(x,x')f(x'). \tag{1.17}$$

Applying now to the time-independent Schrödinger equation

$$\mathcal{H}(\vec{r})\psi(\vec{r}) = E\psi(\vec{r}), \tag{1.18}$$

we can see that the Green's function that satisfies this expression will be

$$[E - \mathcal{H}(\vec{r})]G(E;\vec{r},\vec{r}\,') = \delta(\vec{r}-\vec{r}\,'). \tag{1.19}$$

$$\rightarrow G(E;\vec{r},\vec{r}\,') = \frac{\langle\vec{r}|\vec{r}\,'\rangle}{E - \mathcal{H}(\vec{r})}, \tag{1.20}$$

where we have used the Dirac notation $\delta(\vec{r}-\vec{r}\,') = \langle\vec{r}|\vec{r}\,'\rangle$.

Using the completeness relation $\sum_n |n\rangle\langle n| = 1$ for the Green's function 1.20 on the basis of the Bloch functions $|\phi_k\rangle$ in which the Hamiltonian $\mathcal{H}|\phi_k\rangle = \varepsilon_k |\phi_k\rangle$ is diagonal, we have

$$G(E;\vec{r},\vec{r}\,') = \sum_k \frac{\langle\vec{r}|\phi_k\rangle\langle\phi_k|\vec{r}\,'\rangle}{E - \mathcal{H}} = \sum_k \frac{|\langle\vec{r}|\phi_k\rangle|^2}{E - \varepsilon_k}. \tag{1.21}$$

This equation admits solutions only if $E \neq \varepsilon_k$. As $\mathcal{H}$ is Hermitian, its eigenvalues are real and, therefore, to satisfy the existence condition of the Green's function, it is necessary to add a small imaginary part in the energy E. Thus, to ensure the convergence of the solution, we define $E = \omega \pm i\eta$, where ω and η are the real and imaginary parts of the energy, respectively, in the limit

$\eta \to 0$. The Green's function is then a complex function, given by

$$G(\omega \pm i\eta; \vec{r}, \vec{r}\,') = \sum_k \frac{|\langle \vec{r} | \phi_k \rangle|^2}{\omega - \varepsilon_k \pm i\eta} \, , \tag{1.22}$$

and defined as retarded (G^r) and advanced (G^a) Green functions

$$\mathbf{G}^{r,a} := \lim_{\eta \to 0} G(\omega \pm i\eta; \vec{r}, \vec{r}\,') \, . \tag{1.23}$$

Using the Cauchy identity

$$\lim_{\eta \to 0} \frac{1}{x \pm i\eta} = P\Big(\frac{1}{x}\Big) \mp i\pi \delta(x),$$

in Eq. 1.22, with $x = \omega - \varepsilon_k$, then

$$\mathbf{G}^{r,a} = P\left(\sum_k \frac{|\langle \vec{r} | \phi_k \rangle|^2}{\omega - \varepsilon_k} \right) \mp i\pi \sum_k |\langle \vec{r} | \phi_k \rangle|^2 \delta(\omega - \varepsilon_k) \, . \tag{1.24}$$

Taking the imaginary part of $\mathbf{G}^{r,a}$, we get,

$$\mp \frac{1}{\pi} Im\Big[\mathbf{G}^{r,a}\Big] = \sum_k |\langle \vec{r} | \phi_k \rangle|^2 \delta(\omega - \varepsilon_k) \, . \tag{1.25}$$

We observe that this expression is related to the probability density of finding the particle with energy ε_k. We can now define the density of states (DOS) with the Trace of the Green's function [65],

$$\rho(\omega) = \mp \frac{1}{\pi} Im\Big[Tr\Big(\mathbf{G}^{r,a}\Big)\Big]. \tag{1.26}$$

Generally, we calculate the DOS involving the delayed Green's function, that is, using the negative sign of $\rho(\omega)$. With this expression, we obtain the total probability occupation of the states as a function of the energies of the studied system.

Another important physical quantity concerning the electron probability distribution is the Local Density of States (LDOS), where in the Green's function formalism could be calculated taking imaginary part of $\mathbf{G}^r(E)[[i, i]]$ for a given energy E at each i-th site. The LDOS gives the

20

spatial information among the electronic charge distribution and the lattice position. In order to obtain the Green functions we use a recursive method for computing the $\mathbf{G}^r$ function, discussed in Appendix. C. The Green's function importance in the nanoscopic transport will be emphasized in the following section.

1.3   Transport in Nanoscale

The macroscopic electrical transport of metals is well described by Ohm's law, which states that the electric current is proportional to the applied voltage. This proportionality constant is the conductance G (inverse of resistance), expressed by the quotient of the cross-sectional area S and the length of the system,

$$G = \sigma \frac{S}{L} \; , \tag{1.27}$$

where σ is the conductivity (inverse of the resistivity), which varies according to the material. Due to the wave characteristics of electrons, in a metal, their wavelength reaches nanoscopic scales. To understand electrical conduction at a fundamental level, it is necessary that the material studied be of the order of the Fermi wavelength λ_F of electronic states, which is the De Broglie wavelength of electrons near the level of Fermi.
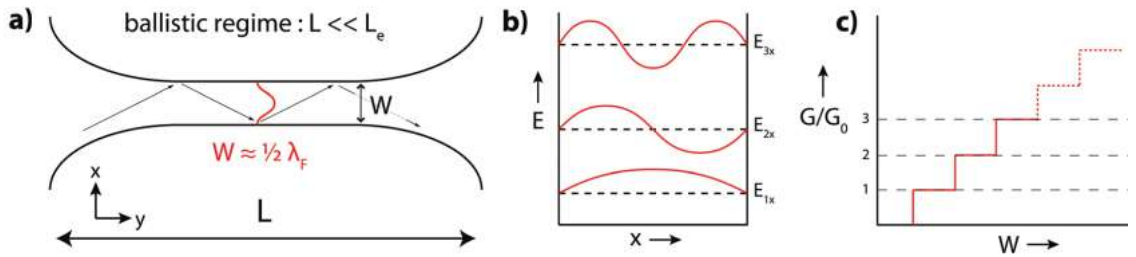
Figure 1.4: (a) Representation of the electron in a ballistic conducting piece. The arrows represent a classic movement of the electron, but in reality at this scale its movement is undulating. When bouncing off the sides along the x-direction of the conductor, the behavior is similar to the problem of the electron confined in a box. (b) The confinement of the electron gives rise to an infinite number of quantized states. The index **n** indicates the number of "half" electron wavelengths (1/2 times the Fermi wavelength λ_F) that can fit in W. (c) Each state **n** contributes **n** quanta for the conductance. [66]

21

An important parameter to determine the transport regime is the mean free path ($\mathscr{L}$), which is the distance traveled by a particle before it is scattered. In the case of a two-dimensional system, as illustrated in Fig. 1.4, it makes no sense to use the parameter S. Instead we denote the width of the conductor by W and L its length. Thus, if $\mathscr{L} < (W, L)$ the transport is said to be diffusive and if $\mathscr{L} > (W, L)$ the transport is ballistic. Based on Eq. 1.27, if the conductor length L is reduced, the conduction would drastically increase infinitely. However, as experimentally reported [67], the conduction is quantized in multiples of $G_0 = 2\frac{e^2}{\hbar} \approx (12.9 \ k\Omega)^{-1}$, which is a finite value. This happens because in a real experiment, the contacts made to measure the electronic flow have a finite resistance, and for that reason in the limit where $\mathscr{L} \gg L$ the electronic conductance will also have a finite value. To calculate such conductance values, we can resort to the Landauer formalism discussed in the section, writing the conductance in terms of electronic transmission probabilities.

1.3.1   Landauer Approach

In the Laudauer formalism, the electronic conduction is associated with the transmission in the ballistic regime through the scattering region, expressed in terms of the probability an electron has to be transmitted through the system [68]. Fig. 1.5, illustrates the one-dimensional transport, in which the contact with the conductor (or scattering region) is made by the left and right leads (or terminals).
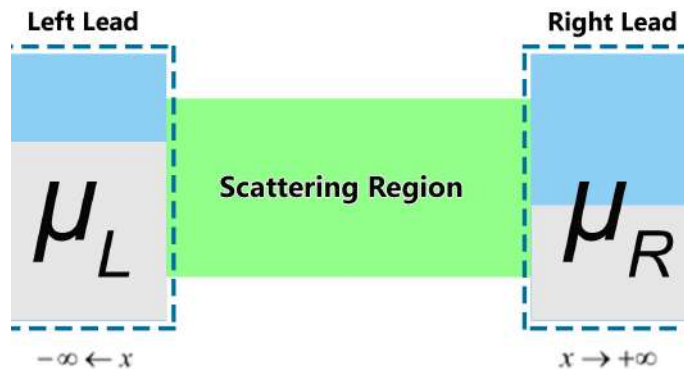
Figure 1.5: Landauer approach involving two terminals represented by the left and right leads with the respective surface Green function calculated in the semi-infinite scheme. The central Green function is calculated over the scattering region on the finite central part.

The contacts are considered as thermal resevoirs. In equilibrium, the chemical potential leads are equal ($\mu_L = \mu_R$). When a gate voltage (V) is established by $V = \frac{\mu_L - \mu_R}{e}$, the chemical potentials in the left and right leads are, respectively, $\mu_L = \mu + eV$ and $\mu_R = \mu$, where e is the electronic charge. We assume that both terminals are filled with electrons following the Fermi-Dirac distribution

$$f_L(E) = f(E, \mu + eV, T) = \frac{1}{e^{\frac{E - \mu + eV}{KT}} + 1}$$

$$f_R(E) = f(E, \mu, T) = \frac{1}{e^{\frac{E - \mu}{KT}} + 1}$$

where K is the Boltzmann constant, E is the electronic energy and T is the temperature.

An electron going from the left/right to the right/left leads has a transmission probability related to the transmissions coefficient $\mathscr{T}(E) = \mathscr{T}_L(E) - \mathscr{T}_R(E)$. The electronic current can be obtained by summing all available energies, the product between the transmission probability and the Fermi-Dirac distribution difference for each lead, as follows [69]

$$I = I_L - I_R = \frac{2e}{h} \int_{-\infty}^{+\infty} \mathscr{T}(E) \left[f_L(E) - f_R(E) \right] dE \ . \tag{1.28}$$

By taking the limit $eV \ll 0$, i.e., considering that the gate voltage between the terminals is sufficiently small in such a way that $\Delta \mu = \mu_L - \mu_R \approx 0$. With this, the Fermi-Dirac distribution becomes,

$$f(E, \mu = \mu_{L,R}, T) = f_{L,R}(E) \approx f(E) - \frac{\partial f(E)}{\partial E}(\mu - \mu_{L,R}) \tag{1.29}$$

where the following identity was used

$$\frac{\partial f(E, \mu, T)}{\partial \mu} = -\frac{\partial f(E, \mu, T)}{\partial E}.$$

Thus,

$$f_L(E) - f_R(E) = \frac{\partial f(E)}{\partial E} \Delta \mu. \tag{1.30}$$

Therefore, using $\Delta \mu = eV$, the Eq. 1.28 could be writing as

$$I = \frac{2e^2 V}{h} \int_{-\infty}^{+\infty} \mathscr{T}(E) \frac{\partial f(E, \mu, T)}{\partial E} dE. \tag{1.31}$$

23

Notice that for low temperatures, the $\partial f(E, \mu, T)/\partial E$ is numerically near from a Dirac's delta around the chemical potential. In this case, using the integral delta properties with T→0K, the electronic distribution is exactly a delta function. Thus, the Eq. 1.31 becomes,

$$I = \frac{2e^2 V}{h} \mathscr{T}(E).$$ (1.32)

Finally, as we have already discussed previously, the mesoscopic conductance is calculated as $G = \frac{I}{V}$. For this reason, in the Landauer formalism, the conductance is expressed as

$$G = \frac{2e^2}{h} \mathscr{T}(E).$$ (1.33)

In this formalism, the next step is to obtain the transmission coefficient $\mathscr{T}(E)$ using the **Decimation** method with the Green's function formalism through the expression [69],

$$\mathscr{T}(E) = Tr(\Gamma_L \mathbf{G}_c^r \Gamma_R \mathbf{G}_c^a).$$ (1.34)

The **Decimation** process details are explored in the Appendix. C. Therefore, here, we want to unravel the meaning of each term from Eq. 1.34 and understand the two terminals model developed by Landauer. As depicted in the beginning of this Section, the system configuration is followed by two leads around the scattering region. The leads are composed by the semi-infinite lattice obtained in the decimation process (see Appendix. C).

To understand Equation 1.34 we need first to define the Green's function of the central part (scattering region), expressed by

$$\mathbf{G}_c^r(E) = [E - H_c - \Sigma_L^r(E) - \Sigma_R^r(E)]^{-1} \, ,$$ (1.35)

where H_c is the Hamiltonian of the central part, and $\Sigma_{L,R}^{r,a}(E)$ are the self-energies for retarded/advanced Green's function of the left and right leads, respectively, expressed as

$$\Sigma_{L,R}^{r,a}(E) = U_{L,R}^\dagger \mathbf{G}_{L,R}^{r,a} U_{L,R} \, ,$$ (1.36)

in which, $\mathbf{U}_{L,R}$ are the hopping matrices that connect the leads with the central part. Note that

$\Sigma^a = (\Sigma^r)^\dagger$ and also that $\mathbf{G}^a_{L,R} = (\mathbf{G}^r_{L,R})^\dagger$. Finally, the coupling matrices expression is then obtained by

$$\Gamma^{L,R}(E) = i\left[\Sigma^r_{L,R}(E) - \Sigma^a_{L,R}(E)\right]. \tag{1.37}$$

In the following section we address the Tersoff-Hamann model for the STM tip and discuss how it is connected with the Local Density of States (LDOS) obtained with the Green's function formalism together with the Landauer approach.

1.4 STM Theory: A Brief look into Tersoff-Hamann model

The Scanning Tunneling Microscope (STM) is an experimental apparatus discovered by G.Binnig and H.Rohrer in March of 1981 [70]. Until now, several progress were made concerning to the technological aspects involved, from manufacturing up to measurements itself, as discussed in the Introduction. To perform the measurements, a small metal tip is kept near enough from the surface of the material and the high (d) between then is adjusted to make the electron tunneling approximately constant, as illustrated in Fig. 1.6. A gate voltage is created to promote a tunneling current measured and processed by the control center, giving, as a result, a surface map of the system as depicted in Fig. 1.6(a). Usually, the STM tip, is composed by cluster of atoms [71], or even, more complex structures like pyramids [31], although in the Tersoff-Hamann model, the tip was considered as a spherically potential well, near from the single s-orbital with radius R, as depicted in Fig. 1.6(b).

The calculations developed originally by J.Tersoff & D.R.Hamann in 1985, used a transfer matrix to compute the system information, and then connect it with the net current [72]. On the present case we derive the tunneling current (I) using the electronic transmission probability between the tip and sample[4] within first-order perturbation theory, following Hui *et al* [73], and then discuss its

---

[4]Experimentally the cluster of atoms present in the tip provides the inverse process, i.e. the net current is measured from the tip to the sample.
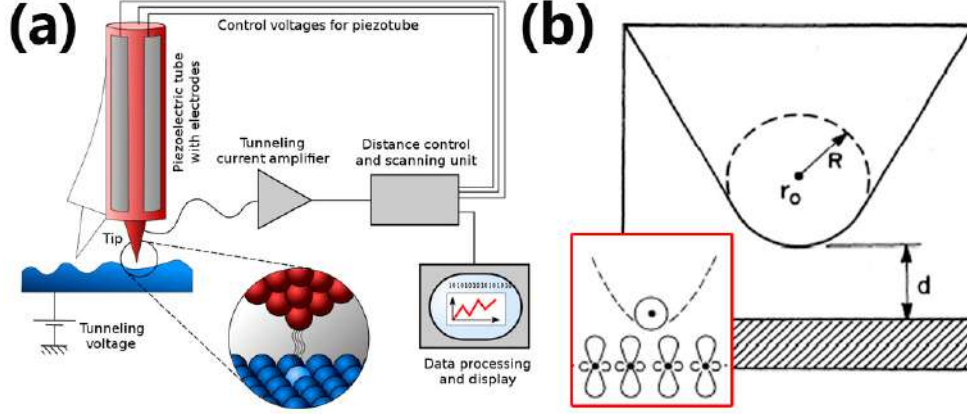
Figure 1.6: a) STM apparatus b) Tersoff-Hamann model for the STM tip [72] with inset showing the s-wave model for the tip interacting with the p_z orbitals of the sample as an example.

connection within the Local Density of States (LDOS). Starting with the one-electron Schrodinger equation for the tip and a similar one for the sample

$$\left[-\frac{h^2}{2m}\nabla^2 + U_t(\vec{r}) \right] \phi_{n\vec{k}_t}(\vec{r}) = E_n(\vec{k}_t)\phi_{n\vec{k}_t}(\vec{r}) \tag{1.38}$$

where $\phi_{n\vec{k}_t}(\vec{r})$ and $E_n(\vec{k}_t)$ are the wave function and the eigenvalue with band index n and wave vector $\vec{k}$, respectively, and U_t is an effective local potential. The Hamiltonian H of the system composed by an electron moving through the sample (s) and the tip (t), is given by

$$H = -\frac{h^2}{2m}\nabla^2 + U_s + U_t + U_{s,t} \tag{1.39}$$

where U_s and U_t are the sample and tip potentials, respectively, and $U_{s,t}$ is the sample-tip interaction potential. Applying the time-dependent perturbation theory, the initial electronic state is localized on $\phi_{n\vec{k}_t}$ with time-dependent amplitude $A_{\vec{k}_t}$. The $\vec{k}_t$ denotes the wave vector of the tip states when a voltage bias is established. We define $\mathcal{P}_{t\to s}$ as the steady-state transition rate of the electron from, $\phi_{n\vec{k}_t}$ on the tip, to $\phi_{n\vec{k}_s}$ in the sample. For simplicity, only a single-band calculations are considered, and also a quasi-unidirectional electron movement between the sample and the tip. In that sense we have $\phi_{n\vec{k}_i} = \phi_{k_i}$ and $E_n(k_i) = E_i$ where $i = s$ or t. Taking into account the transition $\mathcal{P}_{t\to s}$ between the tip and the sample, the time-dependent wave function $\Psi_k(\vec{r}, t)$ will be a combination among the sample and tip states as follows

26

$$\Psi_k(\vec{r}, t) = A_{k_t}(t)\phi_{k_t}(\vec{r})e^{-iE_t t} + \int dk_s A_{k_s}(t)\phi_{k_s}(\vec{r})e^{-iE_s t}. \tag{1.40}$$

Within the perturbation theory the amplitude coefficients in first order are $A_{k_t}(t) \approx 1$ and $A_{k_s}(t) \approx 0$. The transition probability $\mathcal{P}_{t \to s}$ can be calculated taking the $lim_{t \to \infty} |A_{k_s}(t)|^2/t$, yielding to [73]

$$\mathcal{P}_{t \to s} \approx 2\pi |H(k_s, k_t)|^2 \delta(E_s - E_t) , \tag{1.41}$$

where $H(k_s, k_t)$ are the matrix elements $\langle \phi_{k_s} | H | \phi_{k_t} \rangle$. The transition probability can be written in terms of the fermi level or the chemical potentials of the systems, μ_s and μ_t, by $\epsilon_s = E_s - \mu_s$ and $\epsilon_t = E_t - \mu_t$. We have then $\mu_s - \mu_t = eV$, with V being the gate voltage applied between the sample and the tip. Finally, the electronic current is obtained by multiplying the Eq. 1.41 with the probability $f(\epsilon_t)$, that the tip level is occupied, and by $[1 - f(\epsilon_s)]$, being the probability that the sample level s is unoccupied. Both of them integrated over all k_s and k_t for each system. The net current is calculated doing the current difference between each transition possibility,

$$\begin{aligned}
I &= I_{t \to s} - I_{s \to t} \\
&= 2\pi e \int \int dk_s dk_t |H(k_s, k_t)|^2 \\
&\quad \Big(f(\epsilon_t)[1 - f(\epsilon_s)] - f(\epsilon_s)[1 - f(\epsilon_t)] \Big) \delta(\epsilon_s - \epsilon_t + eV) \\
&= 2\pi e \int \int dk_s dk_t |H(k_s, k_t)|^2 \Big[f(\epsilon_t) - f(\epsilon_s) \Big] \delta(\epsilon_s - \epsilon_t + eV) ,
\end{aligned} \tag{1.42}$$

where we have used $\delta(E_s - E_f) = \delta(\epsilon_s - \epsilon_t + eV)$, with $f(\epsilon)$ being the Fermi-Dirac distribution. In the limit where the applied voltage and the temperature are sufficiently low, the net current becomes

$$I = 2\pi e^2 V \int \int dk_s dk_t |H(k_s, k_t)|^2 \delta(\epsilon_s)\delta(\epsilon_t) . \tag{1.43}$$

In the multiband case, the band indexes n and m should be take into account for the sample and tip, respectively. The calculations made so far could be preserved, adapting only the matrix elements of $H(k_s, k_t)$ to $H_{n,m}(k_s, k_t)$. In fact, the calculations made by Tersoff-Hamann using the transfer matrix $\mathcal{M}_{n,m}$ reach at the same result as developed here with the correct connections between the

two models [72, 73]. Considering only simple single orbitals for the tip function ϕ_t the net current can be written as

$$
\begin{aligned}
I &\propto e^2 V \sum_n \int dk_s |\langle \phi_{nk_s} | H | \phi_t \rangle|^2 \delta(\epsilon_s) \\
&\propto \times \sum_n \int dk_s |\phi_{nk_s}|^2 \delta(\epsilon_s) \\
&\propto \times LDOS
\end{aligned}
\tag{1.44}
$$

where only the n-bands of the sample were considered. Because the function ϕ_t is concentrated at the tip position $\vec{r}_0$, we have assumed that the matrix elements $\langle \phi_{nk_s} | H | \phi_t \rangle$ are proportional to the overlap integral $\langle \phi_{nk_s} | \phi_t \rangle$. As a consequence of this, the term $\langle \phi_{nk_s} | \phi_t \rangle$ becomes proportional to $\langle \phi_{nk_s} | \vec{r}_0 \rangle = \phi_{nk_s}(\vec{r}_0)$ leading to the LDOS definition,

$$
LDOS(\vec{R}_0, E) = \sum_n |\Phi_n(\vec{R}_0)|^2 \delta(E - E_n)
\tag{1.45}
$$

where $\vec{R}_0$ here denotes the lattice positions and $\Phi(\vec{R}_0)$ is the corresponding electronic wave function of the nth state acting here as weights to the electronic distribution. It is important to stress that this equivalence between the current measured in the STM and the LDOS works well for s-wave tips with low Miller index metal surfaces like Au(111), Cu(100), and others [71]. We will see later that, in fact this theoretical model fits very well with experimental observations of synthesized fractal molecular chains.

Chapter 2

Electronic Properties of Standard Carbon Systems

Carbon materials are very versatile due to the several chemical linkage possibilities. Forming single, double and triple bonds, the carbon interactions gives a large number of compounds that could be created. The calculations presented in this work are related essentially with carbon-atom lattices, and then, the principal atomic orbital responsible for the transport is the p_z. The electron configuration in carbon is given by $1s^2 2s^2 2p^2$. The first core is screened while the others energies levels are composed by two hybridized perpendicular states $\sigma_{x,y}$ and π_z, formed by p_x, p_y, s and p_z orbitals, each one with one electron (four in total). In the orthogonal TB approximation there is no overlap between the orbitals and the energy bands close to the Fermi energy are p_z-orbital contributions. The p_z are then the most important orbitals for the electronic transport, with the carriers moving between the sites using the hopping energies. The TB energy parameters can be obtained by first principle calculations within other computation methods [74], but one of the strengths of the TB model is the possibility of obtaining the electronic properties in function of t.

Graphene systems and its allotropes (graphyne and kagomé lattices) can be prepared in several ways, such as flakes, wires, nanotubes, monolayers and bilayers [75]. The monolayers are bidimensional system (2D), with infinite symmetry in both x-y directions, also called as bulk in some cases. A quasi-one dimension graphene lattice is the graphene nanoribbon, that depending on the

edge-geometry are subdivided as chiral or achiral ribbons. In the latter group we have zigzag and armchair nanoribbons. The nanoribbons can be obtained by cutting the infinite system along one specific axis and present infinite periodicity along that direction while exhibiting discrete states in the confining direction. In the following we discuss both 2D and quasi-unidimensional examples of some all-carbon systems disposed in the called standard geometries.

2.1 Monolayer

Taking a single slice of graphite makes possible for the first time the study the electronic properties of monolayered carbon systems [1]. Here we focus on the investigation of such properties in graphene, graphyne and kagomé honeycomb features. The most general aspects of graphene nanoribbons (GNRs) and 2D-graphene features were already explored analytically and numerically by Wakabayashi *et al* [2] and other authors [5]. For that reason, the electronic properties of graphene will be compared with the electronic results obtained for other hexagonal systems.

	α-Graphyne	Kagomé H.	Graphene
t_1	2.85/2.40 eV	t	2.80 eV
t_2	7.50/3.40 eV	——	——
a_{sp^2}	1.396 Å	a_{KH}	1.4 Å
a_{sp}	1.230 Å	——	——
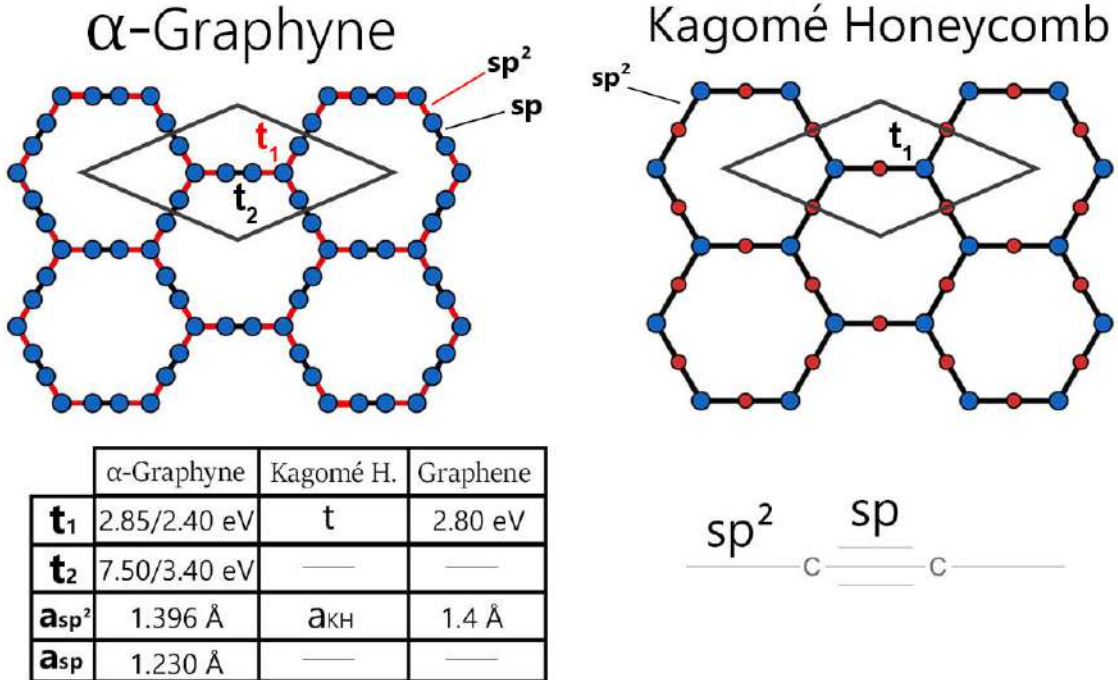
Figure 2.1: Top: 2D α-graphyne and kagomé honeycomb lattices. Bottom: Tables of the hopping and lattice parameters and bond scheme of the α-graphyne lattice.

In Fig.2.1 we present schematically the α-graphyne and the kagomé honeycomb lattices. Dif-

ferently from the graphene and Kagomé lattices the graphyne exhibits sp-like orbitals, forming acetylenic bonds in addition to the usual sp^2. The acetylenic and simple carbon bonds in graphyne are represented by the lattice parameters a_{sp} and a_{sp^2}, respectively. As hopping energies are inversely proportional to the corresponding atomic distance, and as $a_{sp} < a_{sp^2}$, we expect to have $t_2 > t_1$, where t2 and t1 are represented in the Fig. 2.1 with black and red lines. Of course, chemical aspects of linkages are very important for this result. The other hexagonal lattice shown, the Kagomé Honeycomb, may be described as a decorated graphene lattice. Actually, graphene lattice is recovered by removing the red sites in the unit cell of kagomé honeycomb shown in Fig. 2.1. Both structures have the same hexagonal symmetry, and then we can use the same unit cell, with area $\vec{a}_1 \times \vec{a}_2$ given in terms of the corresponding lattice parameter a and changing the the unit cell basis from 2 atoms for graphene, to 5 and 8 atoms for kagomé and α-graphyne, respectively.
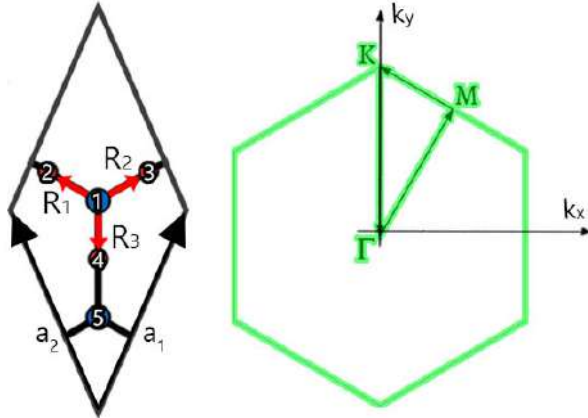
Figure 2.2: Left: Unit cell representation of the 2D-kagomé honeycomb. Right: Reciprocal space of a honeycomb lattice with high symmetry points highlighted.

In the following we calculate the electronic structure of the kagomé lattice. The unit cell and the corresponding first Brilouin zone are depicted in Fig. 2.2. Numerical calculations were developed with the use of Hamiltonian 1.12, and adopting the hopping parameters t1 and t2 given in reference [11, 76], for the α-graphyne, and t_1 for the graphene lattice [75].

The lattice vectors are defined as

$$\vec{a}_1 = a(\cos 30°, \sin 30°) \quad \vec{a}_2 = a(0, 1).$$

31

The first nearest neighbor are mapped in terms of the position vectors

$$\vec{R}_1 = a(\frac{\sqrt{3}}{6}, 0) \ ,$$
$$\vec{R}_2 = a(-\frac{\sqrt{3}}{12}, \frac{1}{4}) \ ,$$
$$\vec{R}_3 = a(-\frac{\sqrt{3}}{12}, -\frac{1}{4}). \tag{2.1}$$

Using the method described in Sec.1.1.1, the Hamiltonian for kagomé honeycomb is given as

$$H_{KH} = \begin{pmatrix} \varepsilon_1 & tM_1 & tM_2 & tM_3 & 0 \\ tM_1^* & \varepsilon_2 & 0 & 0 & tM_1 \\ tM_2^* & 0 & \varepsilon_3 & 0 & tM_2 \\ tM_3^* & 0 & 0 & \varepsilon_4 & tM_3 \\ 0 & tM_1^* & tM_2^* & tM_3^* & \varepsilon_5 \end{pmatrix} \tag{2.2}$$

where $M_j = \exp\left(i\vec{k}.\vec{R}_j\right)$ (j=1,2,3), M_j^* its complex conjugate, and the potentials $\varepsilon_2 = \varepsilon_3 = \varepsilon_4 = \epsilon_K$ and $\varepsilon_1 = \varepsilon_5 = \epsilon_H$ represent the atomic plurality of the kagomé lattice. Solving the secular equation 1.1 for H_{KH}, we obtain the eigenvalues

$$E_1 = \epsilon_K$$
$$E_2 = \frac{1}{2}\left(\epsilon_H + \epsilon_K - \sqrt{(\epsilon_H - \epsilon_K)^2 + 4t^2(3 - f_{\vec{k}})}\right)$$
$$E_3 = \frac{1}{2}\left(\epsilon_H + \epsilon_K + \sqrt{(\epsilon_H - \epsilon_K)^2 + 4t^2(3 - f_{\vec{k}})}\right)$$
$$E_4 = \frac{1}{2}\left(\epsilon_H + \epsilon_K - \sqrt{(\epsilon_H - \epsilon_K)^2 + 4t^2(3 + f_{\vec{k}})}\right)$$
$$E_5 = \frac{1}{2}\left(\epsilon_H + \epsilon_K + \sqrt{(\epsilon_H - \epsilon_K)^2 + 4t^2(3 + f_{\vec{k}})}\right) \tag{2.3}$$

where $f_{\vec{k}} = \sqrt{4\cos\left(\sqrt{3}ak_x/2\right)\cos(ak_y/2) + 2\cos(ak_y) + 3}$. The first constant eigenvalue E_1 is responsible for the flat band in the dispersion relation. This particular value corresponds to the on-site energies of the atoms at the 2, 3 and 4 positions in the unit cell. The dispersion relation along the high symmetry path is presented in Fig. 2.3, considering two on-site energy configurations. The

flat band at E_1 clearly breaks the electron-hole symmetry of the band structure around the Fermi Level. Moreover, no available energies for electrons in the range $\Delta E = 0.25t$ are found in the case of $\epsilon_K = -\epsilon_H = 0.25t$ [9], revealing a semiconductor characteristic for the Kagomé when $\epsilon_K \neq \epsilon_H$ [see Fig. 2.3(a)]. Otherwise, for $\epsilon_K = \epsilon_H = 0$ [see Fig. 2.3(b)], as discussed for kagomé honeycomb systems, the spatial and time-reversal symmetries are preserved and the gap is closed.
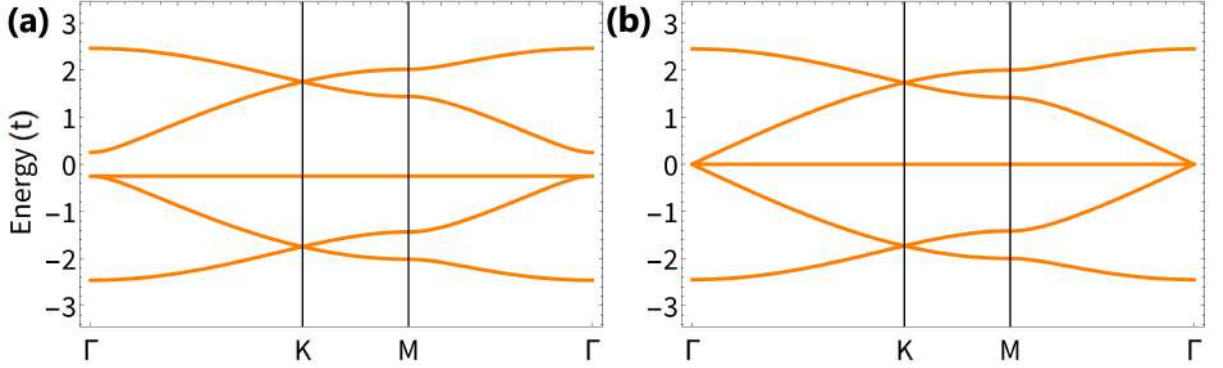
Figure 2.3: Energy dispersion of a kagomé honeycomb in terms of t for (a) $\epsilon_H = 0.25t$, $\epsilon_K = -0.25t$ and (b) $\epsilon_H = \epsilon_K = 0$.

For α-graphyne monolayer, the band structure has symmetric flat bands which are tuned by changing the hopping ratio t_1/t_2, as seen in Fig. 2.4. As previously mentioned, for graphyne lattices described by the TB Hamiltonian we have $t_2 > t_1$ and then a physical result is only observed for $t1/t2 < 1$. For this case the flat bands are pinned at $E = \pm t_2$ and are symmetrical with respect to the Fermi level ($E = 0$), as can be seen in Fig. 2.4(a). For $t_1 > t_2$ the same behavior is observed, as shown in the energy dispersion highlighted in the green square in Fig. 2.4(b), for $t_2 = 0.5t_1$. The morphology of the band structures can be captured in the gap energy given by $\Delta(t)$ as a function of the hopping ratio t_1/t_2. As depicted in Fig. 2.4(c), for ratio values satisfying $\frac{t_1}{t_2} < 1$ a linear behavior is seen with a minimum value of $\Delta(t) = 0$, null gap, for $t_1/t_2 = \sqrt{2/3}$, as shown in the band structure shown within the blue square in Fig. 2.4(c). The $\Delta(t)$ values as a function of the t-ratio gives a picture of the itinerant flat bands. The colors red and orange are used to distinguish between physical and not physical situation in the graphyne, respectively. The evolution of the flat band with the hopping values was previously reported for the square Lieb lattice with similar features [77] and also evidenced for kagomé lattices [78].
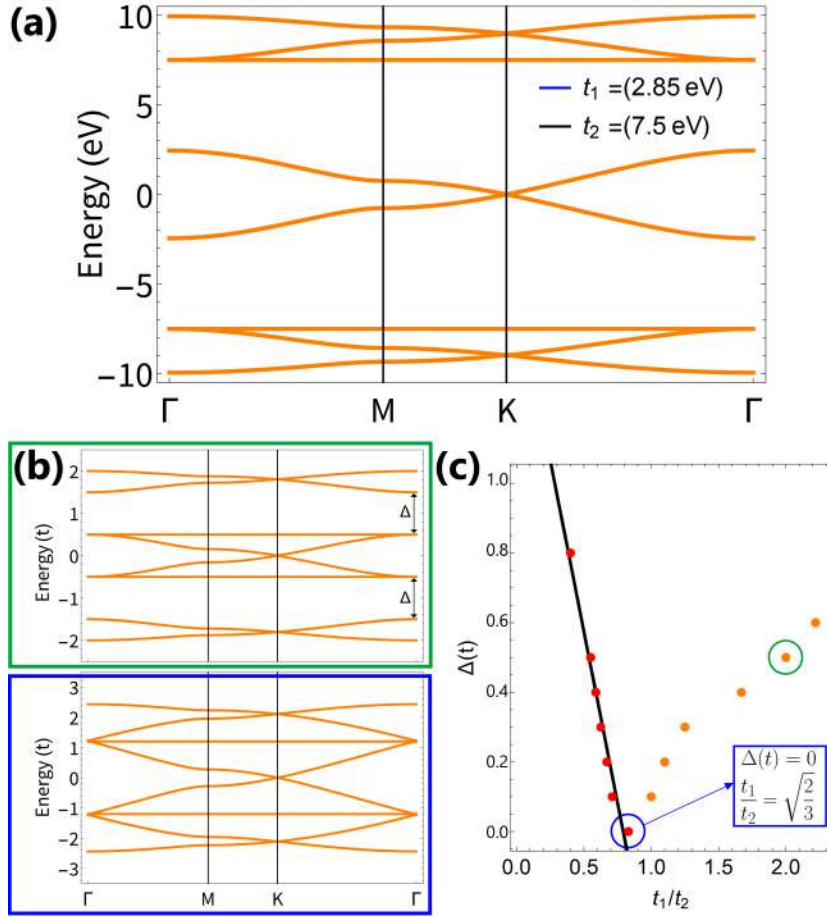
Figure 2.4: Band structure of α-graphyne. (a) for $t_1 = 2.85\ eV$, $t_2 = 7.5\ eV$ (b) Changing the hoppings t_1 and t_2, green and blue highlited bands have t_1/t_2 equal to 2 and $\sqrt{2/3}$, respectively. (c) $\Delta(t)$ as a function of t_1/t_2.

As Dirac cones and flat bands describe opposite electronic properties, they are difficult to coexist, although band engineering could be employed to promote the crossing between Dirac cones and flat bands in graphene and kagomé nanoribbons [79, 80]. In Fig. 2.5 we present a comparison between the DOS of the graphene, graphyne and kagomé lattices, by setting the on-site energies equal to zero and using the hopping parameter equal to the graphene lattice, i.e., $t = 2.85eV$. Next to the Fermi energy the graphene [Fig. 2.5(a)] and α-graphyne [Fig. 2.5(b)] have the same semi-metallic aspect, as zero gap semiconductors, while for the kagomé [Fig. 2.5(c)] the energy gap is closed for $\varepsilon = 0\ eV$ due to a flat state in the zero level.

Lowering the system dimensions, by cutting along orthogonal directions, we get nanoribbon lattices, as depicted in Fig. 2.6(a); the zigzag and armchair are obtained for vertical and horizontal

34
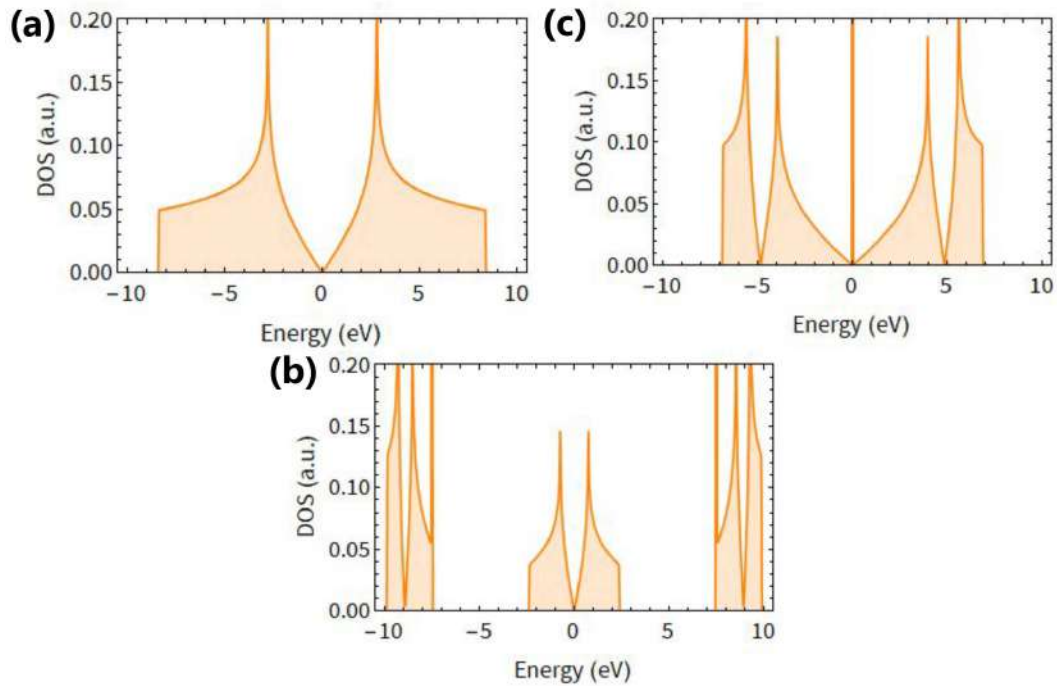
Figure 2.5: Density of states for zero on-site energy values: (a) graphene and (b) α-graphyne, and (c) kagomé honeycomb with t=2.85eV.

cuts, respectively. Because of the graphene and graphyne lattice geometries [see Fig. 2.6(b)], we can construct similar unit cells for both graphene (GNRs) and α-graphyne nanoribbons (GyNRs). The first two unit cells $N = 1$ and $N = 2$ are displayed in the figure.
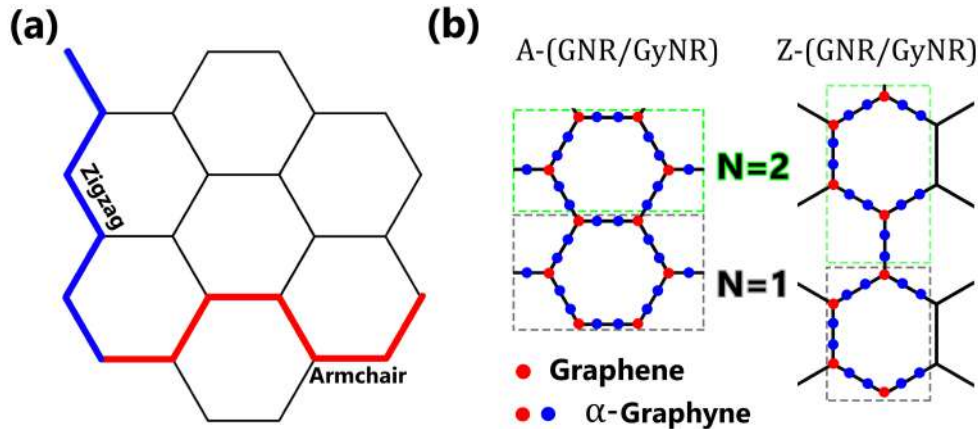
Figure 2.6: Nanorribons scheme illustration (a) Cut direction of both armchair and zigzag, for red and blue lines, respectively, along the hexagonal lattice. (b) Nanorribons unit cells for both A-GNR/GyNR and Z-GNR/GyNR from left to right, respectively.

The effects of the lattice topology on the electronic properties of the system is presented in Fig.

2.7, where a comparison between the hexagonal nanoribbon lattice details of graphene, graphyne, Kagomé and 3-dimer graphyne lattices (all with N=3) and the corresponding band structure is explored. The results are grouped accordingly with the parity symmetry of the unit cells of the lattices. The results indicate a direct relation to that, i.e., if the number of atoms inside the unit cell (2D system) is even, such as in the cases of graphene (4 atoms) and α-graphyne (8 atoms), the properties will be similar for the nanoribbons as shown in Fig. 2.7(a) and (b), respectively; semiconductor families for armchair nanoribbons with N=3 (and metallic states for zigzag - not shown here). These features are also found for α-graphdiyne nanoribbons [18], with 14 atoms in the unit cell.
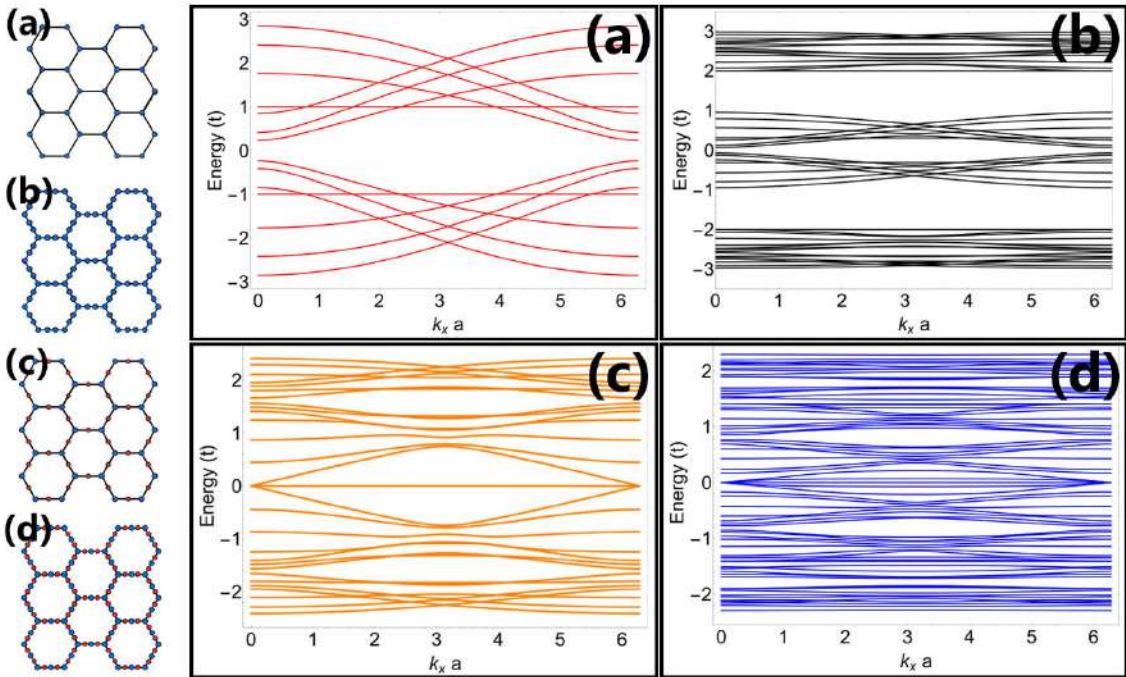
Figure 2.7: N=3 Armchair nanoribbon lattices and corresponding band structures: (a) Graphene, (b) α-Graphyne, (c) Kagomé honeycomb, and (d) Decorated honeycomb for $\epsilon = 0$

Otherwise, if the system unit cell has an odd number of atoms it will behave as a semiconductor independently of the nanoribbon family, as evidenced for kagomé honeycomb with $\epsilon = 0$ (5 atoms in the unit cell), shown in Fig. 2.7(c). This metallic characteristic is also found for a proposed decorated honeycomb lattice, a 3-dimer graphyne lattice presenting odd parity, as depicted in Fig. 2.7(d). For zigzag-edged nanoribbons, both lattices with odd parity are metallic with a well defined flat band at the Fermi level E=0.

A comparison between the energy gaps vs the unit cell index of armchair GNRs and GyNRs can be seen in Fig. 2.8(a) and (b). We notice that the armchair nanoribbons alternate from semiconductor to metallic systems in both lattices; two semiconductor series, 3p and 3p+1, and one metallic 3p+2. The armchair nanoribbon width is given by $a \times N$, with a being the atoms distance inside the lattice of each system and N the nanoribbon cell index. Although not shown here, kagomé honeycomb nanoribbons (KHNRs) have a constant gap undependable from the configuration details or ribbon width, given by the difference between the on-site energies. In the previous case presented in Fig. (c), a null gap was found since the same energy was considered for the red and blue atoms illustrated in the schematic Kagomé lattice in the left pannel. This particular property is also evidenced in the Sierpinski kagomé that will be discussed in the next Chapter.
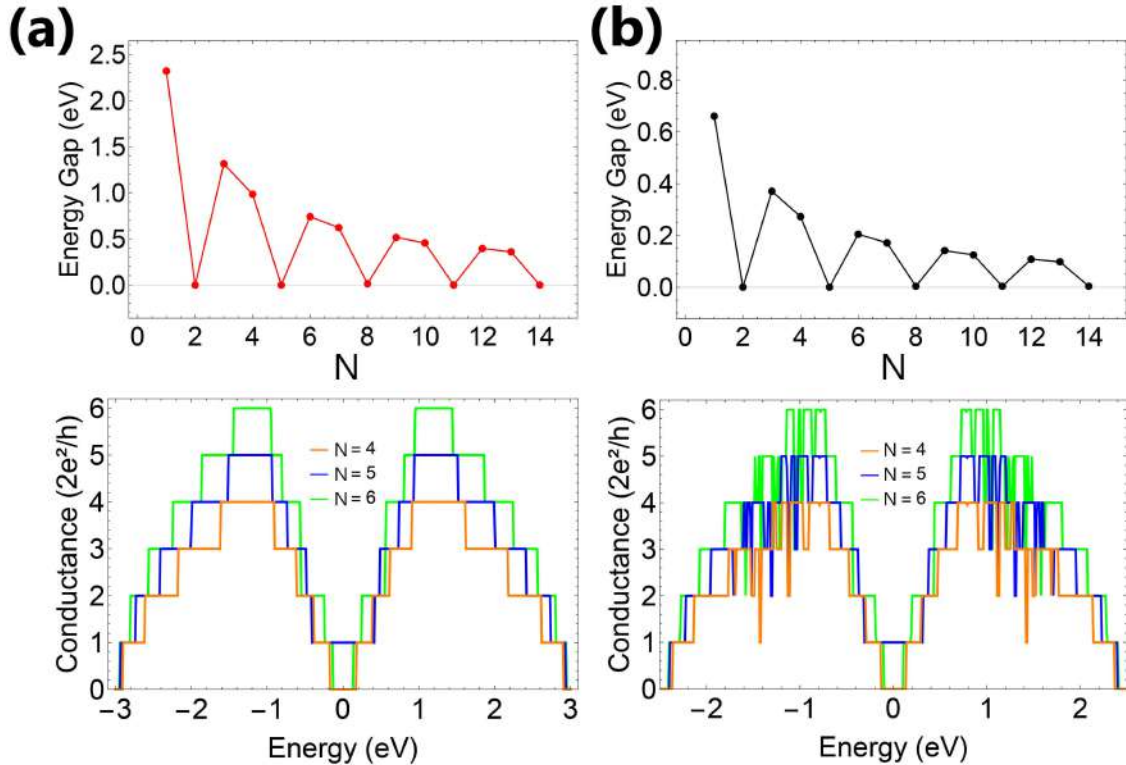
Figure 2.8: Energy gap and conductance for (a) A-GNR [$t = 2.80$ eV] and (b) A-α-GyNRs [$t_1 = 2.85$ eV and $t_2 = 7.50$ eV].

Furthermore, electronic transport aspects were investigated and shown in the bottom of Fig. 2.8. We note that each conductive channel is unveiled by the sequence of plateaus, characteristic

of ballistic transport. The conductance results for A-GNR and A-GyNR exhibit the same sequence of channel number, considering equal unit cells indexes. In the following Section we explore what happens to the electronic properties when the single nanoribbons discussed here are stacked forming bilayered systems, and how the alignment between the layers affect the general physical features.

2.2   Bilayer

In the case of bilayered systems, new configurations can be reached depending on the particular atomic aligning within the unit cell. The number of possible stacking depends on the number of atoms in the unit cell. Moreover, the energetic stability is the most important aspect to systems formation. It is known, for instance, that for graphite the most stable configuration is the Bernal stacking.
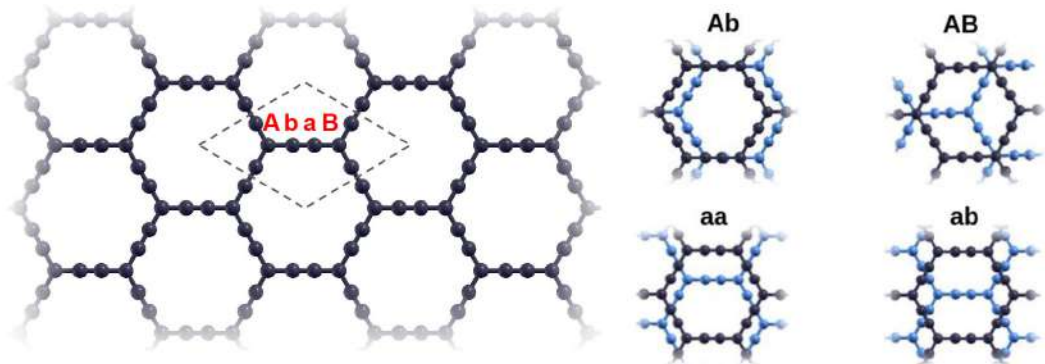
Figure 2.9: Unit cell of 2D α-Gy and the four stacking possibilities *Ab, aa, AB and ab*. Adapted from Ref.[81].

For graphene, as already seen in the Introduction, the total number of alignments are two, being the direct stacking, when two *A* atoms are exactly on top of each other [*AA* stacking], and the Bernal or *AB* stacking, occurring for *A* and *B* atoms directly aligned in the unit cell, respectively. On the other hand, α-graphyne allows more stacking possibilities illustrated in Fig. 2.9, as *Ab, aa, AB* and *ab*. Recent DFT calculations have addressed *Ab* stacking as the most stable with an average distance $d_A = 3.14$ Å between the layers [81, 82]. For this reason, the calculations of the graphyne bilayer nanoribbons are mainly calculated regarding this configuration as will be discussed later.

The Hamiltonian matrix of bilayered systems can be constructed by duplicating the monolayer matrix and including each layer interaction as follows

$$H_{Bi} = \begin{pmatrix} H_{L1} & H_{int} \\ H_{int}^* & H_{L2} \end{pmatrix} \tag{2.4}$$

with H_{L1} and H_{L2} being the hamiltonians of the individual layers and e H_{int} the interaction between them. In the second quantization formalism, the same hamiltonian is expressed as

$$H = \sum_{i,\alpha} \varepsilon_i^\alpha c_i^{\dagger\alpha} c_i^\alpha - \sum_{\substack{\langle ij \rangle \\ \alpha}} t_{ij}^\alpha c_i^{\dagger\alpha} c_j^\alpha - \sum_{\substack{\langle ij \rangle \\ \alpha \neq \beta}} t_{ij}^{\alpha\beta} c_i^{\dagger\alpha} c_j^\beta + h.c. \tag{2.5}$$

with ε_i being the on-site energy for each atom located at site i in the α layer ($\alpha = 1, 2$) and the operator $c_i^{\alpha\dagger}$ (c_i^α) creates (annihilates) an electron on site i and plane α. The second term describes the intralayer couplings ($\alpha = 1$ and 2), t_{ij}^α being the corresponding hopping energies taken as t_1 and t_2 for graphyne and t graphene, depending if the i and j first-neighboring atoms share sp or sp^2 hybridized orbitals, respectively. Interlayer interactions are considered in the last term ($\alpha \neq \beta$) and denoted as $t_{ij}^{\alpha\beta} = t_\perp$. They depend on the stacking configuration between top and bottom layers and on the respective edges.

In particular, for graphene bilayers (BG), in AA and AB stackings, we see a linear crossing and a parabolic pattern at the K points, respectively. In the AB stacking a band gap can be induced by applying an external perpendicular electric field perpendicularly to the layers plane, as theoretically predicted and experimentally verified, [25, 26]. Without the field, as shown in Fig. 2.10(a) and (b), both stackings AA and AB are metallic. In the inset of the band structures it is possible to verify that the linear dispersion band crossing at K point still appears for AA stackings, while for AB the eigenenergies follows a not crossing parabolic shape at K point.

In this Section we are interested in the study of the electronic properties of the graphyne bilayers (BGy). As pointed out in the literature, the graphyne systems are good candidates to thermometric device construction due to its very poor electronic-phonon thermal conductance [83, 84]. As a result,
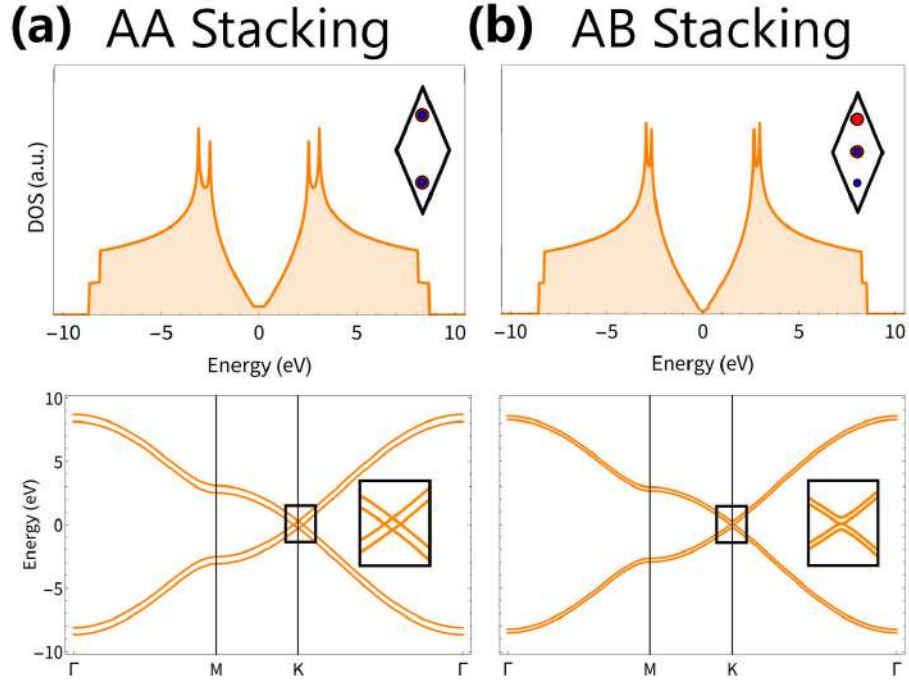
Figure 2.10: 2D bilayered graphene DOS, band structure and unit cell of (a) *AA* and (b) *AB* stackings.

thermoelectric efficiency responses are higher than the verified for graphene [81, 85]. The energy bands for α-graphyne 2D bilayers are also calculated. We notice that the orange and black atoms have distinct positioning depending on the stacking inside the unit cell. For the *Ab* stacking the unit cell has two atoms positioned exactly one above the other, giving origin to a hopping parameter $t_\perp = 0.28$, and also with one almost direct align among the atoms, leading to a mismatch between the first and second layers, represented in the model as $t'_\perp = 0.25$ eV. The energy bands behavior close to the Fermi level are also different for the α-graphyne stackings, in which, for *Ab* stacking [see Fig. 2.11(a)] the energy spectra in the point K are almost parabolic as observed in *AB* stacking for graphene. A very similar result is observed for the *AA* stacking in both graphene and α-graphyne bilayers as can be seen in Fig. 2.11(b).

The band structure comparison between the results in orange for TB and blue for DFT calculations made by Rodrigues et al [81] reveals that the simple model used here, better fits the results for direct stackings, like *AA*. In the case where a mismatch between the atoms of both layer is observed, as in *Ab* stacking, adding second neighbors and including the overlap between the orbitals
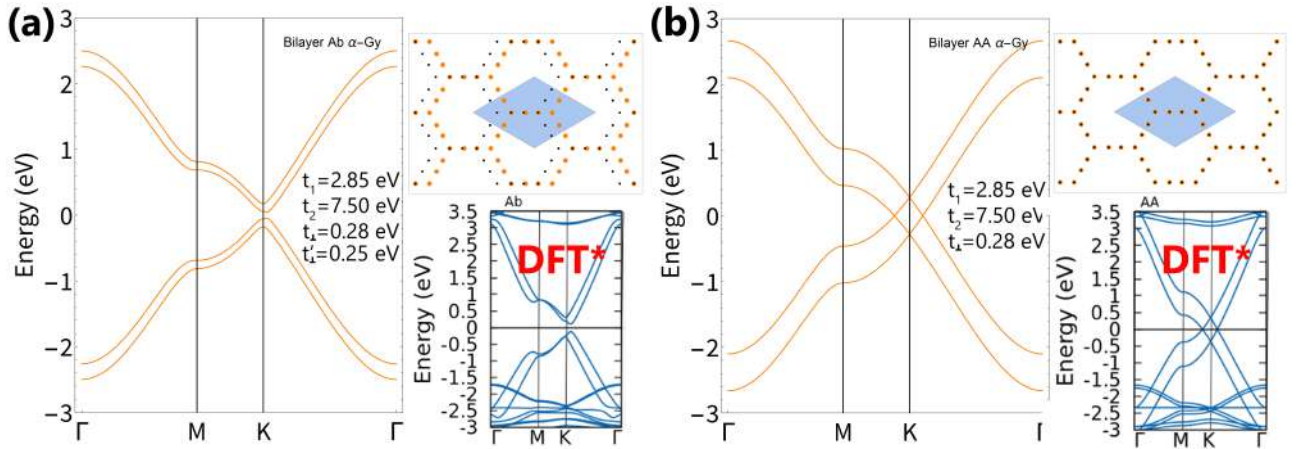
Figure 2.11: In orange our TB results and in blue DFT*[81] band structures of 2D α-Gy (a) *Ab* stacking showing almost parabolic crossing in K (b) *AA* stacking with linear crossing bands in K.

in the TB model could better fit the results obtained in DFT (not shown here).
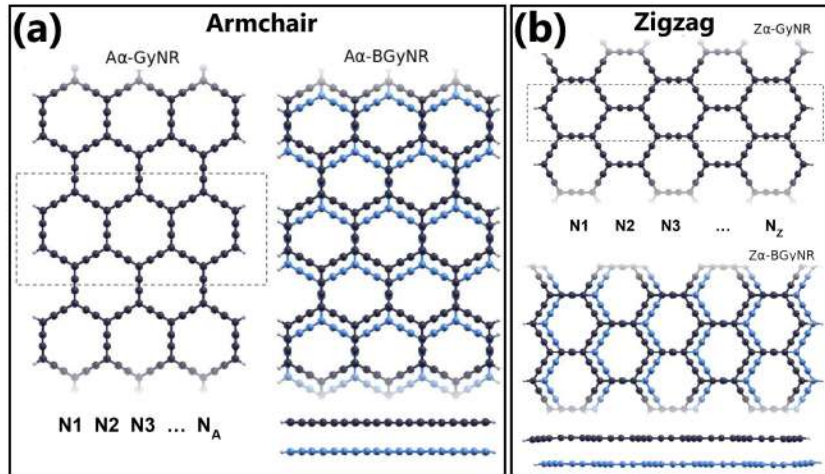
Figure 2.12: α-Gy mono/bilayer nanoribbons scheme for (a) Armchair and (b) Zigzag. Both relaxed results are exhibit in the bottom of the respective nanoribbon type. Adapted from[81].

As well as for monolayers, we can cut the bilayered bidimensional system along two directions and obtain the bilayer nanoribbons (BNRs). An interesting feature is the bending effect observed on the α-graphyne zigzag features after relaxation calculations [81] as evidenced in Fig. 2.12(a) and (b), we notice in the bottom of each figure, an attractive and repulsive action in the armchair and zigzag bilayers, respectively. The same behavior were reported for bilayer graphene nanoribbons

41

[24, 86]. With that, new properties can be explored and studied in these systems. For the zigzag α-graphyne nanoribbon (Zα-BGyNR) we have chosen the hopping energy parameters [11] as $t_1 = 2.85$ eV and $t_2 = 7.50$ eV and the hopping interaction between the layers are considered as $t_\perp = 0.28$ eV and $t'_\perp = 0.25$ eV for AA and Ab stacking, respectively. For the α-graphyne armchair nanoribbons Aα-BGyNR showed in Fig. 2.13, the chosen parameters are as follows: $t_1 = 2.85$ eV, $t_2 = 4.00$ eV, and $t_\perp = 0.37$ eV and $t'_\perp = 0.23$ eV for AA and Ab stacking, respectively. Both parameters were chosen based on the nearest results of TB in comparison with DFT calculations [81].
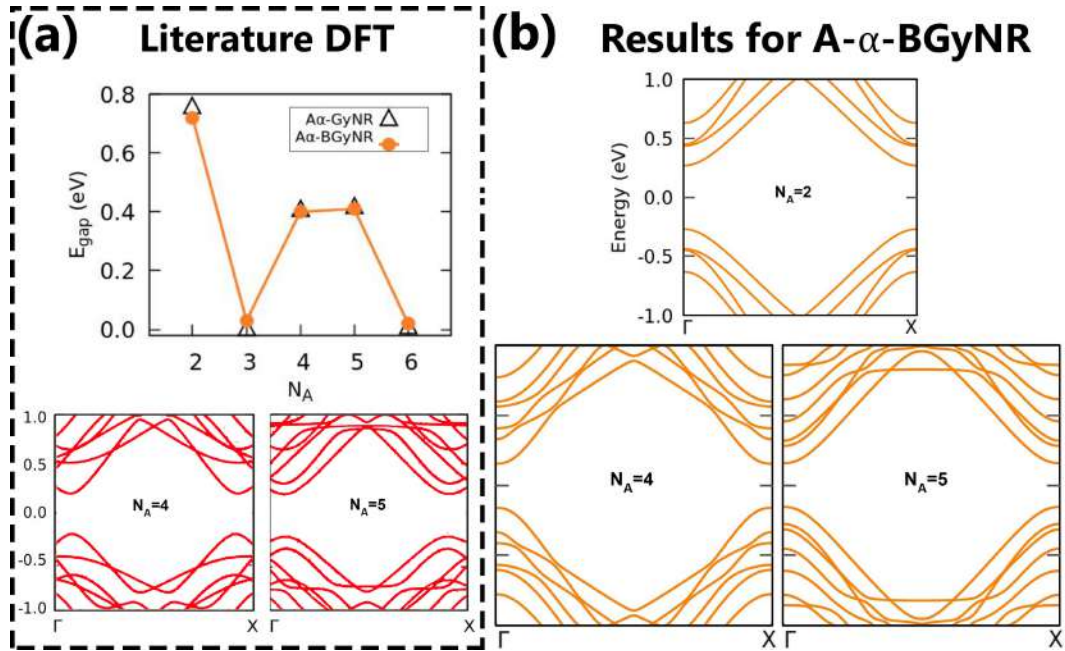
Figure 2.13: DFT and Tight-Binding calculations on Aα-BGyNR for Ab stacking (a) From top to bottom: Gap evolution of armchair monolayer and bilayer nanoribbons and band structures of N_A= 4 and 5 of DFT calculations [81]. (b) Band structures of N_A=2, 4, and 5 preserving the edges symmetry (here ΓX path stands for $k_x \in [0, \pi/a]$).

Just like graphene, the bilayer graphyne armchair families alternate between semiconductor and metallic states, as confirmed by DFT calculations [81] in Fig. 2.13(a). Considering only the semiconductor cases in armchair, we see that the band structures of Aα-BGyNR in Fig. 2.13(b) obtained with a simple first neighbors TB are in good agreement with the ones calculated via DFT [81]. The electronic density of states and the conductance of an N-αA-BGyNR with $N_A = 5$ are presented in Fig. 2.14(a) and (b). The energy gaps confirm the semiconducting nature of

such bilayer nanoribbon. The charge distribution for a particular energy, along the nanostructure, may be visualized by a colour plot of the local density of states (LDOS). The two LDOS color maps displayed at the right part of Fig. 2.14 correspond to the results for the highlighted energies in dashed lines on the electronic conductance [see Fig. 2.14 (a)] and density of states [see Fig. 2.14(b)], E=0.50 eV and 1.1 eV in green and black, respectively. We notice that, for E=0.50 eV the charge density distribution are localized primarily at the more external acetylenic linkages, whereas for E=1.11 eV they are localized in the middle of those linkages on the nanoribbons.
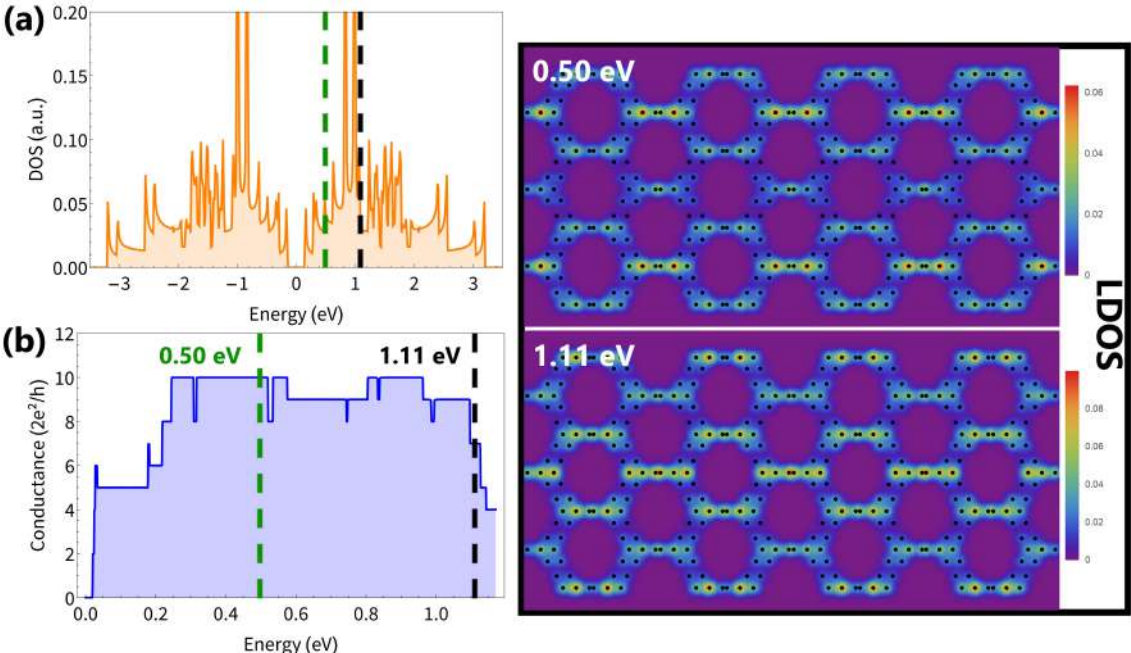
Figure 2.14: (a) Density of States and (b) Electronic Conductance of Ab stacking 5-αA-BGyNR (c) LDOS results with lattice in black dots and energy regions highlighted in DOS and Conductance with green and black dashed lines.

Returning to the graphene systems, it is interesting to compare the band gap evolution of an armchair single nanoribbon layer and the AB stacked bilayer nanoribbon graphene, as shown in Fig. 2.15(a). The results exhibit the same alternating behavior between the energy gap (lower values for bilayer) as the system is grown following the description given in Fig. 2.15(b). As discussed before for both, GNR and GyNR, the pristine zigzag features without disturbance are metallic systems. When atomic relaxation are considered in AB bilayer graphene nanoribbon, an small energy gap is achieved, as predicted by our TB model (blue curves) and DFT calculations reported

in Refs. [24, 86], as shown in Fig. 2.15(c). It is important to stress that, this bending effect could
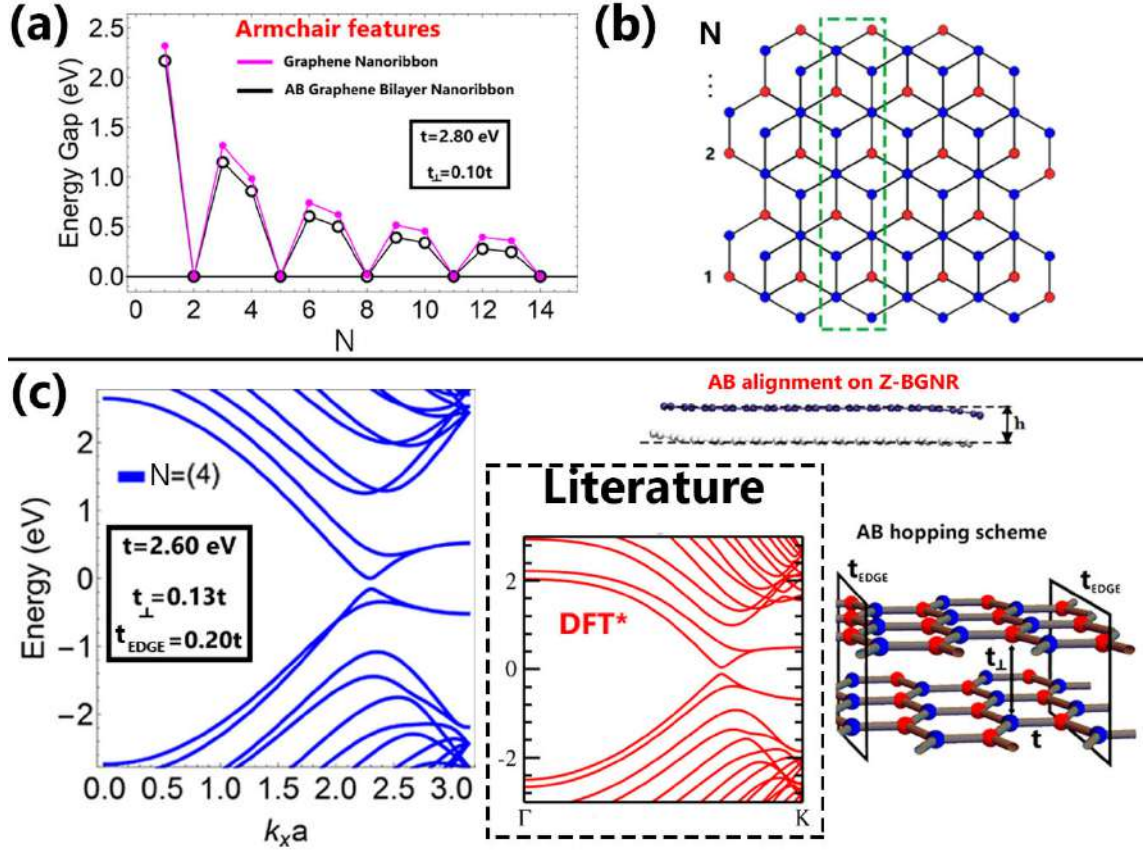
Figure 2.15: Results obtained for armchair and zigzag bilayered graphene nanoribbons. (a) Energy band gap evolutions comparing the monolayer and bilayer cases of armchair graphene sheets. (b) Top: Z-BGNR unit cell representation. Bottom: Hopping scheme model adopted, with t intralayer and $t_\perp$ intralayer hoppings. The t_{EDGE} regions are represented by square around the edges of each layer. (c) On the left, in blue, TB results and on right, red DFT results *[24]

create an overlap between the electronic clouds of neighbors carbon atoms in the layers which is

not taken into consideration in our calculations. Thus, in more complex systems with different

hybridizations the interaction between those electronic clouds becomes an important factor to the

electronic structures. Because of that, our zigzag calculations performed with our simple TB model

for Zα-BGyNRs including the edge hoppings are not enough to get comparable results with first

principle calculations. Besides that, more simple systems like graphene, including a hopping term

t_{EDGE} in Z-BGNRs is sufficient to obtain results in good agreement with the ones obtained by DFT

[24, 86] for zigzag BGNR.
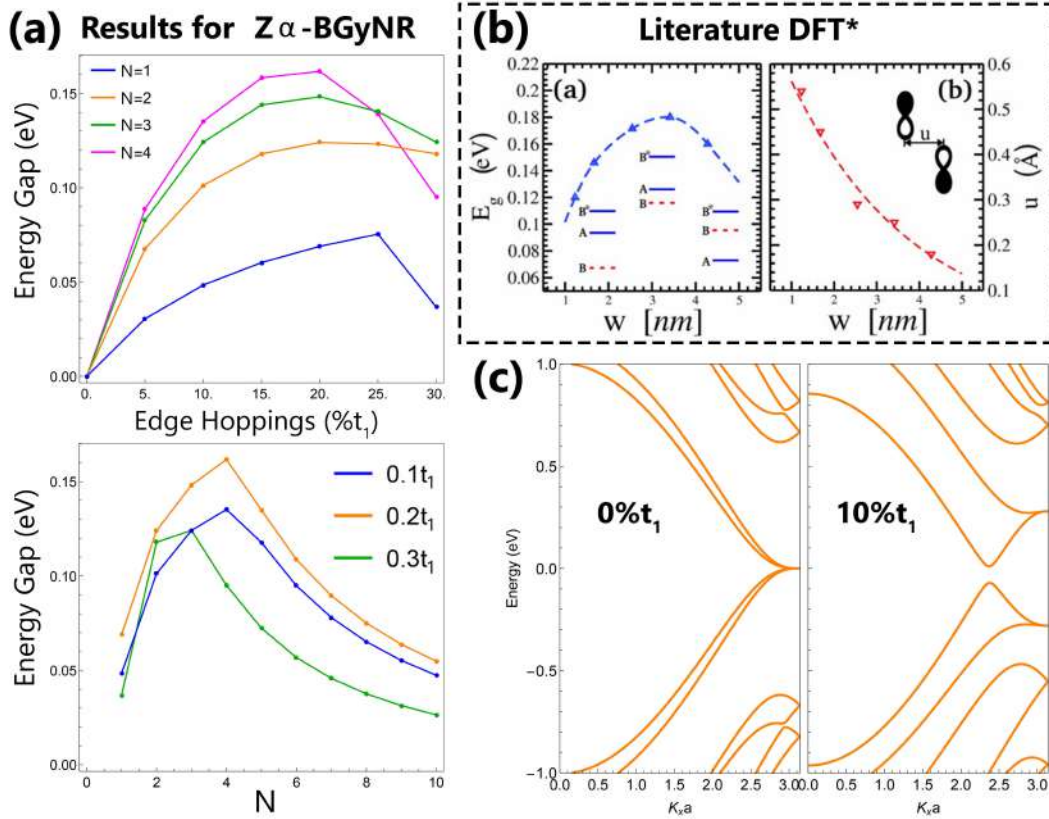
Figure 2.16: (a) Top: Gap evolution vs Edge hoppings percentage ($t_{EDGE} = \%t_1$) Bottom: Gap evolution vs Nanoribbon size (n) for $t_{EDGE} = 10\%t_1$, $20\%t_1$, $30\%t_1$, in blue, orange and green, respectively. (b) DFT*[24, 86] calculations for Z-BGNRs with edge hoppings for $(b)_{(a)}$ Energy gap and $(b)_{(b)}$ orbitals distance, versus nanoribbon length, respectively. (c) Energy bands for Zα-BGyNR with $N_Z = 2$ and hoppings $0\%t_1$ and $10\%t_1$, respectively.

The energy gap achieved by considering the interaction between the edges can be tuned according to the edge hopping energy, considered in terms of the t_1 values ($\%t_1$) and also as a function of the nanoribbon width. Both results are shown in Fig. 2.16(a). The parabolic trend observed for the Zα-BGyNRs results are also obtained in our group by performing DFT calculations [81] for the zigzag system. However, our maximum gap values occur at different nanoribbon widths, indicating that the simple TB model does not provide equivalent results with the DFT calculations. The same parabolic feature was reported before [24] for Z-BGNRs as depicted in Fig. 2.16-$(b)_{(a)}$. As shown in Fig. 2.16-$(b)_{(b)}$, for increasing nanoribbon sizes the overlap between the edge hoppings are minimal. The energy bands for Zα-BGyNRs are shown in Fig. 2.16(c). The hopping parameters are chosen to better fitting with the DFT results. For $N = 2$, they are:; $t_1 = 2.85$ eV, $t_2 = 4.0$ eV, $t_\perp = 0.37$

eV, $t'_\perp = 0.23$ eV. As we can see, the edge hopping energies are responsible to open a band gap and break the electron-hole symmetry of the electronic spectra.

In conclusion, a simple TB method can satisfactorily calculate electronic properties of near band transitions in armchair non-metallic graphyne samples (mono and bilayered sistems). However, for the zigzag features, we need further the inclusion of electronic correlations due to the edge states to get reasonable agreements with first principle calculations. Advances studies have been already started in this direction. Better adjustments are still lacking to improve the TB approximations such as a proper incorporation of the ribbon bending effect due to relaxation processes. More than stacking the monolayers, we can make a rotation between the layers for specific angles, and with that it should be possible to expect further interesting effects that will be approached in the following section.

2.3   Overview: Moiré Effect in Twisted Bilayer Graphene

The Moiré effect is a very common optical pattern, obtained by the interference of electromagnetic waves when crossing through grids shifted by a very short amount. More recently, this effect was also observed for electrons in carbon materials at specific angles, defined as commensurable angles, in twisted bilayered-systems. For really specific angles between the layers, called magical angles, near from $1.1°$, the twisted bilayer graphene (TBG) is know for its superconductive properties due to strongly correlated electronic interactions at magic angles [28], leading to the emergence of flat bands, as indicated in Fig. 2.17(b) taken from Ref.[29].

The mismatch between the rotated layers are responsible to produce the Moiré effect. As illustrated in Fig. 2.17(a) for non commensurable angles as $60°$, the moiré effect can not be seen. To determine the commensurable angles responsible for that, we start from the graphene unit vectors

$$
\begin{aligned}
\vec{a_1} &= a(-1/2\hat{i} + \sqrt{3}/2\hat{j}), \\
\vec{a_2} &= a(1/2\hat{i} + \sqrt{3}/2\hat{j}), \qquad w/ \qquad \vec{a} = a\hat{i}
\end{aligned}
\tag{2.6}
$$

The position vector at the fixed layer is defined as $\vec{r} = m\vec{a_1} + n\vec{a_2}$ while the vector at the twisted layer is given by $\vec{t_1} = \alpha\vec{a_1} + \beta\vec{a_2}$, with n, m, α, β being integer coefficients. We determine α, β as
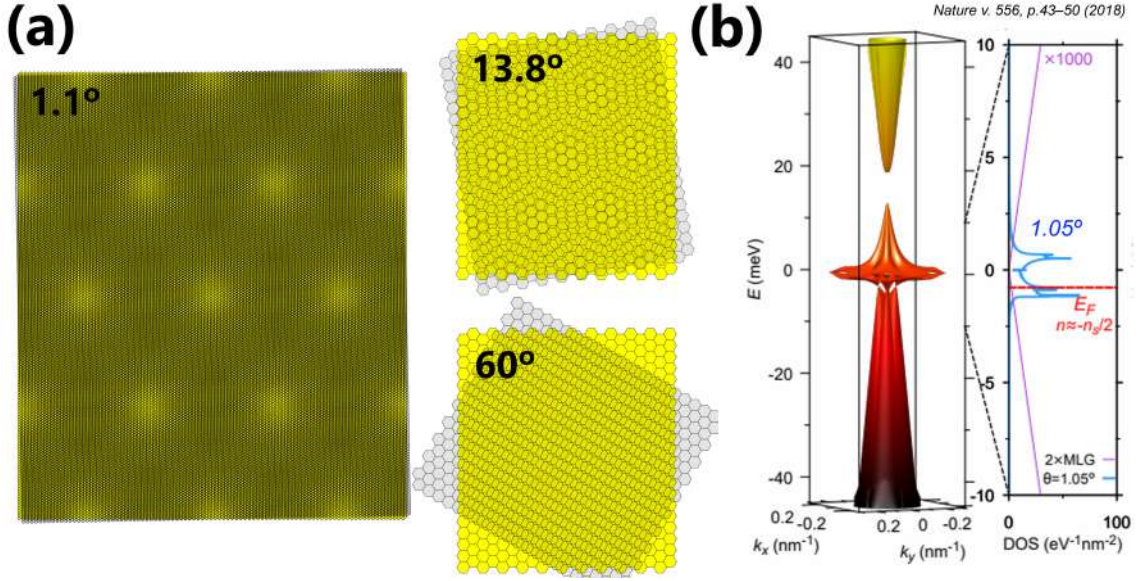
Figure 2.17: (a) Structures generated in Mathematica for commensurable angles $\Theta = 1.1°$ and 13.8° and for non commensurable angles $\Theta = 60°$ and . (b) Energy flat bands and DOS observed for TBG at $\Theta = 1.05°$ near ± 15 meV. Adapted from.[29]

a function of n, m such that the relation $\vec{r} - \vec{a} = \vec{t_1}$ is satisfied. Substituting the vectors $\vec{a_1}$, $\vec{a_2}$ and solving a linear system of equations, we get $t_1 = n\vec{a_1} + m\vec{a_2}$, with $n = m + 1$. The next step is to determine $\vec{t_2}$ from a rotation of the vector $\vec{t_1}$. By hypothesis, the angle between these two vectors is fixed, as they both delimit the area of the unit cell to be determined. In addition, due to the hexagonal geometry, the angle between these two vectors should be 60°. Thus, we can write that $\vec{t_2} = \mathbf{R}.\vec{t_1}$ [87], with $\mathbf{R} = \mathbf{R}(60°)$ being the rotation matrix. By multiplying the rotation matrix we obtain the rotated vector in terms of the $\hat{i}, \hat{j}$ coordinates $\vec{t_2} = (m + n/2)\hat{i} + \sqrt{3}/2 \ n \ \hat{j}$; in terms of the primitive vectors ir is written as $\vec{t_2} = -m\vec{a_1} + (n + m)\vec{a_2}$.

We can see in the left part of Fig. 2.18 that the vectors $\vec{t_1} + \vec{t_2}$ delimit the parallelogram that grows as n varies. These regions are exactly the smallest cells responsible for the reproduction of the system periodically. We still need to determine the commensurable angles for which the rotations does generate a Moiré pattern, corresponding to a strong electronic localization of the system. To obtain the commensurable angles, we need to calculate the angle between the vector of the fixed layer $\vec{r}$ and the angle of the vector of the twisted layer $\vec{t_1}$. Thus [88],
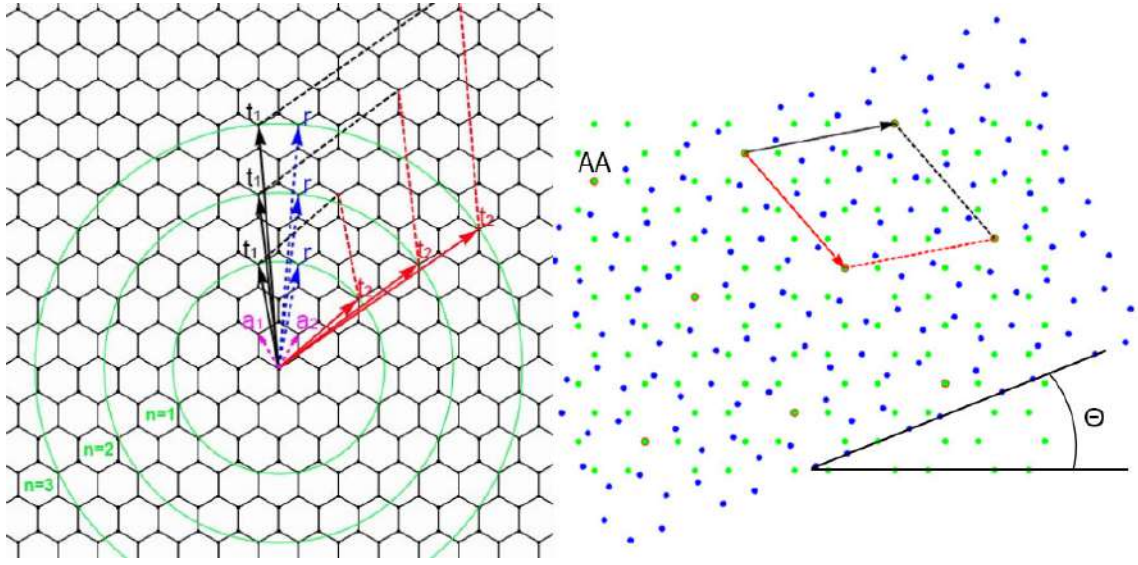
Figure 2.18: Left: Geometric illustration of base vectors as a function of the integers n and m that define the size of the lattice [cases n=1, 2 and 3]. Right: Illustration of the unitary cel for n=1 ($\Theta = 21.78°$).

$$r.t_1 = |\vec{r}||\vec{t_1}|cos\Theta$$

$$\rightarrow \Theta(n,m) = \arccos[\vec{r}.\vec{t_1}/|\vec{r}||\vec{t_1}|] \tag{2.7}$$

$$\rightarrow \Theta(n,m) = \frac{(m^2 + 4mn + n^2)}{2(m^2 + mn + n^2)^2}.$$

Using this relation, we determine the commensurable angles that are responsible to give the size of the system unit cell, as illustrated for the first case on the right of Fig. 2.18 for $\Theta = 21.78°$. We can also determine the function $N(n,m)$ which gives us the number of atoms per unit cell. The rate of the area delimited by $\vec{t_1} \times \vec{t_2}$, and the area of a regular hexagon gives the number of hexagons per unit cell. Multiplying the result by 2, factor associated with the layer number, and by 6, corresponding to the number of atoms per hexagon, we determine the number of atoms distributed in the unit cell, $N(n,m) = 4(m^2 + mn + n^2)$. We can notice, that for angles close to the magic angle our system reaches 4 decimal places for the number of atoms involved.

As the number of elements in the Hamiltonian matrix is defined by the number of atoms in the unit cell, for 1.08° we get a 11164 x 11164 matrix, requiring a significantly large computational effort to perform the calculations of the eigenvectors and eigenvalues. The Hamiltonian of this system is constructed with the same structure as bilayered one, with elements i, j,

48

$$H_{int}[[i,j]] = t_{\perp} = t_0 Exp\left[\frac{d(i,j)}{\beta}\right] \tag{2.8}$$

where $d(i,j)$ is the Euclidean distance between the lower layer site (not twisted) and the upper layer site (twisted) and the dimensionless β adjustment parameter, which usually can vary between -3 and -2.5 [88].
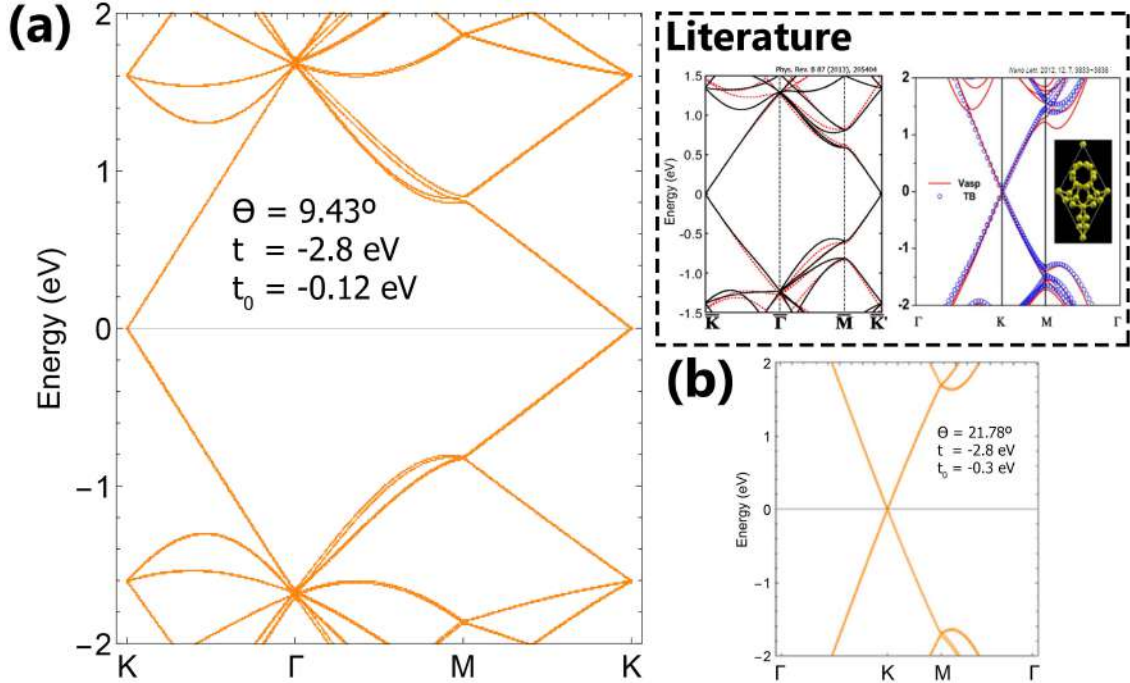
Figure 2.19: Energy bands for: $\beta = -3$, $t = -2.8$ eV (a) $\Theta = 9.43°$ and $t_0 = -0.12$ eV (b) $\Theta = 21.78°$ and $t_0 = -0.3$ eV. DFT and TB calculations adapted from [89] and [90], respectively, are shown in the dashed square in the top-right section.

The electronic structures of 2D bilayered Gy for $\Theta = 21.8°$ and $\Theta = 9.43°$ are shown in Fig. 2.19(a) and (b), along the high symmetry points, $\Gamma = [0,0]$, $K = (\vec{b}_1 - \vec{b}_2)/3$, $and M = \vec{b}_1/2$. Our results (orange curves) are compared with other theoretical calculation [89, 90] presented in the dashed frame in Fig. 2.19 exhibiting a reasonable agreement.

In the next chapter we drive our efforts in discussing fractals systems, considering flakes made of Sierpinski triangle compositions and some molecular chains composed of ST units. It is interesting at that point to mention that systems with standard geometries may exhibit fractal properties by applying a perpendicular magnetic field to the layer. In this case the electrons are confined in the

unit cell, travels under the effect of an external field, and then changes its hopping phase. The patterns shown when the external magnetic field is observed along the available electronic energies are fractal. Further aspects of electrons moving through a lattice with external magnetic field is discussed in the following Chapter.

Chapter 3

Fractal Properties of Carbon Materials

In a physics conference at MIT, Dr.Richard Feynman, when asked about the physical problems to be solved in the future after the sec.XX, replied: *"There's Plenty of Room at the Bottom"*, concluding that a lot of contents in physics are about to be discovered, and studied. Until now, we have seen that experimental realizations of fractals in nanometric systems are a reality. This is not surprising, indeed, the condensed matter systems are strikingly related with the geometric properties, as shortly exposed in this work. Recent results show that electrons and photons interacting within a fractal lattice behaves like particles in a fractional dimension [34, 91]. In this Chapter we investigate the fractal patterns in the electronic properties of some systems. The self-similarity appears at specific energy intervals between each fractal order, and have equal spectra for each generation observed. Moreover, a magnetic field applied across a standard (not fractal) geometry can create a fractal pattern in the electronic energy spectra,exhibiting a coexistence between free and periodic electrons in a crystal .

3.1   Landau Levels

Magnetic field is a fundamental ingredient of crucial interactions and elementary theory in condensed matter. Motivated by Bloch studies (1925) on a confined electron, Lev Landau was

concerned to solve the problem of a free electron in a perpendicular strong applied magnetic field. Within the Drude electron gas theory, the hamiltonian is given by

$$H = \frac{\hat{p}^2}{2m} \tag{3.1}$$

with $\hat{p} = -i\hbar\nabla$. In the presence of a magnetic field B_z applied in the z-direction, the electron movement is restricted to the x,y-axis. The Pierls substitution for the momentum in the Hamiltonian gives [92]

$$\hat{H} = \frac{\left[\hat{p} + e\vec{A}(r)\right]^2}{2m} \tag{3.2}$$

where e is the electronic charge and $\vec{A}(r)$ is the potential vector. In this problem the free electron energy is quantized into separate levels known as Landau Levels (LLs) and the problem could be interpreted as a quantum harmonic oscillator with a cyclotron frequency $w_c = eB_z/m$ [93]. The accessible energies are

$$E_n = \hbar w_c \left(n + \frac{1}{2}\right) \tag{3.3}$$

with n being an integer.

The energy spectra in function of the magnetic field and the density of states in function of the energy are represented in Fig. 3.1. The LLs are highly degenerated in energy and each peak in the DOS is separated by a factor proportional to the applied magnetic field B_z.
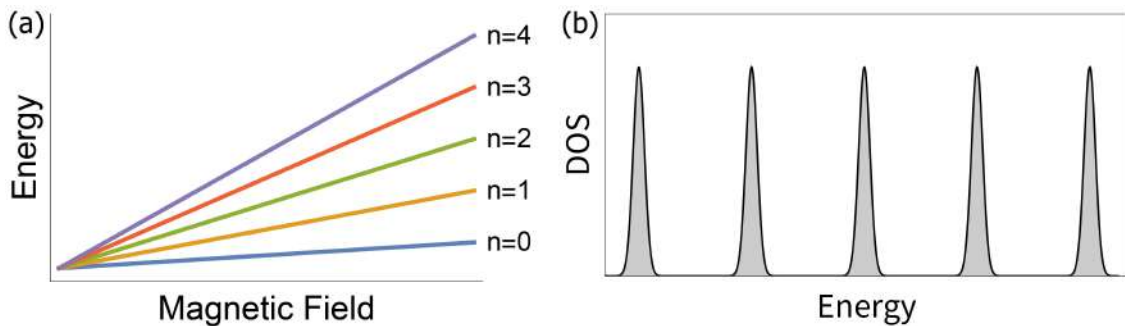
Figure 3.1: Representation of the Landau Levels a) Energy spectra in function of the magnetic field b) DOS as a function of the free electron energy.

For the case of the free electron we see a linear relation between the energy spectra and the

magnetic field. Notice that $w_c = \frac{eB_z}{m} = \frac{\hbar}{ml_B^2}$, with $l_B = \sqrt{\hbar/eB}$ being the magnetic length.

Now, considering the electron moving inside a lattice, with atoms distance a, we can add a periodic potential $U(r) = U(r + a)$ into Eq. 3.1

$$\hat{H} = \frac{\left[\hat{p} + e\vec{A}(r)\right]^2}{2m} + \hat{U}(r). \tag{3.4}$$

Now, considering the periodic potential of a graphene monolayer (MG) and a graphene bilayer (BG), the energy spectra are shown to be proportional to $E \propto n\sqrt{B}$ and $E \propto nB$, respectively, as illustrated in Fig. 3.2.
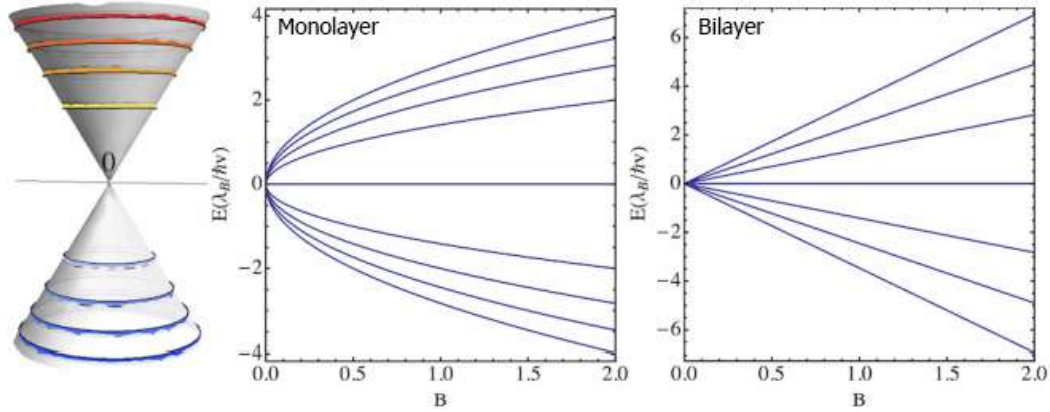
Figure 3.2: Left: LLs in Dirac Cone of the effective model for MG. Medium: Energy spectra for MG. Right: Energy spectra for BG. Adapted [94].

In a periodic medium, Bloch bands emerge in the energy spectra. In the presence of a external applied magnetic field the energy degeneracy is broken. A plot of the eigenvalues of this system versus the magnetic flux produces a beautiful fractal figure, obtained first by Hofstadter in 1976. In the following sub-section we briefly reproduce his calculations and derive the Hodstadter butterfly for different lattice systems.

3.2 Hofstadter Butterfly

We have seen that electronic energy can be quantized in two ways, by the lattice potential and by an applied magnetic field. In this sub-section we consider both quantities in a square lattice as performed by Douglas Hofstadter [95]. The first calculations of a lattice in a magnetic field where performed in 1955 by P.G. Harper [96], however, he did not succeed in obtaining the solutions of his equations for different values of magnetic field. Later Hofstadter proceed with the calculations finding a beautiful fractal figure as we discuss now.

The translation operator presented in Sec. 1.1 together with the Peierls substitution is $T_{\vec{R}} = \exp\left\{\frac{i}{\hbar}(\vec{p}.\vec{R}) + \frac{ie}{\hbar}(\vec{R}.\vec{A})\right\}$. Applying to a Bloch orbital

$$T_{\vec{R}} \ \phi(\vec{r}) = \exp\left\{\frac{ie}{\hbar}\left(\int_{\mathcal{C}} \vec{A}.d\vec{r}\right)\right\} \phi(\vec{r}+\vec{R}) \tag{3.5}$$

where the vector potential $\vec{A}$ changes continuously along the curve $\mathcal{C}$ and $d\vec{r}$ changes with unitary cell. Using the hopping definition

$$t'_{\vec{R},\vec{R}'} = \int d\vec{r} \ T_{\vec{R}'}\phi^*_{\vec{R}'} \ \mathcal{H} \ T_{\vec{R}} \ \phi_{\vec{R}} \tag{3.6}$$

substituting the translation operator 3.5 we obtain

$$t'_{\vec{R},\vec{R}'} = \exp\left\{\frac{ie}{\hbar}\left(\int \vec{A}.d\vec{r}\right)\right\} t_{\vec{R},\vec{R}'} \ . \tag{3.7}$$

We conclude then, that the external magnetic field changes the hopping term by a phase related to the vector potential. This effect is related with the Aharonov–Bohm (AB) effect, in which, the wave function of a particle obtains a phase even in regions without a measurable magnetic field, as evidenced in the AB effect [97]. Thus, we define the Peierls phase as

$$\Phi = \frac{e}{\hbar} \int \vec{A}.d\vec{r} = 2\pi\frac{\Phi_B}{\Phi_0} \tag{3.8}$$

with $\Phi_0 = h/e$. The system geometry changes the magnetic flux Φ_B. Usually, for the adopted Landau gauge $\vec{A} = (0, Bx, 0)$, inside the square unit cell, we have $\Phi_B = aBx$. Taking into account only one displacement along x-direction; $x = a$ gives $\Phi_B = a^2 B$. Using $l_B^2 = \hbar/eB$ we can define a flux over the magnetic unit cell area

$$\alpha = \frac{\Phi_B}{\Phi_0} = \frac{a^2 B}{h/e} = \frac{(a/l_b)^2}{2\pi} \Leftrightarrow \Phi = 2\pi\alpha. \tag{3.9}$$

The α value is given by the ratio between the lattice parameter a and the magnetic length l_B. With this quantity, we could have two regimes. When a is much smaller than l_B, and then we have the LLs and the Drude model is applicable. Or when the both quantities are comparable, in this case, the lattice is important for the study of electron behavior. Thus, the size of the spatial unit cell is inversely proportional to the size of the magnetic unit cell. The modulus of the magnetic field in Eq. 3.9 could be written as $B = \alpha/a^2 \Phi_0$, in this way if $\alpha = 1$, then the applied magnetic field decreases with $1/a^2$. Then, the larger is the spatial unit cell, the smaller is the applied magnetic field to obtain the Hofstadter butterfly. For this reason, the TBGs with super-cells are largely used to construct experimental Hofstadter butterflies [98] as in Fig. 3.3.
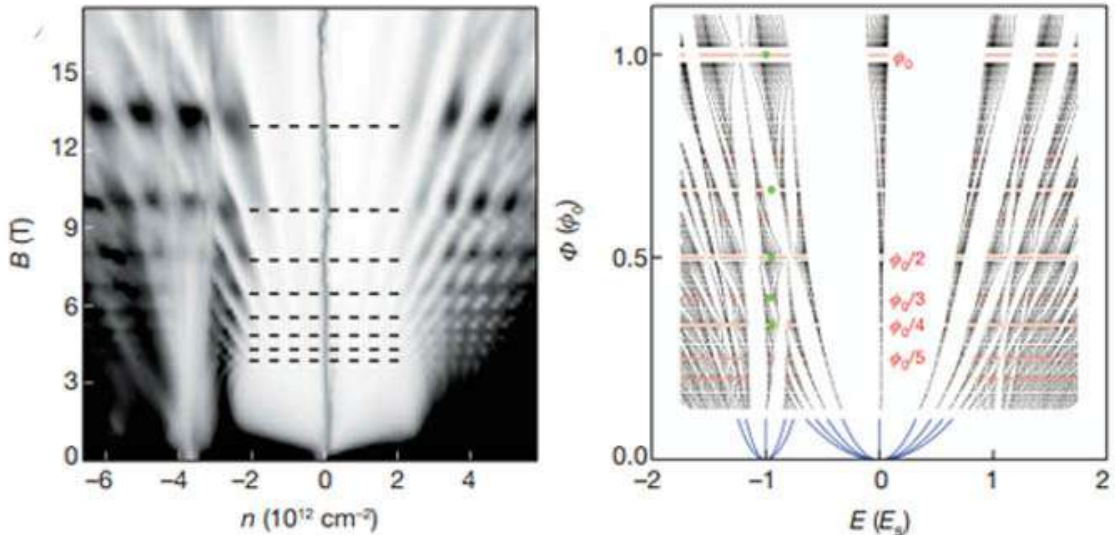
Figure 3.3: Left: Experimental magnetic field versus carrier density Right: Modeled Hofstadter butterfly with Landau levels in blue [Adapted [98]]

In a square lattice, for the first neighbors TB Hamiltonian in Eq. 1.12, the annihilation(creation)

operators act on the ith lattice sites given by $\vec{R}_i = m_i a\hat{x} + n_i a\hat{y}$, with m and n integers. Thus, the Peierls phase from two consecutive atoms is,

$$\Phi = \frac{2\pi}{\Phi_0} B m_i a.(n_j a - n_i a). \Phi = 2\pi m_i \alpha$$

Note that we have the same result $\Phi_B = Ba^2$ in Eq. 3.9 if $m_i = 1$, $n_j = 1$ and $n_i = 0$, which is the first magnetic unit cell with two atoms. Due to the periodicity of the lattice, the magnetic cell could be displayed in x or y directions, quantified by p and q, respectively. In this case, due to the adopted Landau gauge, only the y-direction hoppings will be changed. Further, we can define α as a rational number [95]

$$\alpha \equiv \frac{p}{q} \quad ; \quad \alpha \ between \ 0 \ \& \ 1 \tag{3.10}$$

with p and q being integers that give the size of the magnetic unit cell. The magnetic field $B = \Phi_0 p/qa^2$ have large values for $\alpha = 1$ due to the lattice parameter $a \approx 10^{-10}$ m. In the case illustrated in Fig. 3.4, the spatial unit cell is marked in orange and the magnetic unit cell (red region) displayed along the x direction, with area given by $(1 \mathrm{x} q).a^2$. In this system the hopping
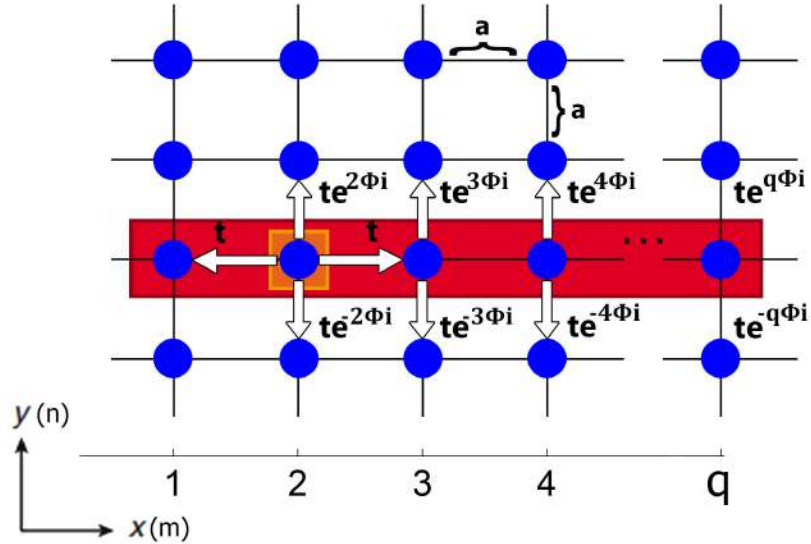
Figure 3.4: Scheme of the magnetic field in a square lattice. Orange square: Spatial unit cell for p=1 and q variable. Red rectangle: Magnetic unit cell.

integral in the x-direction does not change due to the particular conditions of the Peierls phase:

$$\exp\{(0, Bx, 0).(1, 0, 0)\} = 1$$

Otherwise, the hopping integral in the y direction depends on the x position along the magnetic cell and the Hamiltonian is written as

$$H = \begin{pmatrix} h_1 & te^{ik_x a} & 0 & \ldots & te^{-ik_x a} \\ te^{-ik_x a} & h_2 & te^{ik_x a} & \ldots & 0 \\ \vdots & \vdots & \vdots & \ddots & \vdots \\ te^{ik_x a} & 0 & 0 & \ldots & h_q \end{pmatrix} \tag{3.11}$$

where $h_m = cos(k_y a + m\Phi)$ and $(m = 1, 2, ..., q)$. Note that at the end of the unit cell $m = q$. This leads to a q-level Schrodinger equation to be solved, as described in the TB section. Without magnetic field, or when α assumes an integer value the energy levels are simply $E = 2t[cos(k_y a) + cos(k_x a)]$.
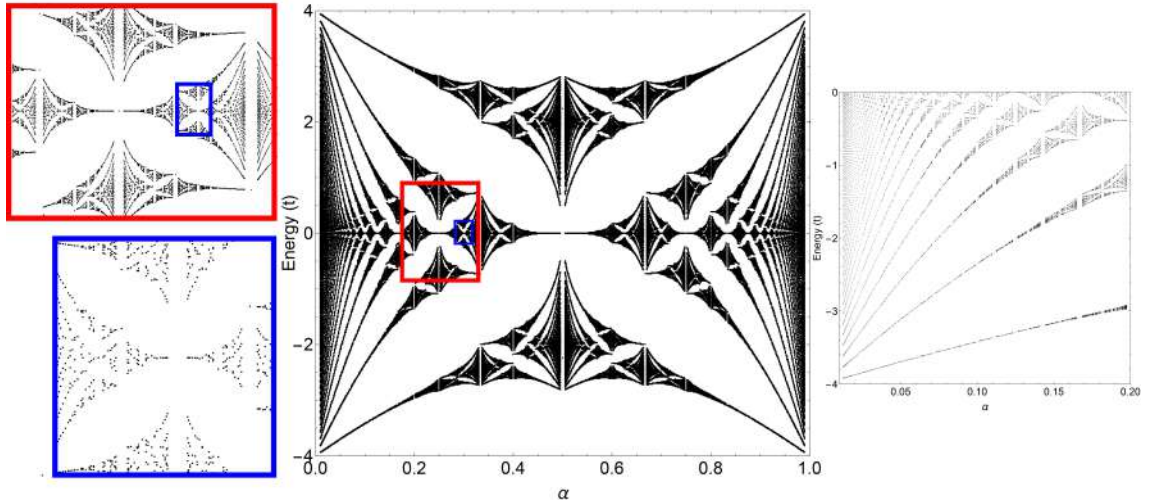
Figure 3.5: Left: Zooms of an arbitrary region in the butterfly. Medium: The Hofstadter butterfly of a square lattice for q=80. Right: Landau levels in the butterfly.

The energy spectra shown in the center of Fig. 3.5 is obtained for an electron in a periodic potential exposed to a large magnetic field. Known as Hofstadter Butterfly, this figure shows a fractal pattern in arbitrary regions. Box counting calculations agrees with a fractal dimension

D=1.77 for the Hofstadter Butterfly in literature [99]. In the red and blue boxes we compare zoomed regions in the butterfly spectrum. We verify that the figure is a fractal, showing a self-similarity for each inset. Further interesting features are largely explored in the butterflies, such as topological invariants called Chern numbers, which are directly related to the quantization of the Hall conductivity in the integer Quantum Hall effect [100, 101, 102]. Also, near from integer α values the butterfly regions became similar to the LL for free electrons.
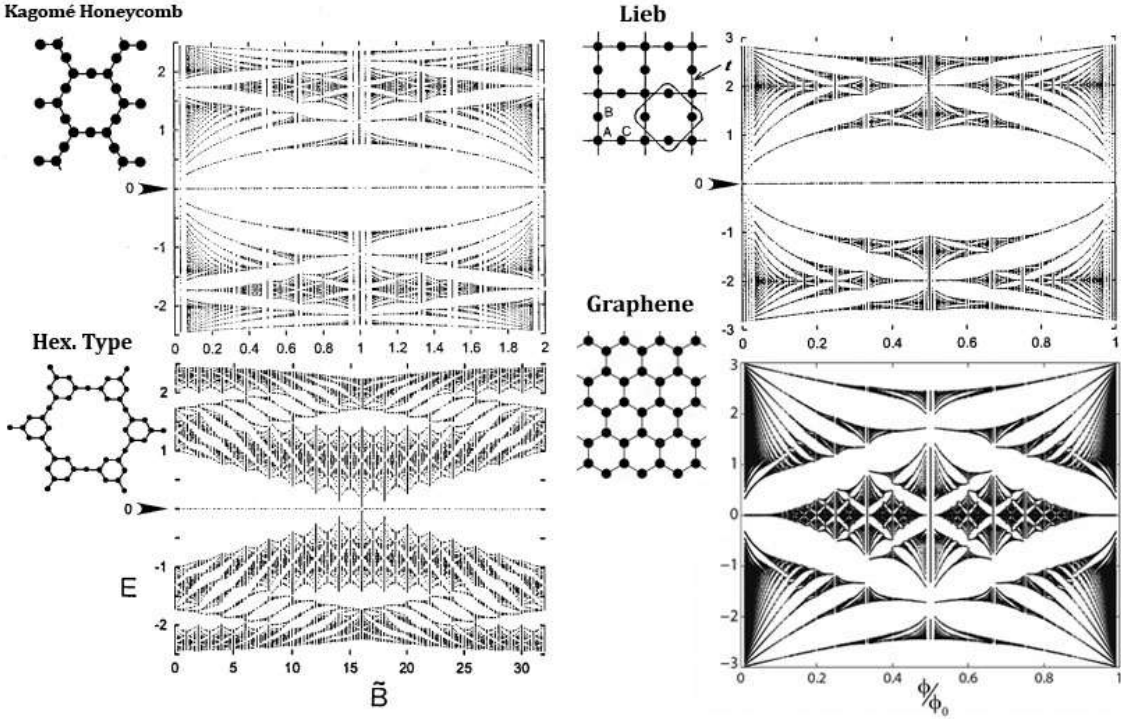
Figure 3.6: Butterfly spectrum for different lattice structures. The flat band of each system is signalized with the black arrow [Adapted from [102]].

Other spectra are further illustrated for different structures as shown in Fig. 3.6. We can observe that the full periodicity of the butterfly spectra is achieved at particular flux values that depend on the lattice parameter, being extremely sensitive to disorders and defects in the lattice [103]. Also, the flat states marked with black arrows in the figures, are preserved as can be noticed for the Kagomé Honeycomb studied before.

3.3 Conventional ST Flake Model

Inspired on the possibility of engineering real structures based on the geometries of the Sierpinski triangle we developed a recursive process to describe ST of different generations, based on the Green's function formalism. Our first emphasis is to investigate fractal features on the electronic properties of ST flakes. Here we show the results of the density of states (DOS) for conventional ST flakes in terms of the order generation l.
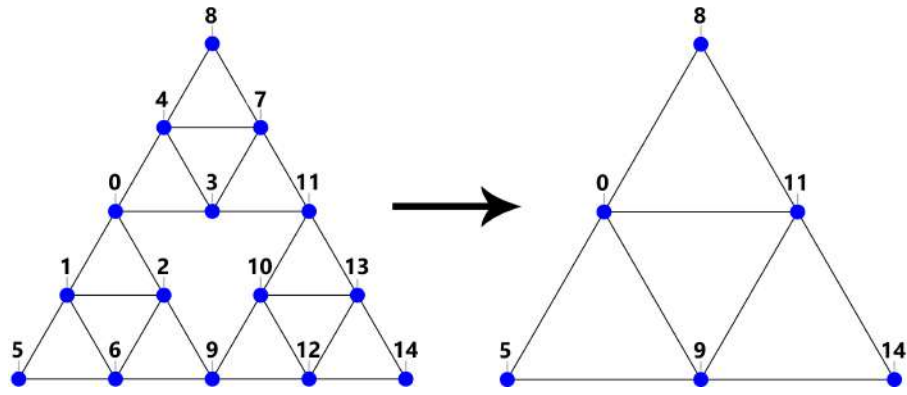
Figure 3.7: Illustration of the decimation method in which a G(2) ST is reduced to a G(1) ST.

The electronic properties are obtained by using the single first neighbor tight binding Hamiltonian, described in Eq. A.3 and putting $t' = 0$. The hopping energy matrices follow the corresponding connectivity of the l-order ST [G(l)], illustrated in Fig. 3.7. The DOS is given by

$$\rho_i(E) = -\frac{1}{\pi} Im G_{ii}(E).$$

(3.12)

The Dyson equations [see Appendix. B] relating the real-space Green functions, among the

15-atoms of the second ST generation, shown in Fig. 3.8, can be written as,

$$G_{00} = g_0 + g_0 t[G_{10} + G_{20} + G_{30} + G_{40}] \tag{3.13}$$

$$G_{10} = g_1 t[G_{00} + G_{20} + G_{60} + G_{50}]$$

$$G_{20} = g_2 t[G_{00} + G_{10} + G_{60} + G_{90}]$$

$$G_{30} = g_3 t[G_{00} + G_{40} + G_{70} + G_{110}]$$

$$G_{40} = g_4 t[G_{00} + G_{30} + G_{70} + G_{80}]$$

$$G_{60} = g_6 t[G_{10} + G_{20} + G_{50} + G_{90}]$$

$$G_{70} = g_7 t[G_{30} + G_{40} + G_{80} + G_{110}] \, ,$$

where the propagator $g_i(E) = 1/(w - E_i)$ and $t = t_{i,j}$ corresponds to the energy hopping between two first neighboring atoms i and j in the lattice, which were considered identical. After some algebraic manipulations involved in a decimation procedure[104], and considering $g_i = g_0$, for all sites i, we obtain a renormalized Dyson equation for the G_{00} locator,

$$G_{00} = \tilde{g}_0 + \tilde{g}_0 \tilde{t}[G_{50} + G_{80} + G_{90} + G_{110}] \, , \tag{3.14}$$

corresponding to a reduced ST generation, with the dressed propagator and hopping energy given by,

$$\tilde{g}_0 = \frac{g_0}{1 - \frac{4g_0^2 t^2 (1 + g_0 t)}{1 - 3g_0^2 t^2 - 2g_0^3 t^3}} \, , \tag{3.15}$$

and

$$\tilde{t} = \frac{g_0 t^2 (1 + 2g_0 t)(1 + g_0 t)}{1 - 3g_0^2 t^2 - 2g_0^3 t^3} \, . \tag{3.16}$$

By realizing l iterative process it is possible to obtain the DOS of the $(l + 1) - th$ ST generation. The results for different numbers of iterative processes (1-4) are shown in Fig. 3.8 .

As being finite systems, the DOS are expected to exhibit a sequence of delta functions that increase as the number of atoms is increased, as depicted in Fig. 3.8. A self-similarity of the DOS, emerging from higher l-order STs is evident in the zoom (bottom panel) presenting the short energy range (-1.0t to -0.75t). Particular pinned localized states are found at the same energies,
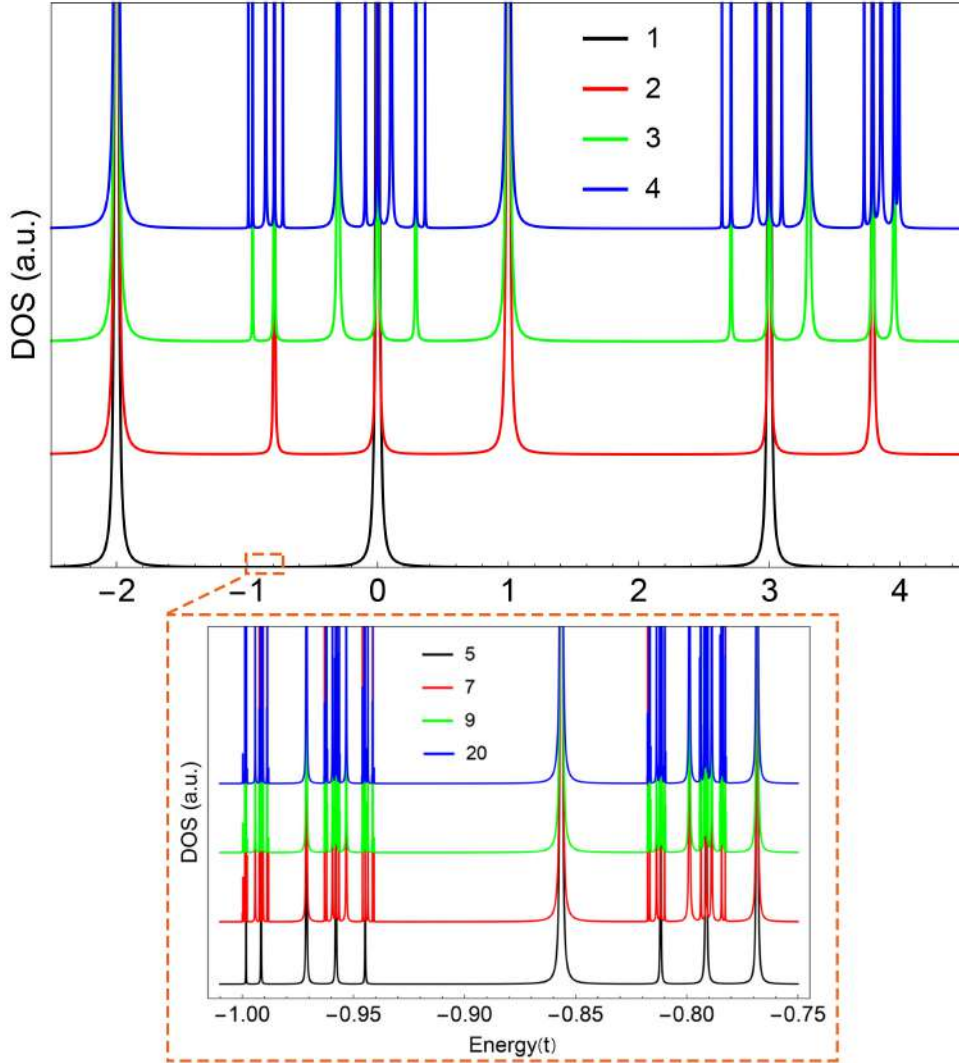
Figure 3.8: DOS as a function of the Fermi energy, calculated from -2.5t to 4.5t for l-ST varying from 1 up to 4. Inset: DOS results within a narrower energy range(marked in the central figure), for l=5, 7, 9 and 20, illustrating the DOS self-similarity.

independently of the ST generation-order. More interesting to note is the fact that all states presented in a given iterative process also appear in the LDOS results of all subsequent iterative steps of higher order, in a cumulative process.

3.4   Kagomé ST Flake Model

Motivated by fractal properties in more realistic systems we propose the Kagomé-Honeycomb ST flake (KHST). In this case we solve the tight-binding system up to second neighbors, as illustrated

in Fig.(3.9)-(a) for armchair-KHST (A-KHST) and in Fig.(3.9)-(b) for zigzag-KHST (Z-KHST). The number of atoms for the armchair (N_A) and zigzag (N_Z) configurations are, respectively,

$$N_A^l = 12 * 3^l + \sum_{i=1}^{l} 3^i \ ,$$

$$N_Z^l = 15 * 3^l + 4 - \sum_{i=0}^{l-1} 3^i, \ \text{for } l > 1 \text{ and } N_Z^1 = 49 \ . \tag{3.17}$$

All the calculations are made using on-site energies equal to $\pm\epsilon = \pm0.25t_1$, with t_1 being the nearest-neighbor hopping, for the blue ($+\epsilon$) and orange ($-\epsilon$) sites, following reports on two-dimensional covalent organic honeycomb frameworks [9], that are typical example of graphene-kagomé lattices. The second nearest neighbor hopping energy is chosen as [34] t_2=0.08t_1. The LDOS is calculated as a function of energy by

$$LDOS(x, y, E) = \sum_n |\Phi_n(x, y)|^2 \delta(E - E_n) \ , \tag{3.18}$$

where x and y are the lattice position coordinates and $\Phi(x, y)$ is the corresponding electronic wave function of the nth state. To compute the delocalized electronic contribution around the sites, given by $|\Phi_n(x, y)|^2$ we transform the

For both KHST edge geometries, the presence of a band gap is verified, for the cases of first and up to second-neighbors, as shown in Fig. 3.9 (right panels), revealing a semiconducting feature to such Kagomé-like ST. Otherwise, the graphene ST flake results, reveal a semiconducting and metallic characteristic for armchair and zigzag GSTs, respectively [38] in the energy-state maps. As noticeable from Figs. 3.9(a) and (b), the gap increases by $\approx 0.16t_1$ when second nearest neighbors are taken into account in the TB model, for armchair and zigzag-edged KHSTs. An interesting feature found in the electronic properties of the KHST gaskets is the reminiscent flat band observed in 2-dimensional Kagomé lattice, highlighted here by the high degeneracy order of the E=-0.25t_1 and -0.41t_1 states, for first and second-neighbor models, respectively, at the gap threshold. The number of such localized degenerate states is expected to increase as the generation order of the gasket is increased, although the size of the gaps do not dependent on the generation order, as depicted in the insets of Fig. 3.9, for armchair and zigzag configurations. Compared with the gap
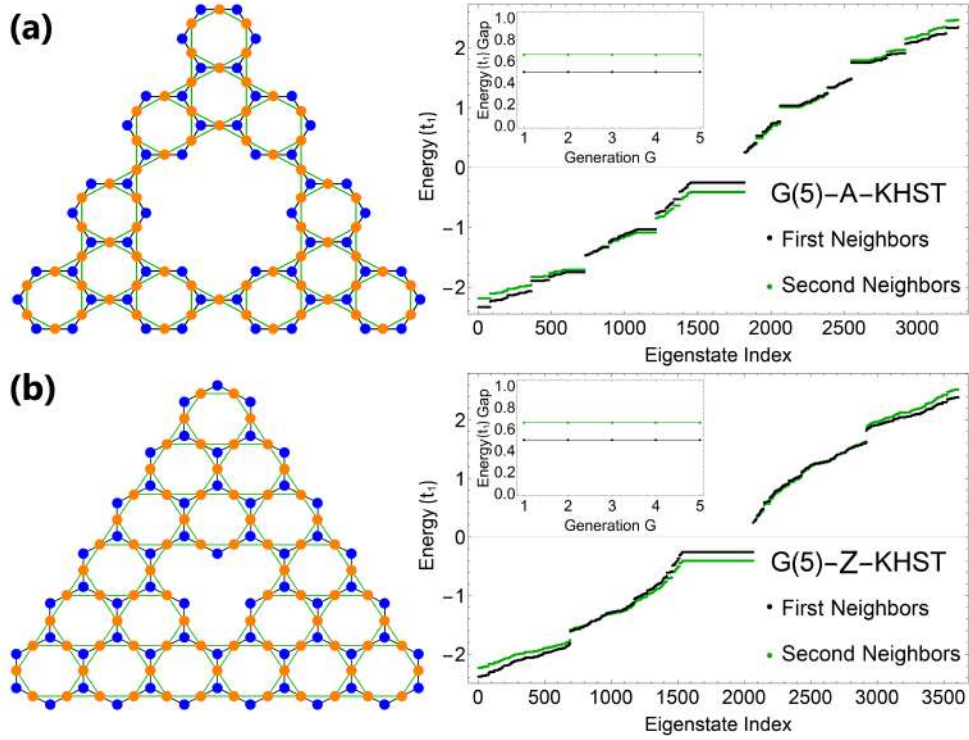
Figure 3.9: Schematic view of the second generation [G(2)] of an (a) A-KHST and a (b) Z-KHST flake at left and the eigenvalues for the 5th generation as a function of the eigenstate indexes at right. Results considering only first and up to second neighbor-hopping energies are depicted in black and green dots, respectively. Insets: gap sizes versus the ST generation.

dependence for GST flakes exhibited in Fig. 3.9(a), for KHST the gap size saturates with l between 3 and 4. We must comment that the number of atoms in the KHST flakes are considerable superior at the same generation order, what may justify the constant gap size achieved already in the first generation. The self similarity is evidenced zooming in the DOS of a G(5)-armchair GST, after each amplifying as evidenced by Perdersen *et al*. For zigzag GST the energy gap can be tuned by adding an electronic correlation with the Hubbard model [38].

Due to the difference in the geometry and site numbers in the basic units forming the KHSTs in comparison to the conventional ST, another fractal dimension definition is used

$$D = \lim_{r \to 0} \frac{Log(N(r))}{Log(r^{-1})} \ , \tag{3.19}$$

with $N(r)$ and r being the number of squares covering the full system, and the square size, respectively. These parameters are used in the box-counting method [36] to perform the dimension

calculation. The dimension of each system is determined by the line slope coefficient of $Log(N(r))$ vs $Log(r^{-1})$ graph presented in Fig. 3.10 (a).

Starting from the atomic spatial localization in the A-KHST flake [see Fig. 6(e)], the sizes (in pixels) of each square found to better adjust the slope are 10 up to 90 pixels. In both cases we take the LDOS image (360 x 360 pixels) and binarize it in a threshold of 30%, to represent the most accurate electronic distribution. The details of such numerical process is described in Refs. [34, 35]. Perfect Kagomé nanoribbons and Kagomé 2D-lattices, exhibit symmetric band spectra, except for the presence of a flat band located exactly at ϵ or $-\epsilon$, depending on the hopping energy signal. For this reason, in this work we choose then the values of $E = \pm\epsilon$ to calculate the maximum contribution in LDOS indicated by its brightest spots, which gives two different patterns, as can be seen in the binarized image shown in Fig. 3.10 (b) and (c).

In this system we have two energy values that the maximum contribution in LDOS is spread through the flake, given origin to the patterns (b) and (c) in Fig. 3.10. Taking them both in the analysis, the box counting method yields a fractal dimension close to the conventional Sierpinski triangle gasket, ≈ 1.585, as can be verified by the slope values shown in Fig. 3.10(a), for both situations (1st and up to 2nd neighbor hopping). This occurs because the brightest spots in the LDOS maps are near from the geometrical points of a A-GST flake, that are also fractal. Otherwise, for energies where the bright spots (high LDOS values) do not reveal the real geometry of the flake, the fractal dimension varies between D=1.30-1.80, as verified by Kempkes *et al.*[34] in hexagonal flakes, varying between low and high contributions of each site for the LDOS, respectively. The self-similarity observed in others ST flakes [34, 38] is also evidenced here for both configurations of the KHSTs (armchair and zigzag), independently on the order of the neighboring hopping taken into account.

A further interesting feature to explore in zigzag and armchair KHST flakes, described by the first and second neighbors approximation, is the asymmetric distribution of the electronic probability distribution at E_1=-0.25t_1 and E_2=0.25t_1 states. Considering the first generation G(1), we found that while the E_1 state is formed by four-fold degenerate eigenstates, the E_2 state is non-degenerated. These states are spread differently among the orange and blue sites of the flake [see Fig. 3.9] , giving raise to the LDOS exhibited in Fig. 3.10 (d) and (e), respectively. The same behavior is evidenced
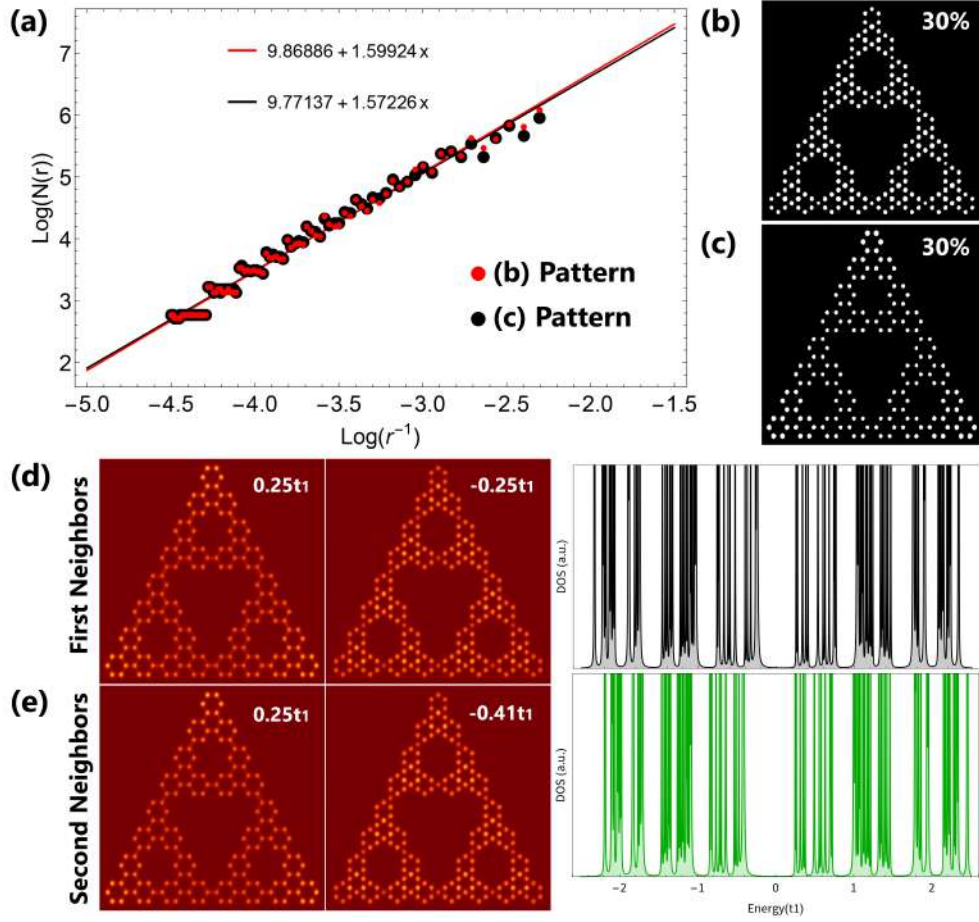
Figure 3.10: (a) Box-counting results of the binarized images (b) and (c) for $\pm 0.25 t_1$, represented by red and black colors, respectively. Total DOS and LDOS of a G(3)-A-KHST for (d) first neighbors at $E = \pm 0.25 t_1$ and (e) second neighbors at $E = 0.25 t_1$ and $E = -0.41 t_1$.

for higher orders of the KHSTs, considering both first and up to second-neighbor hopping models.

3.5 ST Mirrored Chains

Following the experimental realization of 1-D molecular chains [45], with ST as building blocks grown on Au(111), we explore electronic properties of a similar quasi-1D chain as depicted in Fig. 3.11(a). The system was idealized based on the coupling of two hexagonal STs spatially inverted (up and down), with mirror symmetry. Green and black lines connect nearest and second-nearest neighboring atoms, respectively, through the hopping terms t and t' in the tight binding Hamiltonian given in Eq.(1). Differently from the long-range ordered grown structures where Co atoms are present in intercalated benzene lattices [45], our simple model involves exclusively carbon

atoms, denoted by blue dots. The electronic properties are calculated using on site energy $\epsilon = 0$ and following the relation t'=0.08t for the hopping parameters as recently for HSTs [34].
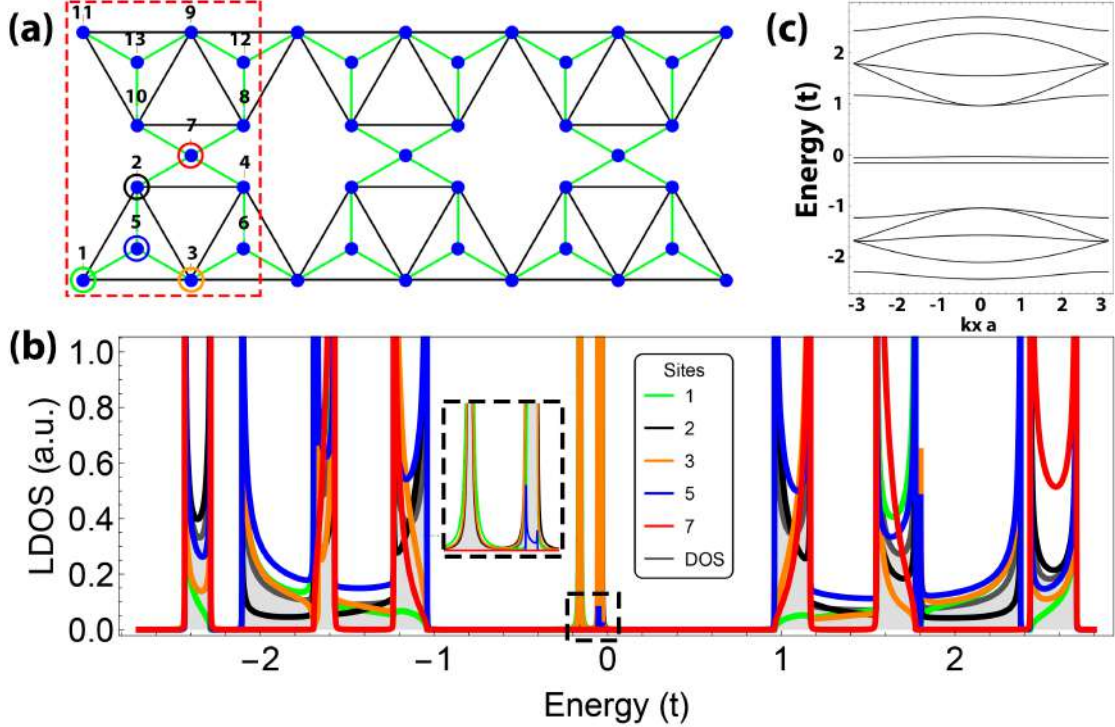
Figure 3.11: (a) Effective G(1)-ST Chain. The green and black lines are related to hopping t and t', respectively. The system extends infinitely along the x-direction. (b) LDOS in function of the energy at sites 1,2,3,5 and 7 identified and colored circled inside the red dashed unit-cell of the ST-Chain, defined in part (a). The total DOS is also shown with pink shadow regions. (c) Band structure of the ST chain for ϵ=0.

The LDOS shown in Fig. 3.11(b) is calculated via Eq. 3.12, where G_{00} is obtained using similar real-space decimation methods, properly constructed to infinite periodic systems as discussed previously. At energies close to the Fermi level, the electronic group velocity is near zero, giving origin to almost two dispersionless bands as can be seen in the corresponding electronic structure shown in Fig. 3.11(c). These flat bands appear as highly peaked density of states, and are highlighted in the inset in Fig. 3.11(b). The different curves correspond to the assigned sites marked with the same color in the unit cell displayed in part (a). As seen in Fig. 3.11(b), at E=-0.16t, the main contribution becomes from sites 1, 2 and 3, and from the symmetric upper sites 11, 10 and 9.

A better visualization of the spatial electronic distribution through the system is displayed in Fig. 3.12 for distinct energies. While part (a) refers to a STM image adapted from ref. [45], Figs.

3.12(b), (c), and (d), are the LDOS theoretical results at $E = -0.16t$ (flat band), $0.96t$ and $1.65t$. In the STM image a high charge distribution appears as bright spots at the relative atomic sites. Correspondingly, in our results the color maps refer to the LDOS intensity. The normalized LDOS results shown in Fig. 3.12(b) reveal that at one of the flat bands [E=-0.16t] not all the atomic sites of the lattice are populated, in according with the previously discussion. This last state appears again in the Dephased ST Chain, and in special, it will not contribute to the transport properties of these systems, as we will see in the next session. Moreover, while at $E = 0.96t$, only sites 2 and
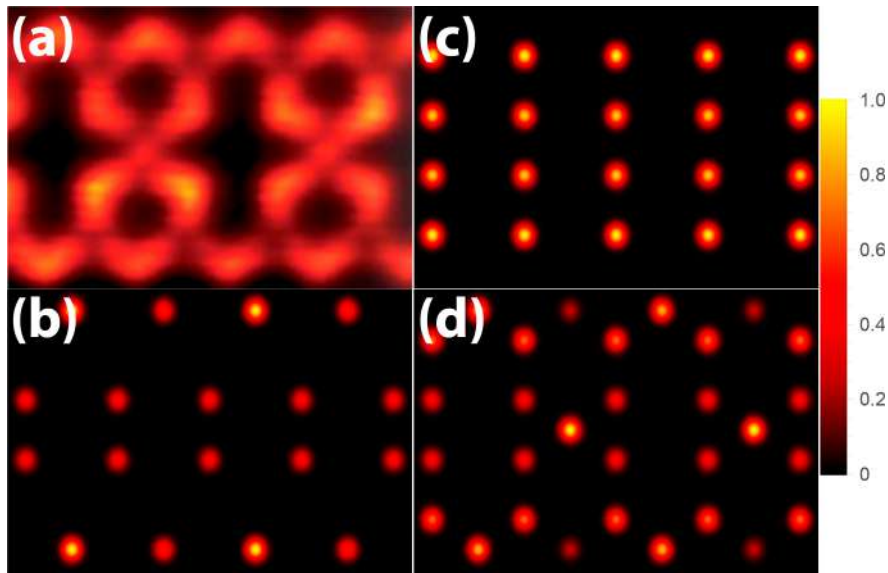
Figure 3.12: LDOS contour plots of a G(1)-ST Chain. a) STM image adapted from the experimental data reported in Ref.[45]. Our theoretical LDOS results for (b) E=-0.16t, (c) 0.96t, and (d) 1.65t.

5, and their equivalents in the unit cell, contribute to the state [see Fig. refstchain(c)], revealing a restricted charge distribution, for the state $E = 1.65t$, Fig. 3.11(d), almost all the lattice is visited generating bright spots in the geometrical net. The later LDOS pattern strongly resembles the cited STM image [Fig. 3.12(a)] indicating that our simple model can be an important tool of modelling such organic molecular chain.

Another experimental alternative of generating 1D mirrored chains made of Sierpiński triangles was proposed in Ref.[46]. We call it as mirrored chain structure-type 2 (MSTC-2). In our model up and down triangles are now fully preserved resembling the STM images shown in Fig. 3.13(a).
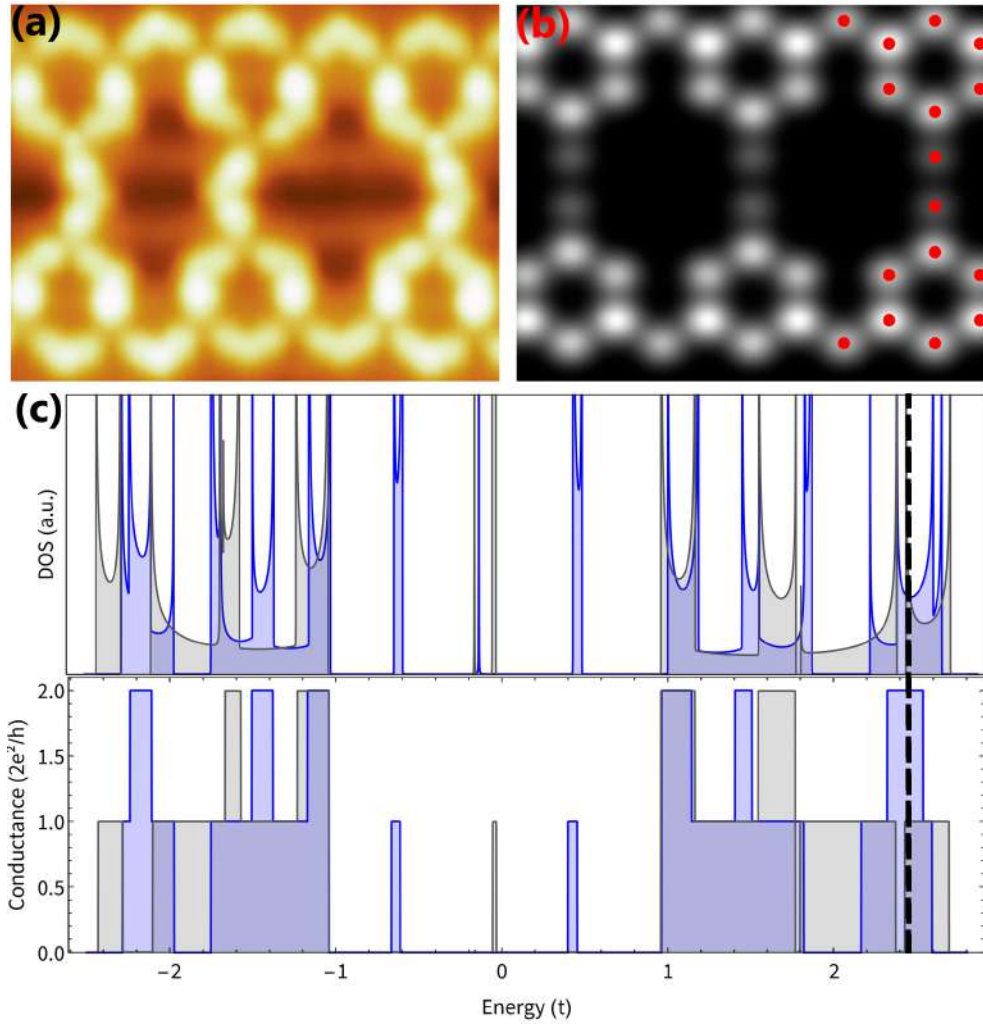
Figure 3.13: (a) STM images of the MSTC-2 [Adapted from [46]]. (b) LDOS of the MSTC for a Fermi energy equal to 2.4t. The nanoribbon unit cell is highlighted with red dots. (c) DOS and conductance results of the MSTC and MSTC-2 in blue and gray, respectively.

The LDOS at a particular energy ($E = 2.4t$) is depicted in part (b) where the region enclosing the nanoribbon unit cell is marked with red circles. The results for DOS and conductance are shown in Fig. 3.13(c), highlighted with shadowed blue curves and compared with the results found for the previous molecular chain [shaded gray curves]. It is noticeable the emergence of two narrowed energy states near the Fermi Level for the MSTC-2, this is a characteristic property of double ST Chains that will be explored in next section. Also, the flat-like states in both chain configurations are preserved in the central gap in DOS, although they are suppressed in the electronic conductance response of each molecular designs due to the high localization features of the flat band.

3.6 Dephased ST Chain

Following the experimental molecular structures presented in Ref.[45, 46], we address now another proposal for ST chain, as illustrated in Fig. 3.14(a). Differently from the previous discussed molecular chains, the new structure are composed by dephased pairs of HSTs [G(2)], connected at particular lateral lattice sites, simulating the packing mode of STs produced by a combination of a Co atom and three BPyB molecules [45]. The unit cell of the dephased molecular chain is marked with dashed red lines. It is interesting to note that our theoretical result for the LDOS at $E = 1.4t$, as shown in Fig. 3.14(d), reproduces quite well the STM image presented in Fig. 3.14(c) for the grown molecular nanostructured.

The electronic properties of the G(2)-dephased ST is shown in Fig. 3.14(b) via the density of states and conductance results. Due to the high electronic localization, the DOS peak at E=-0.16t does not contribute to the electronic conductance in G(2), what happens also for dephased chains of higher ST orders (not shown here).
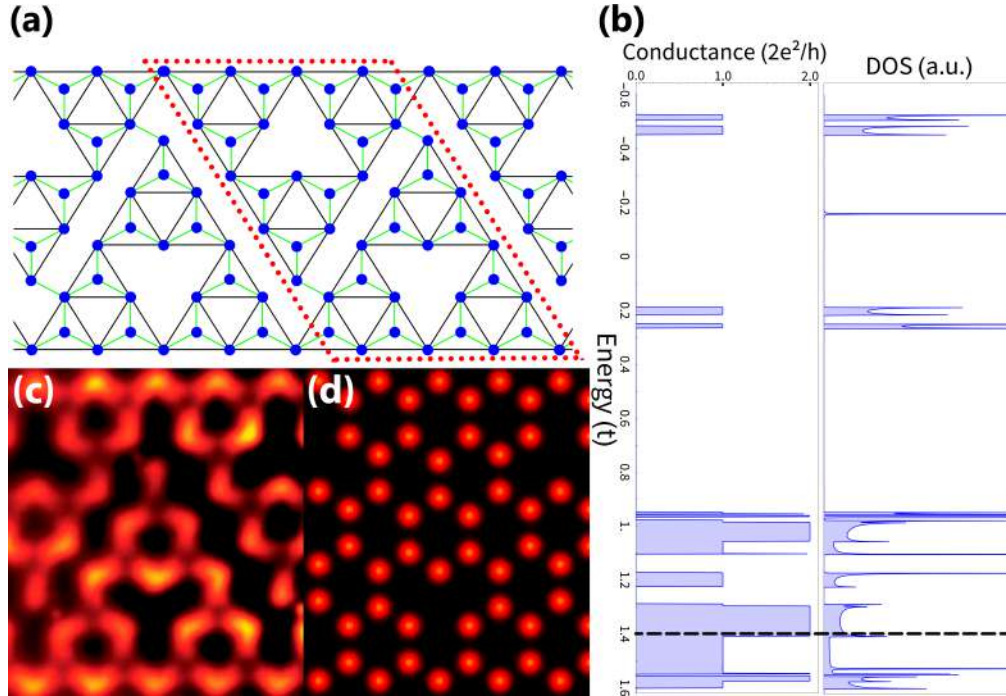
Figure 3.14: (a) Effective G(2)-dephased ST chain, (b) Conductance and DOS, (c) STM image [adapted from Ref.[45]], and (d) LDOS at E=1.4t.

To investigate fractal properties on such nanostructured systems we concentrate now in the
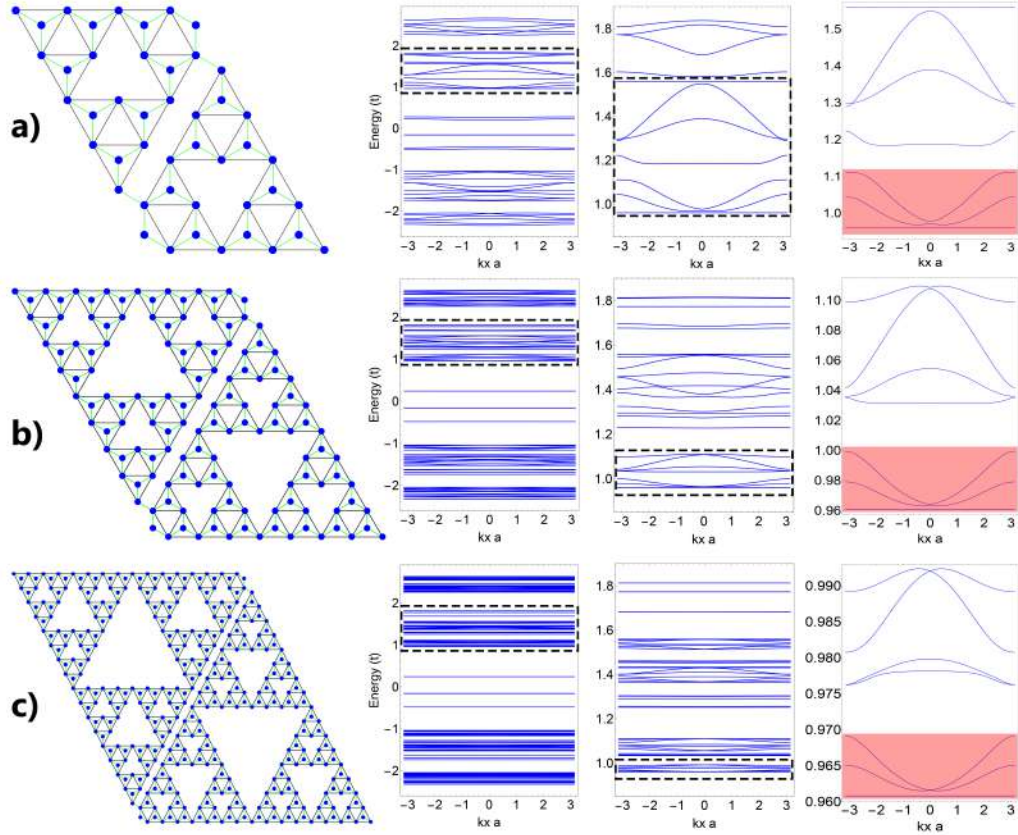
Figure 3.15: (a-c) Unit cells of G(2-4) Dephased ST Chains and corresponding band structures, followed by its zooms, from left to right.

electronic band structures. We present in Fig. 3.15(a-c) unit cells of three generations of the proposed molecular chain discussed in Fig. 3.14, G(2), G(3) and G(4), and the corresponding band structure of the 1D chains. The dashed regions marked in the band structures presented in Fig. 3.15(a), related to the G(2) lattice, was enlarged in the subsequent panels at right, revealing a single flat band and other two bands presenting a small energy dispersion, at the lower energy range, highlighted by the red shaded area. These later are also noted in the DOS and conductance results (not shown). To analyze the role played by the generation order on the used HST blocks forming the chains, we show in Fig. 3.15(b) and (c), for comparison, the energy bands of the three G(3) and G(4) dephased ST chains. The auto similarity of these systems can be evidenced looking firstly, at the same energy region of the three generation proposed, defined by the dashed energy range. Comparing the results, we notice in the last right panels that the common pattern of a single flat band (happening at 0.96t in the three cases), followed by two dispersive bands [ending

at 1.1t (a), 1.0t (b) and 0.97t (c), respectively, is slightly preserved going from G(2) to G(4). As expected, for increasing ST generations, the repeated band structure pattern are found at smaller energy ranges.

Moreover, the results for the energy bands reveal an increasing number of 1D-like van Hove singularities passing from G(2) to G(4) dephased chains. Similarly as reported before [39], the number of flat bands increases significantly with the ST order used to build the chains. Also, in these flat states the degeneracy for each k value inside the first Brillouin zone increases considerably. Our findings suggest that properly tuning the tight binding parameters and playing with different connections between and inside the unit cells, better modeling of such nanostructured systems may be achieved. In particular, considering different on-site energies for Co atoms and BPyB molecules in our model (for instance taking $E_C = -E_{Co}$), simplified here as carbon atoms, only promotes a shift in the double flat states near the fermi level.

Conclusion

We have seen that the carbon atom is a very versatile chemical component. As Mr.Feynmans quote, a new physics branch turned to be an important description of nature behavior at fractal nano scales. The understanding of multilayered systems also becomes very important due to the possibility of changing physical properties. In particular, the recent superconductivity emergence in bilayered graphene systems raised other carbon-based materials to the center of research activity. The studied electronic properties of the monolayered systems present an alternating of semiconductor to metallic families in armchair and only metallic for zigzag features in hexagonal systems with an even number of atoms in the unit cell, e.g., graphene and α-graphyne. For an odd number of atoms inside the unit cell, e.g. Kagomé Honeycomb, both armchair and zigzag nanoribbons are semiconductor with a band gap $E_g = 2\epsilon$. The kagomé systems turned to be very important due the appearance of flat bands, which results in high peaks of van Hove singularities. Stacking two monolayers we obtain the bilayered systems, here studied for each hexagonal system proposed; bilayers of graphene, α-graphyne and kagomé honeycomb. The connection between those geometries is observed when a transient flat band in both α-graphyne and kagomé is obtained by changing the tight-binding parameters. The study developed for the bilayered systems is mainly related with the graphene and α-graphyne bilayers due its similar electronic properties. In zigzag graphene bilayers, first principle calculations have shown a curved relaxed structure at zigzag edges favoring an interaction between those edge sites. Also, the edge hopping analysis were made in order to obtain the best data fitting with DFT results. Both calculations, our results and others, are in good agreement with zigzag graphene bilayer nanoribbons. However for α-graphyne bilayer nanoribbons, the zigzag results have an energy gap difference, which can be turned out by adding the electronic correlation between each layer sites. Meanwhile the calculations for armchair features are in good agreement with the literature. Better adjustment are still lacking to improve the tight binding approximations such as a proper incorporation of the ribbon bending effect due to relaxation processes. Rotating one layer above the other, we construct the twisted bilayered systems. Responsible for exhibit

superconductivity at low angles in $T \approx 2K$, the twisted bilayer graphene are systems with large commensurable unit cells giving the possibility of experimental observation of Hofstadter butterflies for effectively-low magnetic fields. These fractal figures mark the connection between standard geometry lattices with the fractal world.

We have explored fractal features in the electronic properties of ST flakes and molecular chains of different geometry details. Recent experimental results are modeled within our developed tight-binding models, as evidenced for the molecular sierpinski lattice developed in this work. Also, more recently, the synthesis of sierpinski lattice leads the exploration on physical properties of fractal lattices. Theoretical works were previously modeled several spatial geometries. The simple models developed here could qualitatively describe the experimental results for hexagonal flakes and more complex lattice. The results found for the fractal dimension of the Kagomé-like ST flakes follow recent reports on graphene-like STs. The result is corroborated by the Kagomé ST LDOS at particular energy states that exhibit typical graphene ST spatial configurations. The self similarity of the energy states are found comparing different ST generation orders and also amplifying the energy ranges investigated, for both flakes and quasi 1D systems. In particular, the results for the local density of states of the theoretical molecular chains proposed here exhibit quite similar spatial charge distribution as experimental STM reports. The analysis of transport response of such quasi 1D molecular chains reveals localized states that do not contribute to the electronic transport. The study can be used as a guide to propose a variety of architecture in the synthesis of real molecular chains.

Further aspects of the theoretical framework adopted were explored such as changing the inter and intra unit cell connections of the proposed molecular chains. Some of the schemes induce degeneracy break of particular electronic states, favoring the disrupt of flat bands. Although a primary analysis on more realistic on-site energies, simulating metallic atoms in the ST chains that appear in the experiments, has not indicated great changes, more sophisticated theoretical framework must be used for a fully study of tuning the energy channel positions in the transport features of the chains. Probably, the inclusion of electron-electron interaction in the model will bring important light into the electronic occupation in conductive states, in special, in the flat states presented.

Appendix A

Symmetries in Graphene

The symmetry of nanostructured systems, as discussed in Sub-Section 1.1.1 plays an important role in the electronic properties of each system. Therefore, here we analyze Spatial Inversion and Time-Reversal symmetry aspects in graphene when a diagonal term associated with the potentials of A and B sub-lattices is included.

Given the Hamiltonian for graphene,

$$\mathcal{H}(\vec{k}) = \begin{bmatrix} 0 & \gamma h(\vec{k}) \\ \gamma h^{\dagger}(\vec{k}) & 0 \end{bmatrix} \tag{A.1}$$

in which

$$h(\vec{k}) = \sum_{\alpha} e^{i\vec{k}.\vec{\delta}_{\alpha}} = 2e^{\frac{iak_y}{2}} cos(\frac{\sqrt{3}ak_x}{2}) + e^{-iak_y} \tag{A.2}$$

where for simplicity we have considered $\varepsilon = 0$ and first neighbors only. The Hamiltonian A.1 could be understood as a two level system in terms of the Pauli matrices $(\sigma_1, \sigma_2, \sigma_3)$.

In special, the metallic states mainly related with the Dirac cones at $k = \pm\frac{4\pi}{3\sqrt{3}a}$ in hexagonal systems as Graphene are topologically protected by Time-Reversal and Spatial Inversion symmetry. We will conclude that those symmetries are preserved if the principal diagonal terms of the matrix are real and identical. Physically for Graphene, this is quite obvious, given that its sub-lattice is

formed by Carbon atoms that are identical, and because of that the ε is a real quantity, measurable and usually given in electron-volt (eV). For this reason, the pristine Graphene does not have a term associated with σ_3 in the Hamiltonian. What we will do next is to propose an element associated with $f(\vec{k})\sigma_3$ and to analyze its correlation with the potentials ε in Graphene.

Time-Reversal Symmetry ($\mathcal{T}$): Given that the wave vector $\vec{k}$ [105] is not invariant by a transformation $\mathcal{T}$, then $\mathcal{H}(\vec{k}) \rightarrow H^*(-\vec{k})$ since the Bloch basis are related with complex phases. The Hamiltonian A.1 now is given by

$$
\mathcal{H}(\vec{k}) = \begin{bmatrix} f(\vec{k}) & \gamma h(\vec{k}) \\ \gamma h^\dagger(\vec{k}) & -f(\vec{k}) \end{bmatrix},
\tag{A.3}
$$

and as a consequence of the time-reversal operator $\mathcal{T}$, we have

$$
\mathcal{H}(-\vec{k})^* = \begin{bmatrix} f^*(-\vec{k}) & \gamma(h(-\vec{k}))^* \\ \gamma(h^\dagger(-\vec{k}))^* & -f^*(-\vec{k}) \end{bmatrix}.
\tag{A.4}
$$

As $\mathcal{H}(\vec{k}) = \mathcal{H}^*(-\vec{k})$ if the system has time-reversal symmetry conserved, then comparing term by term in A.3, $\mathcal{H}(\vec{k})_{1,1} = \mathcal{H}^*(-\vec{k})_{1,1}$ which implies that $f(\vec{k}) = f^*(-\vec{k})$ is a symmetric function in $\vec{k}$.

Spatial Symmetry Inversion ($\mathcal{P}$): Physically, in Graphene, this symmetry is responsible to invert the phases between the A and B sites, changing $\vec{k}$ to $-\vec{k}$. Thus, in Pauli matrix representation, the condition $\mathcal{P}\mathcal{H}(-\vec{k})\mathcal{P}^{-1} = \mathcal{H}(\vec{k})$ must also be satisfied. For this reason, being symmetric about $\mathcal{P}$ requires that $\sigma_i \mathcal{H}(-\vec{k})\sigma_i^{-1} = \mathcal{H}(\vec{k})$ with i=1, 2 and 3 being the x, y and z components, respectively[58].

For i=1 we have,

$$
\begin{bmatrix} 0 & 1 \\ 1 & 0 \end{bmatrix} \begin{bmatrix} 0 & \gamma h(-\vec{k}) \\ \gamma h(-\vec{k}) & 0 \end{bmatrix} \begin{bmatrix} 0 & 1 \\ 1 & 0 \end{bmatrix} = \begin{bmatrix} 0 & \gamma h(\vec{k}) \\ \gamma h(\vec{k}) & 0 \end{bmatrix}.
$$

It can be shown that for i= 2,3 the equality is not satisfied. Actually, $\sigma_2 \mathcal{H}(-\vec{k})\sigma_2 = -\mathcal{H}(\vec{k})$ and $\sigma_3 \mathcal{H}(-\vec{k})\sigma_3 = -\mathcal{H}^*(\vec{k})$. Now, including $f(\vec{k})\sigma_3$ in $\sigma_1 \mathcal{H}(-\vec{k})\sigma_1$,

$$\begin{bmatrix} 0 & 1 \\ 1 & 0 \end{bmatrix} \begin{bmatrix} f(-\vec{k}) & \gamma h(-\vec{k}) \\ \gamma h(-\vec{k}) & -f(-\vec{k}) \end{bmatrix} \begin{bmatrix} 0 & 1 \\ 1 & 0 \end{bmatrix} = \begin{bmatrix} -f(\vec{k}) & \gamma h(\vec{k}) \\ \gamma h(\vec{k}) & f(\vec{k}) \end{bmatrix},$$

and comparing the matrix elements between the two sides of the equation we get $f(-\vec{k}) = -f(\vec{k})$. In the following we want to combine both symmetries presented in Graphene and compare the conditions for $f(\vec{k})$.

Spatial & Time-Reversal Symmetries: With the inclusion of the term $f(\vec{k})\sigma_3$ in the graphene hamiltonian, for satisfying both symmetries, the following conditions for $f(\vec{k})$ are needed

$$\begin{cases} f(\vec{k}) = f^*(-\vec{k}) \\ f(-\vec{k}) = -f(\vec{k}) \end{cases} \tag{A.5}$$

Solving the system above, we have $f^*(-\vec{k}) = -f(-\vec{k})$, which implies that $f(\vec{k})$ is purely imaginary. However, as the Hamiltonian is hermitian, $f(\vec{k}) = 0$ is the unique non-trivial solution. Further, for both symmetries to be satisfied the graphene hamiltonian can not have σ_3 terms in the principal diagonal. Finally, for that reason, the parity related with $\mathcal{T}$ and $\mathcal{P}$ protects the Dirac cones in graphene and similar materials. We propose in the next the breaking of these symmetry and verify the electronic gap emergence.

Symmetry break in Graphene: Supposing that $f(\vec{k})\sigma_3 = \varepsilon\sigma_3$, which implies in a distinct potential ε between the sub-lattice sites A and B. With this change, the hamiltonian becomes

$$\mathcal{H}(\vec{k}) = \begin{bmatrix} \varepsilon & \gamma h(\vec{k}) \\ \gamma h^\dagger(\vec{k}) & -\varepsilon \end{bmatrix}. \tag{A.6}$$

The eigenvalues $E(k_x, 0)$ are displayed in Fig. A.1. We notice that the energy gap is proportional to 2ε. Therefore, we conclude that the both symmetries play an important role in the electronic structure of condensed matter systems. In fact, other hexagonal geometries that spontaneously break those symmetries like the hexagonal Boron Nitride (hBN), have naturally different values for

(a) (b) (c)
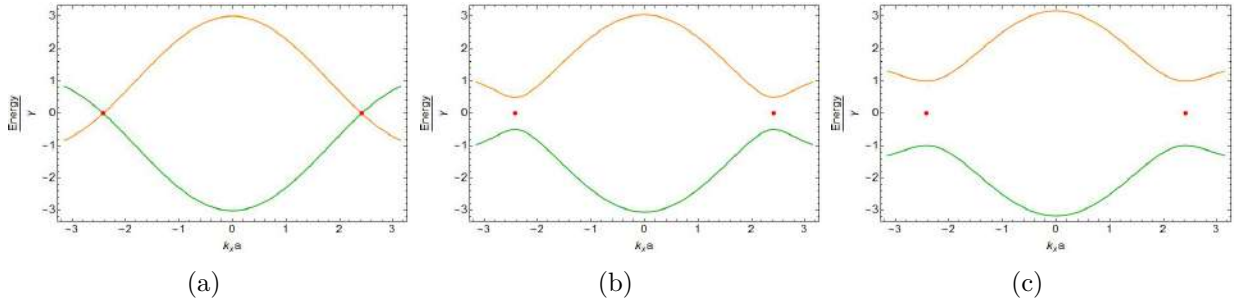
Figure A.1: Electronic dispersion relation projected along the k_x axis for different values of ε: (a) ε=0.0 eV and E_g=0.0, (b) ε=0.5 eV and E_g=1.0γ and (c) ε=1.0 eV and E_g=2.0γ. Dirac $\pm$K points are pointed in red.
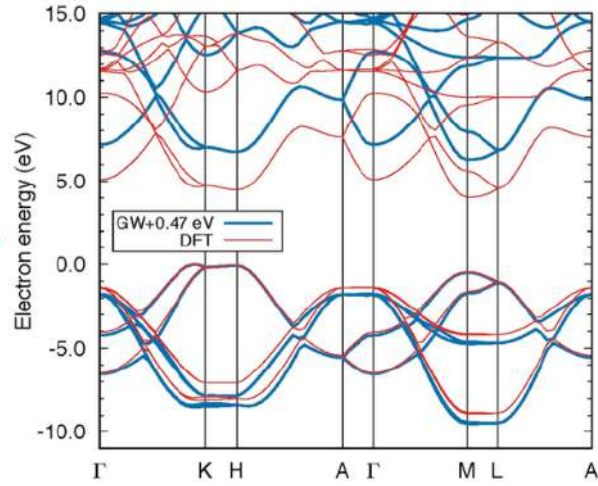
Figure A.2: hBN Band structure along the high symmetry points [106].

the on site energy in the sub-lattice. For that reason, hBN is an insulator material with an energy gap $E_g > 5$ eV [106], as depicted in Fig. A.2.

Appendix B

Dyson Equation

The Dyson equation surges naturally within the Greens function formalism when we perturb the free particle with an external potential. The Hamiltonian of this system can be expressed as

$$H(\vec{r}) = H_0(\vec{r}) + V(\vec{r}) \ . \tag{B.1}$$

The Green function associated with H is given by

$$[E - H(\vec{r})]G(\vec{r}, \vec{r}\,') = \delta(\vec{r} - \vec{r}\,') \tag{B.2}$$

or

$$\overbrace{[E - H_0(\vec{r})]}^{\mathcal{L}} \overbrace{G(\vec{r}, \vec{r}\,')}^{\psi(\vec{r})} = \overbrace{\delta(\vec{r} - \vec{r}\,') + V(\vec{r})G(\vec{r}, \vec{r})}^{f(\vec{r})} \ . \tag{B.3}$$

Changing the integral argument of Eq. 1.17 to $g(\vec{r}, \vec{r}\,'')$ for the undisturbed system, we have

$$G(\vec{r}, \vec{r}\,') = \int d\vec{r}\,'' g(\vec{r}, \vec{r}\,'')[\delta(\vec{r}\,'' - \vec{r}\,') + V(\vec{r}\,'')G(\vec{r}\,'', \vec{r}\,')]$$
$$= g(\vec{r}, \vec{r}\,') + \int d\vec{r}\,'' g(\vec{r}, \vec{r}\,'')V(\vec{r}\,'')G(\vec{r}\,'', \vec{r}\,') \ . \tag{B.4}$$

Note that $G(\vec{r}, \vec{r}\,')$ now depends on the integral of $G(\vec{r}\,'', \vec{r})$, however, we can calculate this one

in the same way as we calculated before,

$$G(\vec{r}\,'',\vec{r}\,') = g(\vec{r}\,'',\vec{r}\,') + \int d\vec{r}\,'''g(\vec{r}\,'',\vec{r}\,''')V(\vec{r}\,''')G(\vec{r}\,''',\vec{r}\,') \ , \tag{B.5}$$

which substituting in $G(\vec{r},\vec{r}\,')$ we get,

$$G(\vec{r},\vec{r}\,') = g(\vec{r},\vec{r}\,')$$
$$+ \int d\vec{r}\,''g(\vec{r},\vec{r}\,'')V(\vec{r}\,'')\Big[g(\vec{r}\,'',\vec{r}\,') + \int d\vec{r}\,'''g(\vec{r}\,'',\vec{r}\,''')V(\vec{r}\,''')G(\vec{r}\,''',\vec{r}\,')\Big]$$

$$= g(\vec{r},\vec{r}\,') + \int d\vec{r}\,''g(\vec{r},\vec{r}\,'')V(\vec{r}\,'')g(\vec{r}\,'',\vec{r}\,')$$
$$+ \int d\vec{r}\,'' \int d\vec{r}\,'''d\vec{r}\,''g(\vec{r},\vec{r}\,'')V(\vec{r}\,'')g(\vec{r}\,'',\vec{r}\,''')V(\vec{r}\,''')G(\vec{r}\,''',\vec{r}\,')$$

with

$$G(\vec{r}\,''',\vec{r}\,') = g(\vec{r}\,''',\vec{r}\,') + \int d\vec{r}\,^{IV}g(\vec{r}\,''',\vec{r}\,^{IV})V(\vec{r}\,^{IV})G(\vec{r}\,^{IV},\vec{r}\,')$$

then

$$G(\vec{r},\vec{r}\,') = g(\vec{r},\vec{r}\,') + \int d\vec{r}\,''g(\vec{r},\vec{r}\,'')V(\vec{r}\,'')g(\vec{r}\,'',\vec{r}\,')$$
$$+ \int d\vec{r}\,'' \int d\vec{r}\,'''d\vec{r}\,''g(\vec{r},\vec{r}\,'')V(\vec{r}\,'')g(\vec{r}\,'',\vec{r}\,''')V(\vec{r}\,''')g(\vec{r}\,''',\vec{r}\,') + \ldots \tag{B.6}$$

We can see that the new Green's function is written again in terms of another function to be determined. We solve this problem by an iterative method in which, for simplicity, we write the terms in the integral of Eq.B.6 in the form of operators.

Thus, we have for the first term

$$\int d\vec{r}\,''g(\vec{r},\vec{r}\,'')V(\vec{r}\,'')g(\vec{r}\,'',\vec{r}\,') = \sum_{\vec{r}\,'',\vec{r}\,'''} \langle\vec{r}|\mathbf{g}|\vec{r}\,''\rangle\,\langle\vec{r}\,''|\mathbf{V}|\vec{r}\,'''\rangle\,\langle\vec{r}\,'''|\mathbf{g}|\vec{r}\,'\rangle$$
$$= \langle\vec{r}|\mathbf{g}\mathbf{V}\mathbf{g}|\vec{r}\,'\rangle \ , \tag{B.7}$$

79

and for the second

$$\int d\vec{r}\,'' \int d\vec{r}\,'''d\vec{r}\,''g(\vec{r},\vec{r}\,'')V(\vec{r}\,'')g(\vec{r}\,'',\vec{r}\,''')V(\vec{r}\,''')g(\vec{r}\,''',\vec{r}\,')$$

$$= \sum_{\vec{r}\,^{II},\vec{r}\,^{IV}} \sum_{\vec{r}\,^{III},\vec{r}\,^{V}} \left\langle \vec{r}\left|\mathbf{g}\right|\vec{r}\,^{II}\right\rangle \left\langle \vec{r}\,^{II}\left|\mathbf{V}\right|\vec{r}\,^{III}\right\rangle \left\langle \vec{r}\,^{III}\left|\mathbf{g}\right|\vec{r}\,^{IV}\right\rangle \left\langle \vec{r}\,^{IV}\left|\mathbf{V}\right|\vec{r}\,^{V}\right\rangle \left\langle \vec{r}\,^{V}\left|\mathbf{g}\right|\vec{r}\,^{I}\right\rangle$$

$$= \left\langle \vec{r}\left|\mathbf{gVgVg}\right|\vec{r}\,'\right\rangle \ . \quad (\text{B.8})$$

The complete expansion of $G(\vec{r},\vec{r}\,')$ can be expressed in the form of operators as

$$\mathbf{G} = \mathbf{g} + \mathbf{gVg} + \mathbf{gVgVg} + \mathbf{gVgVgVg} + \dots$$

$$= \mathbf{g} + \mathbf{gV}\underbrace{\mathbf{g} + \mathbf{gVgVg} + \mathbf{gVgVgVg} + \dots}_{\mathbf{G} \text{ Propagator}} \ . \quad (\text{B.9})$$

Finally, the Dyson equation is written as

$$\mathbf{G} = \mathbf{g} + \mathbf{gVG}. \quad (\text{B.10})$$

Appendix C

Decimation Method Application:

Brick Wall α-Graphyne

Here we follow Ref.[107], and consider that the graphyne lattice can be represented as a graphene with renormalized hopping energies, i.e., $(t_1, t_2) \to \gamma_0$ [11]. We can slice the unit cell and deform the lattice as a square lattice, as illustrated in Fig. C.1.
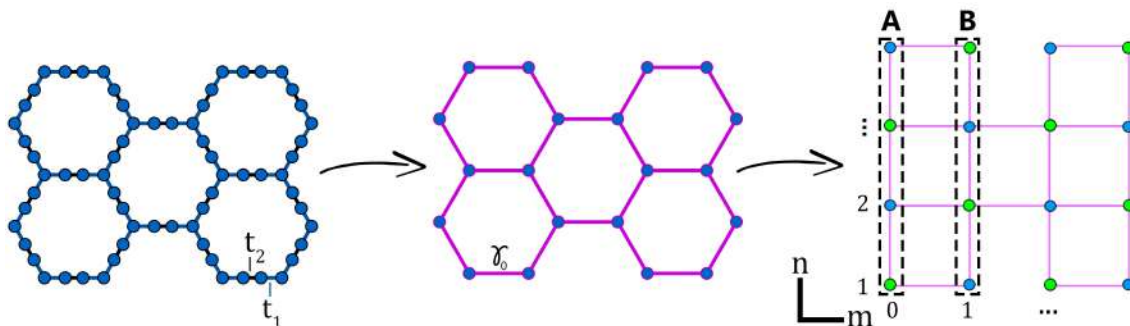
Figure C.1: Illustration of the renormalization process and the construction of the brick wall in an armchair α-graphyne. Where the sub-lattice difference is expressed as blue and green circles in the last picture.

This system is constituted by an infinite number of alternated slices of type A and B, both formed by n numbers of atoms. The connection between slices $A(B)$ and the slice $B(A)$ are represented by

an operator $U_{AB(BA)}$ from left to right, and $U^\dagger_{AB(BA)}$ from right to left. We define the Hamiltonian

$$H^{m,m'}(n,n') = \begin{pmatrix} H_A(n,n') & U_{AB}(n,n') & 0 & 0 & \dots \\ U^\dagger_{AB}(n,n') & H_B(n,n') & U_{BA}(n,n') & 0 & 0 \\ 0 & U^\dagger_{BA}(n,n') & H_A(n,n') & U_{AB}(n,n') & 0 \\ 0 & 0 & U^\dagger_{AB}(n,n') & H_B(n,n') & U_{BA}(n,n') \\ \vdots & 0 & 0 & U^\dagger_{BA}(n,n') & \ddots \end{pmatrix} \quad \text{(C.1)}$$

Taking into account the relation

$$[(E(n,n') - H(n,n'))G(n,n')]^{m,m'} = \delta^{m,m'}(n,n') \quad \text{(C.2)}$$

we have

$$[E^{0,0} - H_A]G_{0,0} = \mathcal{I} + U_{AB}G_{10}$$

$$[E^{1,1} - H_B]G_{1,0} = U^\dagger_{AB}G_{1,0} + U_{BA}G_{2,0}$$

$$[E^{2,2} - H_A]G_{2,0} = U^\dagger_{BA}G_{2,0} + U_{AB}G_{3,0}$$

$$\vdots$$

$$[E^{k,k} - H_i]G_{k,0} = U^\dagger_{j,i}G_{k-1,0} + U_{i,j}G_{k+1,0} \quad \text{(C.3)}$$

where $\mathcal{I}$ is the identity matrix. The Hamiltonian of the i-th slice is labeled as $H_i(n,n')$ and for k even(odd) we have i=A(B). For simplicity we consider $E^{0,0} = E^{1,1} = \dots = E$.

The first decimation step for the B slice gives,

$$[E - H_A - b_1]G_{0,0} = \mathcal{I} + d_1G_{2,0}$$

$$[E - H_A - a_1 - b_1]G_{2,0} = c_1G_{0,0} + d_1G_{4,0}$$

$$[E - H_A - a_1 - b_1]G_{4,0} = c_1G_{2,0} + d_1G_{6,0}$$

$$\vdots$$

$$[E - H_A - a_1 - b_1]G_{2k,0} = c_1G_{2(k-1),0} + d_1G_{2(k+1),0} \quad \text{(C.4)}$$

82

with

$$a_1 = U_{BA}^\dagger (E - H_B)^{-1} U_{BA} \quad , \qquad b_1 = U_{AB}(E - H_B)^{-1} U_{AB}^\dagger$$

$$c_1 = U_{BA}^\dagger (E - H_B)^{-1} U_{AB}^\dagger \quad , \qquad d_1 = U_{AB}(E - H_B)^{-1} U_{BA} \qquad \text{(C.5)}$$

Similarly, we perform the second decimation step, and obtain

$$[E - H_A - b_1 + d_2]G_{0,0} = \mathcal{I} + b_2 G_{4,0}$$

$$[E - H_A - a_1 - b_1 - c_2]G_{4,0} = a_2 G_{0,0} + b_2 G_{8,0}$$

$$[E - H_A - a_1 - b_1 - c_2]G_{8,0} = a_2 G_{4,0} + b_2 G_{12,0}$$

$$\vdots$$

$$[E - H_A - a_1 - b_1 - c_2]G_{2^2 k,0} = a_2 G_{2^2(k-1),0} + b_2 G_{2^2(k+1),0} \qquad \text{(C.6)}$$

where

$$a_2 = c_1(E - H_A - a_1 - b_1)^{-1}c_1 \ ,$$

$$b_2 = d_1(E - H_A - a_1 - b_1)^{-1}d_1 \ ,$$

$$c_2 = c_1(E - H_A - a_1 - b_1)^{-1}d_1 + d_1(E - H_A - a_1 - b_1)^{-1}c_1 \ ,$$

$$d_2 = d_1(E - H_A - a_1 - b_1)^{-1}c_1 \ . \qquad \text{(C.7)}$$

The third step leads to

$$[E - H_A - b_1 - d_3]G_{0,0} = \mathcal{I} + b_3 G_{8,0}$$

$$[E - H_A - a_1 - b_1 - c_3]G_{8,0} = a_3 G_{0,0} + b_3 G_{16,0}$$

$$[E - H_A - a_1 - b_1 - c_3]G_{16,0} = a_3 G_{8,0} + b_3 G_{24,0}$$

$$\vdots$$

$$[E - H_A - a_1 - b_1 - c_3]G_{2^3(k-1),0} = a_3 G_{2^3(k+1),0}, \qquad \text{(C.8)}$$

with

$$a_3 = a_2(E - H_A - a_1 - b_1 - c_2)^{-1}a_2 \ ,$$

$$b_3 = b_2(E - H_A - a_1 - b_1 - c_2)^{-1}b_2 \ ,$$

$$c_3 = c_2 + a_2(E - H_A - a_1 - b_1 - c_2)^{-1}b_2 + b_2(E - H_A - a_1 - b_1 - c_2)^{-1}a_2 \ ,$$

$$d_3 = d2 + b_2(E - H_A - c_2)^{-1}a_2 \ . \tag{C.9}$$

Therefore, we can write a general expression for the S-th decimation step

$$[E - H_A - b_1 - d_S]G_{0,0} = \mathcal{I} + b_S G_{2^S k,0} \ ,$$

$$[E - H_A - a_1 - b_1 - c_S]G_{2^S k,0} = a_S G_{2^S(k-1),0} + b_S G_{2^S(k+1),0} \ . \tag{C.10}$$

where

$$a_S = a_{S-1}(E - H_A - a_1 - b_1 - c_{S-1})^{-1}a_{S-1} \ ,$$

$$b_S = b_{S-1}(E - H_A - a_1 - b_1 - c_{S-1})^{-1}b_{S-1} \ ,$$

$$c_S = c_{S-1} + a_{S-1}(E - H_A - a_1 - b_1 - c_{S-1})^{-1}b_{S-1}$$

$$+ \ b_{S-1}(E - H_A - a_1 - b_1 - c_{S-1})^{-1}a_{S-1} \ ,$$

$$d_S = d_{S-1} + b_{S-1}(E - H_A - a_1 - b_1 - c_{S-1})^{-1}a_{S-1} \tag{C.11}$$

and we define $c_1 = d_1 = 0$. When $|b_S|$ is sufficiently small we can approximate $G^{0,0} \approx [E - H_A - b_1 - d_S]^{-1}$. This result provides the surface Green function of each slide slice. Notice that for armchair case the Hamiltonian from the slice A is equal to the slice B: $H_A = H_B$. So we define

$$U_{AB}(n,n') = \begin{pmatrix} \gamma_0 & 0 & 0 & 0 & \dots \\ 0 & 0 & 0 & 0 \\ 0 & 0 & \gamma_0 & 0 \\ 0 & 0 & 0 & 0 \\ \vdots & & & & \ddots \end{pmatrix} \ , \quad U_{BA}(n,n') = \begin{pmatrix} 0 & 0 & 0 & 0 & \dots \\ 0 & \gamma_0 & 0 & 0 \\ 0 & 0 & 0 & 0 \\ 0 & 0 & 0 & \gamma_0 \\ \vdots & & & & \ddots \end{pmatrix} \tag{C.12}$$

$$H_A(n, n') = \begin{pmatrix} \varepsilon_0 & \gamma_0 & 0 & 0 & \dots \\ \gamma_0 & \varepsilon_0 & \gamma_0 & 0 & \\ 0 & \gamma_0 & \varepsilon_0 & \gamma_0 & \\ 0 & 0 & \gamma_0 & \varepsilon_0 & \\ \vdots & & & & \ddots \end{pmatrix} \tag{C.13}$$

To illustrate the presented decimation process, we show in Fig. C.2 the electronic density of states obtained by using Eq.(1.2) for an infinite armchair nanoribbon with $N_A = 30$.
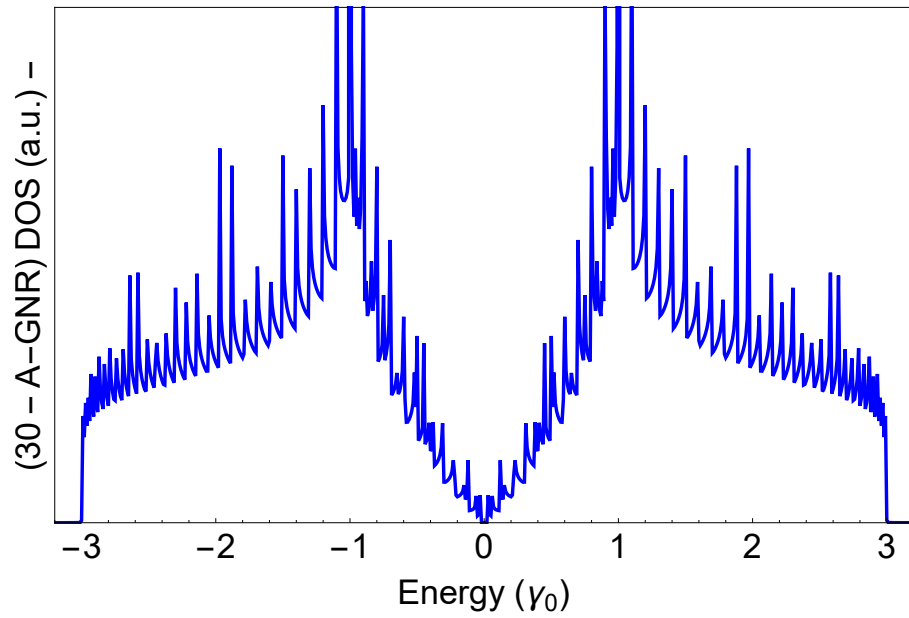
Figure C.2: Total density of states for $S = 40$, $\eta = 10^{-4}$ and nanoribbon size $N_A = 30$.

Appendix D

Epigraph Source Code

```
In[∘]:= next[prev_] :=
    prev /. Polygon[{p1_, p2_, p3_}] :↦
            polígono
        {Polygon[{p1, (p1 + p2) / 2, (p1 + p3) / 2}], Polygon[{p2, (p2 + p3) / 2, (p1 + p2) / 2}],
         polígono                                    polígono
         Polygon[{p3, (p1 + p3) / 2, (p2 + p3) / 2}]};
         polígono


    transform[p_] := (Reverse[p].p) p / Norm[p]^2;
                     inverte ordem      norma


    notFishieAwwwSadFace[n_, a1_ : 0, a2_ : 0, options___] :=
      Module[{axiom}, axiom = Polygon[{Cos[#], Sin[#]} & /@ (a1 + 2 Pi Range[3] / 3)];
      módulo de código        polígono   cosseno  seno              ⋯  intervalo de valores
        Graphics[{Transparent, EdgeForm[Black],
        representa⋯  transparente   forma da ⋯  preto
          Rotate[Nest[next, N@axiom, n] /. Polygon[pts_] :↦ Polygon[transform /@ pts], a2]},
          rotação  repete a apl⋯ valor numérico   polígono           polígono
        options]];


    notFishieAwwwSadFace[7, 1.045]
```

Figure D.1: Credits: http://www.oftenpaper.net/sierpinski

References

[1] A. K. Geim and K. S. Novoselov, "The rise of graphene," *Nature Materials*, vol. 6, p. 183–191, 2007.

[2] K. Wakabayashi, K. ichi Sasaki, T. Nakanishi, and T. Enoki, "Electronic states of graphene nanoribbons and analytical solutions," *Science and Technology of Advanced Materials*, vol. 11, no. 5, 2010.

[3] K. S. Novoselov, A. K. Geim, S. V. Moronov, D. Jiangy, Y. Zhangs, S. V. Dobonosi, V. Grigorieva, and A. A. Firsov, "Electric field effect in atomically thin carbon films," *Science*, vol. 6, p. 666–669, 2004.

[4] A. Hirsch, "The era of carbon allotropes," *Nat. Mat.*, vol. 9, p. 868–871, 2010.

[5] A. H. Castro Neto, F. Guinea, N. M. R. Peres, K. S. Novoselov, and A. K. Geim, "The electronic properties of graphene," *Rev. Mod. Phys.*, vol. 81, pp. 109–162, Jan 2009.

[6] P. H. Jacobse, R. D. McCurdy, J. Jiang, G. V. Daniel J. Rizzo, P. Butler, R. Zuzak, S. G. Louie, F. R. Fischer, and M. F. Crommie*, "Bottom-up assembly of nanoporous graphene with emergent electronic states," *J. Am. Chem. Soc.*, vol. 142, no. 31, p. 13507–13514, 2020.

[7] V. S. Chandel, G. Wang, and M. Talha, "Advances in modelling and analysis of nano structures: a review," *Nanotechnology Reviews*, vol. 9, no. 1, pp. 230–258, 2020.

[8] M. Mekata, "Kagome: The story of the basketweave lattice," *Physics Today*, vol. 56, 2012.

[9] O. J. Silveira, S. S. Alexandre, and H. Chacham, "Electron states of 2d metalorganic and covalentorganic honeycomb frameworks: Ab initio results and a general fitting hamiltonian," *J. Phys. Chem. C*, vol. 120, p. 19796, 2016.

[10] H.-J. Lee, M. Lee, K. Lee, J. Jo, H. Y. andYungyeom Kim, S. C. Chae, U. Waghmare, and J. H. Lee, "Scale-free ferroelectricity induced by flat phonon bands in hfo2," *Science*, vol. 369, pp. (1343–1347), 2021.

[11] Z. Liu, G. Yu, H. Yao1, L. Liu, L. Jiang1, and Y. Zheng, "A simple tight-binding model for typical graphyne structures," *Journal of Computational Electronics volume*, vol. 14, no. 113007, 2012.

[12] R. H. Baughman, H. Eckhardt, and M. Kertesz, "Structure-property predictions for new planar forms of carbon: Layered phases containing sp2 and sp atoms," *J. Chem. Phys.*, vol. 87, p. 6687, 1987.

[13] N. Narita, S. Nagai, S. Suzuki, and K. Nakao., "Optimized geometries and electronic structures of graphyne and its family," *Phys. Rev. B*, vol. 58, p. 11009–11014, 2014.

[14] J. M. Kehoe, J. H. Kiley, J. J. English, C. A. Johnson, R. C. Petersen, and M. M. Haley, "Carbon networks based on dehydrobenzoannulenes. synthesis of graphyne substructures," *Org. Lett.*, vol. 7, pp. 969–972, 2000.

[15] M. M. Haley., "Synthesis and properties of annulenic subunits of graphyne and graphdiyne nanoarchitectures," *Pure Appl. Chem.*, vol. 80, p. 519, 2008.

[16] C. A. Johnson, Y. Lu, and M. M. Haley., "Carbon networks based on benzocyclynes. synthesis of graphyne substructures via directed alkyne metathesis.," *Org. Lett.*, vol. 9, p. 3725, 2007.

[17] X. Gao, H. Liu, D. Wang, and J. Zhang., "Graphdiyne: synthesis, properties, and applications," *Chemical Society Reviews*, vol. 48, pp. 908–936, 2019.

[18] X. N. Niu, D. Z. Yang, M. S. Si, and D. S. Xue, "Energy gaps in α-graphdiyne nanoribbons," *Journal of Applied Physics*, vol. 115, p. 143706, 2014.

[19] B. Yang, H. Zhou, X. Zhang, X. Liu, and M. Zhao., "Dirac cones and highly anisotropic electronic structure of super-graphyne," *Carbon*, vol. 113, 2017.

[20] A. N. Enyashin, Y. N. Makurin, and A. L. Ivanovskii, "Structure and electronic characteristics of new graphyne-like fullerenes of boron nitride: Quantum-chemical modelling," *Theor. Experim. Chem.40*, vol. 71, 2004.

[21] H. Y. Z. et al, "High mobility and high storage capacity of lithium in sp-sp2 hybridized carbon network: The case of graphyne.," *J. Chem. Phys.*, vol. 115, pp. 8845–8850, 2011.

[22] M. Xue, H. Qiu, and W. Guo., "Exceptionally fast water desalination at complete salt rejection by pristine graphyne monolayers," *J. Chem. Phys.*, vol. 24, 2013.

[23] J. Kang, Z. Wei, and J. Li., "Graphyne and its family: Recent theoretical advances," *ACS Appl. Mater.*, vol. 11, pp. 2692–2706, 2019.

[24] M. P. Lima, A. Fazzio, and A. J. R. da Silva, "Edge effects in bilayer graphene nanoribbons: Ab initio total-energy density functional theory calculations," *Phys. Rev. B*, vol. 79, p. 153401, Apr 2009.

[25] A. B. Kuzmenko, I. Crassee, D. van der Marel, P. Blake, and K. S. Novoselov, "Determination of the gate-tunable band gap and tight-binding parameters in bilayer graphene using infrared spectroscopy," *Phys. Rev. B*, vol. 80, p. 165406, Oct 2009.

[26] E. V. Castro, K. S. Novoselov, S. V. Morozov, N. M. R. Peres, J. M. B. L. dos Santos, J. Nilsson, F. Guinea, A. K. Geim, and A. H. C. Neto, "Biased bilayer graphene: Semiconductor with a gap tunable by the electric field effect," *Phys. Rev. Lett.*, vol. 99, p. 216802, Nov 2007.

[27] Y. Huang, X. Li, H. Cui, and Z. Zhou, "Bi-layer graphene: Structure, properties, preparation and prospects," *Current Graphene Science*, vol. 2, pp. 97 – 105, 2018.

[28] Y. Cao, V. Fatemi, S. Fang, K. Watanabe, T. Taniguchi, E. Kaxiras, and P. Jarillo-Herrero, "Unconventional superconductivity in magic-angle graphene superlattices," *Nature*, vol. 556, p. 43–50, 2018.

[29] Y. Cao, V. Fatemi, S. Fang, K. Watanabe, T. Taniguchi, E. Kaxiras, and P. Jarillo-Herrero, "Unconventional superconductivity discovered in graphene bilayers.," *Nature*, vol. 556, p. 43–50, 2018.

[30] Y. Choi, J. Kemmer, and Y. e. a. Peng, "Electronic correlations in twisted bilayer graphene near the magic angle," *Nat. Phys.*, vol. 15, p. 1174–1180, 2019.

[31] A. C. Gadelha, D. A. A. Ohlberg, C. Rabelo, E. G. S. Neto, T. L. Vasconcelos, J. L. Campos, J. S. Lemos, V. Ornelas, D. Miranda, R. Nadas, F. C. Santana, K. Watanabe, T. Taniguchi, B. van Troeye, M. Lamparski, V. Meunier, V.-H. Nguyen, D. Paszko, J.-C. Charlier, L. C. Campos, L. G. Cançado, G. Medeiros-Ribeiro, and A. Jorio, "Localization of lattice dynamics in low-angle twisted bilayer graphene," *Nature*, vol. 6, p. 183–191, 2007.

[32] Y. Cao, J. Y. Luo, V. Fatemi, S. Fang, J. D. Sanchez-Yamagishi, K. Watanabe, T. Taniguchi, E. Kaxiras, and P. Jarillo-Herrero, "Superlattice-induced insulating states and valley-protected orbits in twisted bilayer graphene," *Phys. Rev. Lett.*, vol. 117, p. 116804, Sep 2016.

[33] D. A. A. Ohlberg, D. Tami, A. C. Gadelha, E. G. S. Neto, F. C. Santana, D. Miranda, W. Avelino, K. Watanabe, T. Taniguchi, L. C. Campos, J. C. Ramirez, C. G. do Rego, A. Jorio, and G. Medeiros-Ribeiro, "The limits of near field immersion microwave microscopy evaluated by imaging bilayer graphene moiré patterns," *Nature Communications*, vol. 12, no. 2980, 2021.

[34] S. N. Kempkes, M. R. Slot, S. E. Freeney, S. J. M. Zevenhuizen, D. Vanmaekelbergh, I. Swart, and C. M. Smith, "Design and characterization of electrons in a fractal geometry," *Nat. Phys.*, vol. 15, p. 127–131, November 2019.

[35] K. Foroutan-pour, P. Dutilleul, and D. Smith, "Advances in the implementation of the box-counting method of fractal dimension estimation," *Applied Mathematics and Computation*, vol. 105, no. 2, pp. 195–210, 1999.

[36] K. V., "Measuring fractal dimension of natural object from digital images," *Measuring Fractal Dimension of Natural Object from Digital Images, Mathematica Stack Exchange*, 2012.

[37] E. Mahieu, "Box-counting the dimension of coastlines," *Wolfram Demonstrations Project*, 2014.

[38] T. Pedersen, "graphene fractals:energy gap end spin polarization," *Phys. Rev. B*, vol. 101, no. 235427, p. 1–7, 2002.

[39] B. Pal and K. Saha, "Flat bands in fractal-like geometry," *Phys. Rev. B*, vol. 97, p. 195101, May 2018.

[40] A. Nandy, B. Pal, and A. Chakrabarti, "Flat band analogues and flux driven extended electronic states in a class of geometrically frustrated fractal networks," *Journal of Physics: Condensed Matter*, vol. 27, p. 125501, mar 2015.

[41] A. N. Jabbar, "Studying the effect of building block shape on sierpinski tetrahedron fractal antenna behavior using fdtd-equivalent electric circuits," *J. Microw. Optoelectron. Electromagn. Appl.*, vol. 1, June 2012.

[42] Y. Zeng*, B. J. Y. Zhang, J. Feng, J. Luo, and M. Wang, "A fractal model for effective thermal conductivity in complex geothermal media," *Front. Earth Sci.*, March 2022.

[43] A. Nandy and A. Chakrabarti, "Engineering slow light and mode crossover in a fractal-kagome waveguide network," *Phys. Rev. A*, vol. 93, p. 013807, January 2016.

[44] X.-Y. Xu, X.-W. Wang, D.-Y. Chen, C. M. Smith, and X.-M. Jin, "Quantum transport in fractal networks," *Nature Photonics*, vol. 15, pp. 1749–4893, 2021.

[45] X. Zhang, G. Gu, N. Li, H. Wang, H. Tang, Y. Zhang, S. Hou, and Y. Wang, "One-dimensional molecular chains formed by sierpiński triangles on au(111)," *RSC Adv.*, vol. 8, p. 1852, 2018.

[46] N. Li, G. Gu, X. Zhang, D. Song, Y. Zhang, B. K. Teo, L.-m. Peng, S. Hou, and Y. Wang, "Packing fractal sierpiński triangles into one-dimensional crystals via a templating method," *Chem. Commun.*, vol. 53, pp. 3469–3472, 2017.

[47] B. Pal and A. Chakrabartia, "Nature of electron states and magneto-transport in a graphene geometry with a fractal distribution of holes," *Eur. Phys. Journ. B*, vol. 85, no. 307, 2012.

[48] Z. Jiang, D. Liu, M. Chen, J. Wang, H. Zhao, Y. Li, Z. Zhang, T. Xie, F. Wang, X. Li, G. R. Newkome, and P. Wang, "Assembling shape-persistent high-order sierpiński triangular fractals," *Science*, vol. 23, no. 5, p. 101064, 2020.

[49] A. Rastgoo-Lahrood, N. Martsinovich, M. Lischka, J. Eichhorn, P. Szabelski, D. Nieckarz, T. Strunskus, K. Das, M. Schmittel, W. M. Heckl, and M. Lackinger, "From au–thiolate chains to thioether sierpiński triangles: The versatile surface chemistry of 1,3,5-tris(4-mercaptophenyl)benzene on au(111)," *ACS Nano*, vol. 10, no. 12, p. 12, 2016.

[50] S. Jian, W. Yongfeng, C. Min, D. Jingxin, Z. Xiong, K. Julian, H. Gerhard, S. Xiang, G. J. Michael, and W. Kai, "Assembling molecular sierpiński triangle fractals," *Nature Chemistry*, vol. 7, pp. 389–393, 2015.

[51] N. Li, G. Gu, X. Zhang, D. Song, Y. Zhang, B. K. Teo, L.-M. Peng, S. Hou, and Y. Wang, "Packing fractal sierpiński triangles into one-dimensional crystals via a templating method," *Chem. Commun.*, vol. 53, pp. 3469–3472, 2017.

[52] N. Li, X. Zhang, G.-C. Gu, H. Wang, D. Nieckarz, P. Szabelski, Y. He, Y. Wang, J.-T. Lü, H. Tang, L.-M. Peng, S.-M. Hou, K. Wu, and Y.-F. Wang, "Sierpiński-triangle fractal crystals with the c3v point group," *Chinese Chemical Letters*, vol. 26, no. 10, pp. 1198–1202, 2015.

[53] N. Li, G. Gu, X. Zhang, D. Song, Y. Zhang, B. K. Teo, L.-M. Peng, S. Hou, and Y. Wang, "Packing fractal sierpiński triangles into one-dimensional crystals via a templating method," *Chem. Commun.*, vol. 53, pp. 3469–3472, 2017.

[54] Y. Zhang, X. Zhang, Y. Li, S. Zhao, S. Hou, K. Wu, and Y. Wang, "Packing sierpinski triangles into two-dimensional crystals," *J. Am. Chem. Soc.*, vol. 142, pp. 17928–17932, 2020.

[55] M. Miscuglio, X. M. Yaliang Gui, Z. Ma, S. Sun, T. E. Ghazawi, T. Itoh, A. Alù, and V. J. Sorger, "Approximate analog computing with metatronic circuits," *Communications Physics*, vol. 4, no. 196, 2021.

[56] M. D. R. Saito, G. Dresslhaus, *Physical Properties of Carbon Nanotubes.* 1. ed. London: Imperial College Press, 1998.

[57] "How to understand the time-reversal symmetry in graphene?." <https://mattermodeling.stackexchange.com/a/1602/3560>. Posted: Jul 21, 2020.

[58] J. Cayssol, "Various probes of dirac matter: from graphene to topological insulators," *arXiv: Mesoscale and Nanoscale Physics*, 2013.

[59] F. Guinea, M. I. Katsnelson, and A. K. Geim, "Energy gaps and a zero-field quantum hall effect in graphene by strain engineering," *Nature Physics*, vol. 6, p. 30–33, 2010.

[60] N. S. Bandeira, D. R. da Costa2, A. Chaves, G. A. Farias1, and R. N. C. Filho, "Gap opening in graphene nanoribbons by application of simple shear strain and in-plane electric field," *J. Phys.: Condens. Matte*, vol. 33, no. 6, 2020.

[61] J.-W. Rhim, K. Kim, and B.-J. Yang, "Quantum distance and anomalous landau levels of flat bands," *Nature*, vol. 584, pp. 59–63, 2020.

[62] T. M. R. Wolf, J. L. Lado, G. Blatter, and O. Zilberberg, "Electrically tunable flat bands and magnetism in twisted bilayer graphene," *Phys. Rev. Lett.*, vol. 123, p. 096802, Aug 2019.

[63] Z. L. et al, "Realization of flat band with possible nontrivial topology in electronic kagome lattice," *SCIENCE ADVANCES*, vol. 369, 2018.

[64] M. M. Odashima, B. G. Prado, and E. Vernek, "Pedagogical introduction to equilibrium green's functions: condensed-matter examples with numerical implementations," *Rev. Bras. Ensino Fís.*, vol. 39, no. 1, p. 448, 2017.

[65] E. N. Economou, *Green's Functions in Quantum Physics*. Springer Series in Solid-State Sciences, 1979.

[66] E. H. Huisman, F. L. Bakker, J. P. van der Pal, R. M. de Jonge, and C. H. van der Wal, "Public exhibit for demonstrating the quantum of electrical conductance," *American Journal of Physics*, vol. 79, p. 856, 2011.

[67] B. J. van Wees, H. van Houten, C. W. J. Beenakker, J. G. Williamson, L. P. Kouwenhoven, D. van der Marel, and C. T., "Quantized conductance of point contacts in a two-dimensional electron gas," *Phys. Rev. Lett.*, vol. 60, p. 848, 1988.

[68] S. Datta, *In Electronic Transport in Mesoscopic Systems.* Cambridge, 1995.

[69] D. A. Ryndyk, *Theory of Quantum Transport at Nanoscale.* Springer Series in Solid-State Sciences, 2016.

[70] H. R. G. Binning, C. Gerber, and E. Weibel, "Surface studies by scanning tunneling microscopy," *Phys.Rev.Lett.*, vol. 49, no. 57, p. 183–191, 1982.

[71] C. J. Chen, "Origin of atomic resolution on metal surfaces in scanning tunneling microscopy," *Phys. Rev. Lett.*, vol. 65, p. 448, 1990.

[72] J. Tersoff and D. R. Hamann, "Theory of the scanning tunneling microscope," *Phys. Rev. B*, vol. 31, no. 805, p. 183–191, 1985.

[73] J. Ou-Yang, B. Källebring, and R. A. Marcus, "A theoretical model of scanning tunneling microscopy: Application to the graphite (0001) and au(111) surfaces," *J. Chem. Phys*, vol. 98, pp. 7565–7573, 1993.

[74] G. P. et al, "Wannier90 as a community code: new features and applications," *J. Phys. Cond. Matt*, vol. 32, no. 165902, 2020.

[75] H. Raza, *Graphene Nanoelectronics.* Springer, 2012.

[76] J.-J. Zheng, X. Zhao, S. B. Zhang, and X. Gao, "Tight-binding description of graphyne and its two-dimensional derivatives," *J. Chem. Phys.*, vol. 138, no. 244708, 2013.

[77] S. Flannigan, L. Madail, R. G. Dias, and A. J. Daley, "Hubbard models and state preparation in an optical lieb lattice," *New Journal of Physics*, vol. 23, p. 083014, 2021.

[78] L.-K. Lim, J.-N. Fuchs, F. Piéchon, and G. Montambaux, "Dirac points emerging from flat bands in lieb-kagome lattices," *Phys. Rev. B*, vol. 101, p. 045131, Jan 2020.

[79] C. Zhong, Y. Xie, Y. Chen, and S. Zhang, "Coexistence of flat bands and dirac bands in a carbon-kagome-lattice family," *Carbon*, vol. 99, pp. 65–75, 2016.

[80] G. G. Naumis, "Electronic properties of 2d materials and its heterostructures: a minimal review," *Rev. mex. fis.*, vol. 67, no. 5, 2021.

[81] D. C. M. Rodrigues, L. L. Lage, P. Venezuela, and A. Latgé, "Exploring the enhancement of the thermoelectric properties of bilayer graphyne nanoribbons," *Phys. Chem. Chem. Phys.*, vol. 24, pp. 9324–9332, 2022.

[82] O. Leenaerts, B. Partoens, and F. M. Peeters, "Tunable double dirac cone spectrum in bilayer -graphyne.," *Appl. Phys. Lett.*, vol. 103, p. 013105, 2013.

[83] T. Ouyang, H. Xiao, Y. Xie, X. Wei, Y. Chen, and J. Zhong, "Thermoelectric properties of gamma-graphyne nanoribbons and nanojunctions," *Journal of Applied Physics*, vol. 114, no. 7, p. 073710, 2013.

[84] T. Ouyang, Y. Chen, L.-M. Liu, Y. Xie, X. Wei, and J. Zhong, "Thermal transport in graphyne nanoribbons," *Physical Review B*, vol. 85, no. 23, p. 235436, 2012.

[85] H. Sevinçli and C. Sevik, "Electronic, phononic, and thermoelectric properties of graphyne sheets," *Appl. Phys. Lett.*, vol. 85, p. 223108, 2014.

[86] M. P. Lima, A. J. R. da Silva, and A. Fazzio, "Splitting of the zero-energy edge states in bilayer graphene," *Phys. Rev. B*, vol. 81, p. 045430, Jan 2010.

[87] J. M. B. Lopes dos Santos, N. M. R. Peres, and A. H. Castro Neto, "Continuum model of the twisted graphene bilayer," *Phys. Rev. B*, vol. 86, p. 155449, Oct 2012.

[88] E. Suárez Morell, J. D. Correa, P. Vargas, M. Pacheco, and Z. Barticevic, "Flat bands in slightly twisted bilayer graphene: Tight-binding calculations," *Phys. Rev. B*, vol. 82, p. 121407, Sep 2010.

[89] P. Moon and M. Koshino, "Optical absorption in twisted bilayer graphene," *Phys. Rev. B*, vol. 87, p. 205404, May 2013.

[90] Z. F. AWang, F. Liu, and M. Y. Chou, "Fractal landau-level spectra in twisted bilayer graphene," *Nano Letters*, vol. 12, pp. 1530–6984.

[91] X.-Y. Xu, X.-W. Wang, D.-Y. C. andC. Morais Smith, and X.-M. Jin, "Quantum transport in fractal networks," *Nature Photonics*, vol. 15, pp. 703–710, 2021.

[92] N. A. Lemos, *Mecânica Analítica*. Livraria da Física University Press, 2007.

[93] L. D. Landau and E. M. Lifshitz, *Quantum mechanics: non-relativistic theory*. Elsevier, 1958.

[94] X. Chenl, *The Hofstadter spectrum of monolayer and bilayer graphene van der Waals heterostructures with boron nitride (PhD)*. Lancaster University, 2015.

[95] D. R. Hofstadter, "Approximate analog computing with metatronic circuits," *Physical Review B*, vol. 14, no. 6, 1976.

[96] P.G.Harper, "Single band motion of conduction electrons in a uniform magnetic field," *Phys. Soc. A*, vol. 68, 1955.

[97] Y. Aharonov and D. Bohm, "Significance of electromagnetic potentials in the quantum theory," *Phys. Rev.*, vol. 115, no. 485, 1959.

[98] L. A. Ponomarenko, R. V. Gorbachev, G. L. Yu, D. C. Elias, R. Jalil, A. A. Patel, A. Mishchenko, A. S. Mayorov, C. R. Woods, J. R. Wallbank, B. A. P. M. Mucha-Kruczynski, M. Potemski, I. V. Grigorieva, K. S. Novoselov, F. Guinea, V. I. Falko, and A. K. Geim, "Cloning of dirac fermions in graphene superlattices," *Nature*, vol. 497, p. 594–597, 2013.

[99] N. Moreau, *Development of a tight-binding model to study Hofstadter's butterfly in graphene on h-BN exhibiting a moiré pattern*. Université catholique de Louvain, 2017.

[100] J. Herzog-Arbeitman and et al., "Hofstadter topology: Noncrystalline topological materials at high flux," *Phys. Rev. Lett.*, vol. 125, no. 236804, 2020.

[101] J. Wang and L. H. Santos, "Classification of topological phase transitions and van hove singularity steering mechanism in graphene superlattices„" *Phys. Rev. Lett.*, vol. 125, 2020.

[102] H. Aoki, M. Ando, and H. Matsumura, "Hofstadter butterflies for flat bands," *Phys.Rev.B*, vol. 54, no. 24, 1996.

[103] Y. Matsuki, K. Ikeda, and M. Koshino, "Fractal defect states in the hofstadter butterfly," *Phys. Rev. B*, vol. 104, p. 035305, Jul 2021.

[104] X. R. Wang, "Localization in fractal spaces: Exact results on the sierpinski gasket," *Phys. Rev. B*, vol. 51, pp. 9310–9313, Apr 1995.

[105] J.J.Sakurai and J. Napolitano, *Modern Quantum Mechanics.* Cambridge University Press, 2017.

[106] G. Bhimanapati, N. Glavin, and J. Robinson, *Chapter Three - 2D Boron Nitride: Synthesis and Applications.* Elsevier, 2016.

[107] C. H. Lewenkopf and E. R. Mucciolo, "The recursive green's function method for graphene," *Journal of Computational Electronics volume*, vol. 12, p. pages203–231, 2013.